Predicting the Effects of Dent Size on the Stress in Aluminum Honeycomb Aircraft Panels Subject to Low-Velocity Impact Damage

Prédiction des effets de la taille d'indentation sur les contraintes dans les panneaux d'aéronef en aluminum en nid d'abeille soumis à des dommages d'impact à faible vitesse

A Thesis Submitted to the Division of Graduate Studies of the
Royal Military College of Canada
by

Joel Daniel Benotto, BEng, rmc

In Partial Fulfillment of the Requirement for the Degree of
Master of Applied Science in Mechanical Engineering

January 2018

To my darling wife, Tori: you are my pride and joy; your enduring love and countless sacrifices have made this work possible. To my two beautiful daughters, Beth and Bella: you teach me so much; your laughter and song bring me happiness.

Acknowledgements

I would like to thank Dr. Diane Wowk for her guidance, patience, and support at every stage of my thesis. A special thanks to Capt. David Hardy and Capt. Andrea Fortier for livening up the work environment and supporting me during hard times, and to Dr. Catharine Marsden, Ms. Luba Goyaniuk, Mrs. Crystal Itwar-Barrett, Mr. Baptiste Vaesken, Lt(N) Gregory (Skippy) Clarke, Mr. Tyler Reyno, Mr. Tanner Rellinger, Mr. Dennis Bellamy, Mr. Satpreet Singh Sidhu, Mr. Bryan Little, Mr. Alex Pym, Ms. Natalie Chénier, and Mr. Mich Lavoie for enabling my work in other capacities.

Abstract

Aluminum honeycomb sandwich structures are commonplace in aerospace applications due to their high in-plane strength and bending stiffness-to-weight ratio. A disadvantage of these structures is that they are susceptible to indentation from tool drops, hail, and runway debris occurring during maintenance, taxiing, or takeoff due to their poor out-of-plane resistance to deformation. Current literature states that impact damage can result in significant losses in residual strength, but studies featuring dented metal panels subjected to fatigue loading, tension, and bending are lacking. Furthermore, there are no comprehensive studies that identify the primary damage characteristics affecting the residual strength of metallic sandwich panels. The current work presents a method for predicting post-impact face sheet stresses for a panel loaded in tension using finite element (FE) modelling. Specifically, a two-stage loading simulation consisting of a dynamic impact event followed by an applied tensile load was used for determining the effects of dent diameter and depth on the increases in stress in the dented region of the impacted face sheet. It was determined that it was the degree of core damage associated with the dent and not the dent geometry specifically that had an effect on the face sheet stresses in tension. Material failure in the damaged core caused the tensile load to pass through the dented face sheet rather than the core, resulting in a larger percent increase in stress versus a panel with less core damage.

Résumé

Les structures sandwich en aluminum en nid d'abeille sont utilisées dans les applications aérospatiales en raison de leur résistance élevée dans le plan des feuilles et de leur rigidité à la flexion. Cependant, ces structures sont susceptibles à l'indentation causé par des gouttelettes d'outil, de la grêle et des débris de piste se produisant pendant l'entretien, le roulage ou le décollage en raison de leur faible résistance à la déformation hors du plan des feuilles. La littérature actuelle indique que les dommages causés par les chocs peuvent entraîner des pertes importantes de résistance résiduelle, mais les études portant sur des panneaux métalliques avec l'indentation soumis au chargement de fatigue, à la tension et à la flexion font défaut. De plus, aucune étude complète n'identifie les caractéristiques principales d'endommagement affectant la résistance résiduelle des panneaux sandwich métalliques. Le travail actuel présente une méthode pour prédire les contraintes de la feuille en aluminum après impact pour un panneau chargé en tension en utilisant la modélisation par éléments finis. Précisément, une simulation de chargement en deux étapes consistant en un événement d'impact dynamique suivi d'une charge de tension a été utilisée pour déterminer les effets du diamètre et de la profondeur de l'indentation sur les augmentations de contrainte dans la région bosselée de la feuille impactée. Il a été déterminé que c'était le degré d'endommagement du noyau associé a l'indentation et non la géométrie de l'indentation qui avait un effet sur les contraintes dans la feuille après la charge de tension. La défaillance du matériau dans le noyau endommagé a provoqué le passage de la charge de tension à travers la feuille bosselée plutôt que le noyau, ce qui a entraîné une augmentation de contrainte plus élevée comparé à un panneau moins endommagé.

Contents

List of Tables

List of Figures

List of Acronyms

BVID	Barely Visible Impact Damage
CAI	Compression-After-Impact
DND	Department of National Defence
FE	Finite Element
OEM	Original Equipment Manufacturer
RCAF	Royal Canadian Air Force
SRM	Standard Repair Manual
UK	United Kingdom

1. Introduction

Honeycomb sandwich structures typically consist of a low-density metallic core bonded between two metallic or laminate face sheets. This yields excellent in-plane strength and stiffness-to-weight ratios and makes them ideal in aerospace applications where they are used for floor panels, bulkheads, and aerodynamic and control surfaces. They are commonly found in commercial and military helicopters such as the Royal Canadian Air Force's (RCAF) CH-146 Griffon helicopter, illustrated in Figure 1.1.

Figure 1.1: CH-146 Griffon helicopter, 408 Tactical Helicopter Squadron, Airfield 21, Wainwright, Alberta, Exercise MAPLE RESOLVE 16, May 29, 2016 [1].

One disadvantage of honeycomb sandwich structures is that they exhibit poor out-of-plane impact resistance due to the thin face sheets. In the case of Barely Visible Impact Damage (BVID) which results from blunt objects such as tools, hail, and runway debris during taxiing, maintenance, or take-off, damage to the core may be extensive despite seemingly minimal

surface damage. Figure 1.2 and Figure 1.3 show flat and curved panels from a retired Griffon helicopter with multiple BVID-class dents viewed from the surface. Figure 1.4 shows a view of the core for a flat panel with impact damage after panel sectioning.

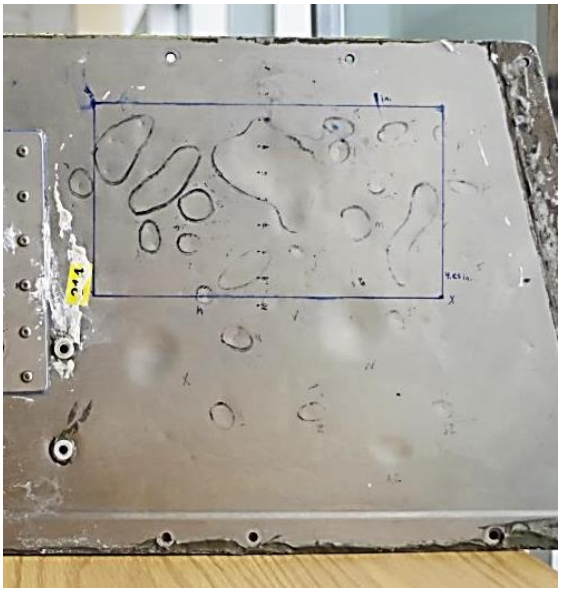

Figure 1.2: Exterior view of a flat panel from a retired Griffon helicopter [2].

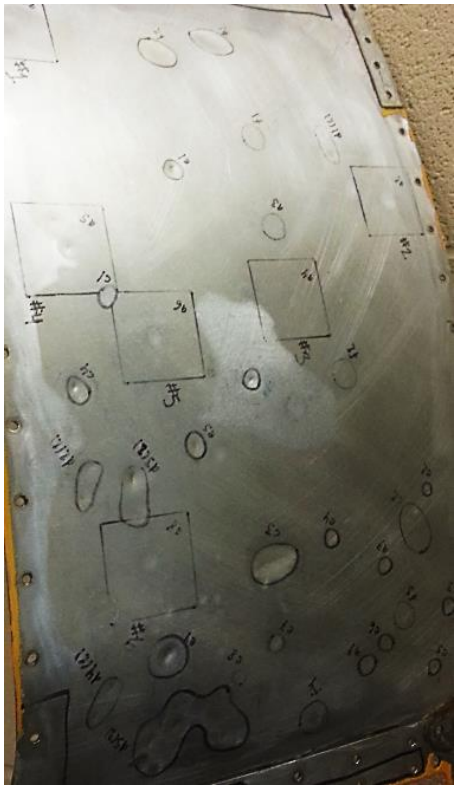

Figure 1.3: Exterior view of a curved panel from a retired Griffon helicopter [2].

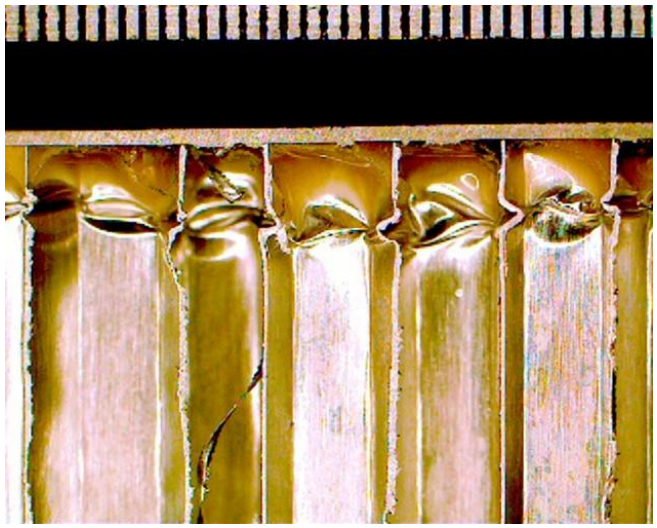

Figure 1.4: Side view of a sectioned panel with impact damage [2].

The damage limits outlined in Standard Repair Manuals (SRM) provided by the Original Equipment Manufacturer (OEM) are based on surface damage dimensions such as dent depth, diameter, and area. These limits have not been optimized in that they do not describe or quantify the loss in the residual strength of the panel in question. As such, it is suspected that they may be conservative. Therefore, it is of interest to study the factors affecting the residual strength in order to potentially extend the damage limits and prolong the service life of the panels considered.

Numerical modelling techniques using FE modelling software have the potential to address these challenges thanks to its ability to easily display and predict stresses from different panel and dent configurations in a cost-effective manner compared to equivalent experiments conducted in a laboratory setting.

1.1. Motivation

This thesis comprises work on a larger project that seeks to extend the service life of honeycomb panels from the Griffon helicopter by re-evaluating the damage limits. Specifically, a simplified numerical model of the panel in question with a homogeneous core (as opposed to 3D cell geometry) and representative core damage would be employed for rapidly quantifying the loss in residual strength for varying dent configurations. Residual strength hereby refers to the residual capacity of a dented panel to support in-service loads, and accounts for stress-based failure modes such as fatigue and bending instability such as localized buckling in the core. The approach of the project is to develop a methodology using FE modeling where simplified models can be used to predict residual stress. This would require knowing what characteristics of the damage affect residual strength so they can be incorporated into the simplified models.

1.2. Goals

The primary goal of this thesis is to identify the influence of face sheet dent depth and dent diameter resulting from low-velocity impact on face sheet stresses from post-impact tensile loading. Increased stresses could highlight problem areas in fatigue, and any characteristics of the damage that contribute to a reduction in residual strength should be included in future simplified models used for predicting the effects of dents on the residual strength of honeycomb panels.

1.3. Methodology

The influence of the dent depth and diameter on the face sheet stresses when loaded in tension was predicted using a FE model of a honeycomb panel with the 3D cell geometry represented. The numerical model described herein was divided into two loading stages: the first stage consisting of the impact event that creates the damage, and the second stage consisting of the tensile loading post-impact.

In the first stage, a model was developed to simulate the damage caused by a dynamic impact from a spherical object. The state of damage here was compared qualitatively to experimental work in terms of the overall damage and dent size including the dent depth and dent diameter.

In the second stage, the model used for the first stage was adapted to account for quasi-static, post-impact tensile loading through the addition of another load step. This resulted in a two-stage sequential loading simulation. The effects of face sheet dent depth and diameter on the stresses in the panel face sheets under tensile loading was then determined.

1.4. Chapter overview

Chapter 2 outlines important concepts in regards to honeycomb sandwich structures, damage limits, and low-velocity impact, and summarizes the findings published in literature on using numerical modelling techniques for modelling impact damage and post-impact loading. **Chapter 3** presents the model development and results from the impact damage stage. **Chapter 4** presents the methods for modelling post-impact tensile loading and the resulting face sheet stresses. **Chapter 5** presents the results of a study on the effect of dent size on face sheet stresses for post-impact tensile loading. **Chapter 6** summarizes the key findings and discusses areas for further research.

2. Literature Review

This chapter outlines important concepts in regards to honeycomb sandwich structures, damage limits, and low-velocity impact, and summarizes the findings published in literature on using numerical modelling techniques for modelling impact damage and post-impact loading.

2.1. Honeycomb sandwich structures

The honeycomb sandwich structure addressed herein consists of an aluminum honeycomb core sandwiched between two aluminum face sheets, bonded using an epoxy adhesive, as shown in Figure 2.1, where *L1* and *L2* are the dimensions of a panel coupon, *h* is the height of the core, t_f is the thickness of the face sheets, and t_a is the effective thickness of the adhesive.

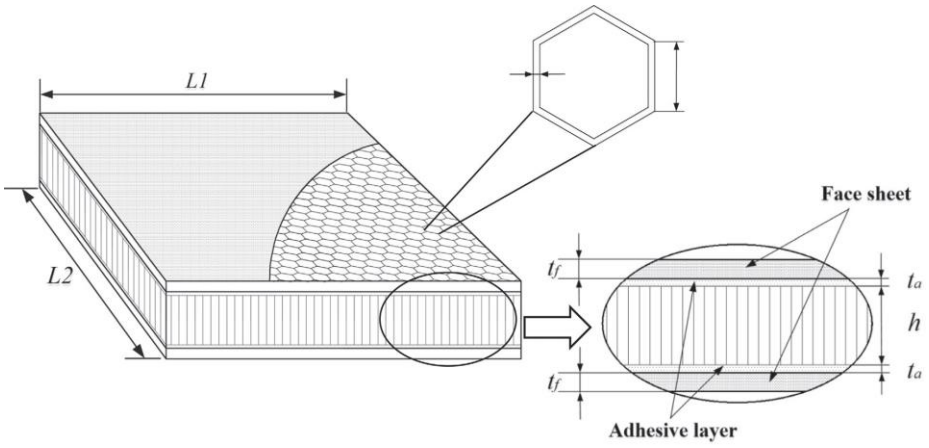

Figure 2.1: Illustration of a typical honeycomb sandwich panel setup [3].

The face sheets provide high in-plane tensile strength and stiffness but lack bending stiffness on their own. Combined with the core which increases the distance measured between the two face sheets, thus, the second

moment of area, the resulting structure has a dramatically improved stiffness-to-weight ratio and bending strength over face sheets on their own. Neither the face sheets of the core have much resistance to local out-of-plane deformation which makes the panels susceptible to localized buckling in the core upon impact. In some cases, the damage to the core could be concealed by the presence of the face sheet. This is revealed upon inspection of panels that have been indented and sectioned, as shown in Figure 2.2.

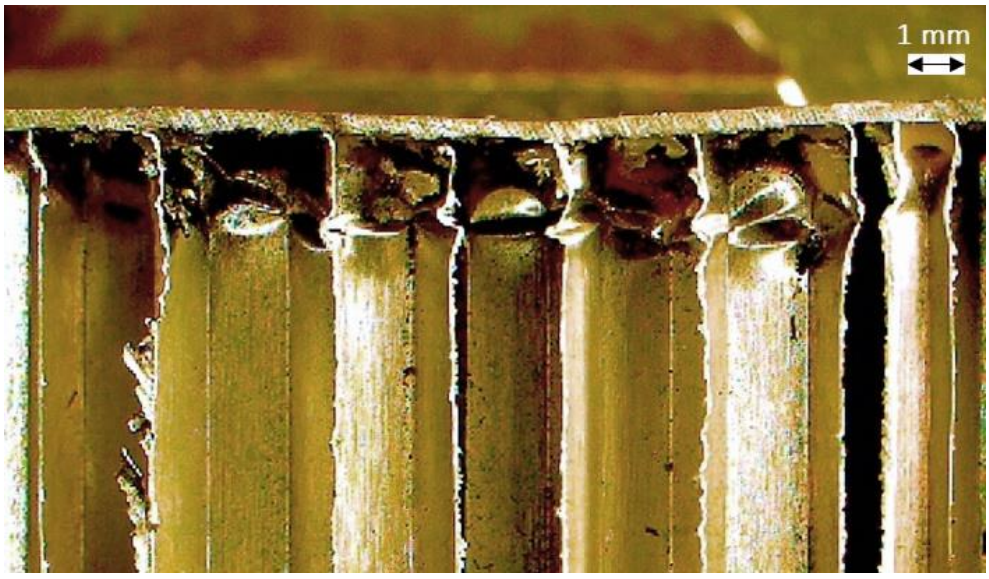

Figure 2.2: Illustration of BVID with localized buckling in the core and a relatively flat top face sheet [2].

The damage shown in Figure 2.2 is typical of a low-velocity impact where the result is a surface dent with localized core crushing.

2.2. Damage limits

The SRM for the Griffon helicopter panels of interest lists three categories of damage: negligible damage, allowable damage, and that which is more severe than allowable damage [4]. Negligible damage does not require

recording, whereas allowable damage does. Both the negligible and allowable damage limits are given in terms of the dimensions of the damage to the panel surface, particularly, dent diameter. Specifically, negligible damage is defined as any dent less than 12.7mm (0.5in) in diameter with no restrictions on depth provided there are no punctures or cracks. Allowable damage is restricted to a 101.6mm (4.0in) maximum diameter of any one dent and a maximum depth per dent of 20% of the panel thickness (or, 2.54mm (0.1in) for a 12.7mm (0.5in) panel thickness). Any damage exceeding these limits requires repair or replacement of the panel. This thesis considers low-velocity impact because it produces dents within the allowable damage limits void of punctures or cracks which would otherwise lead to repair or replacement of the panel.

2.3. Low-velocity impact

The concept of low-velocity impact can be understood as follows, with illustrations provided in Figure 2.3. Upon contact with the indenter, the face sheet deflects inwards while the cells of the core begin to yield and buckle locally (Figure 2.3a). At maximum impact depth, localized buckling of the cell walls in the core worsens, resulting in crumpling of the cells in this location (Figure 2.3b). The residual elasticity of the structure, primarily in the face sheets and attributed to a comparatively larger stiffness and yield strength, results in a phenomenon dubbed “spring-back”. This is where the impressed face sheet rebounds following impact, leaving a surface dent that is shallower than that formed at maximum impact depth (Figure 2.3c).

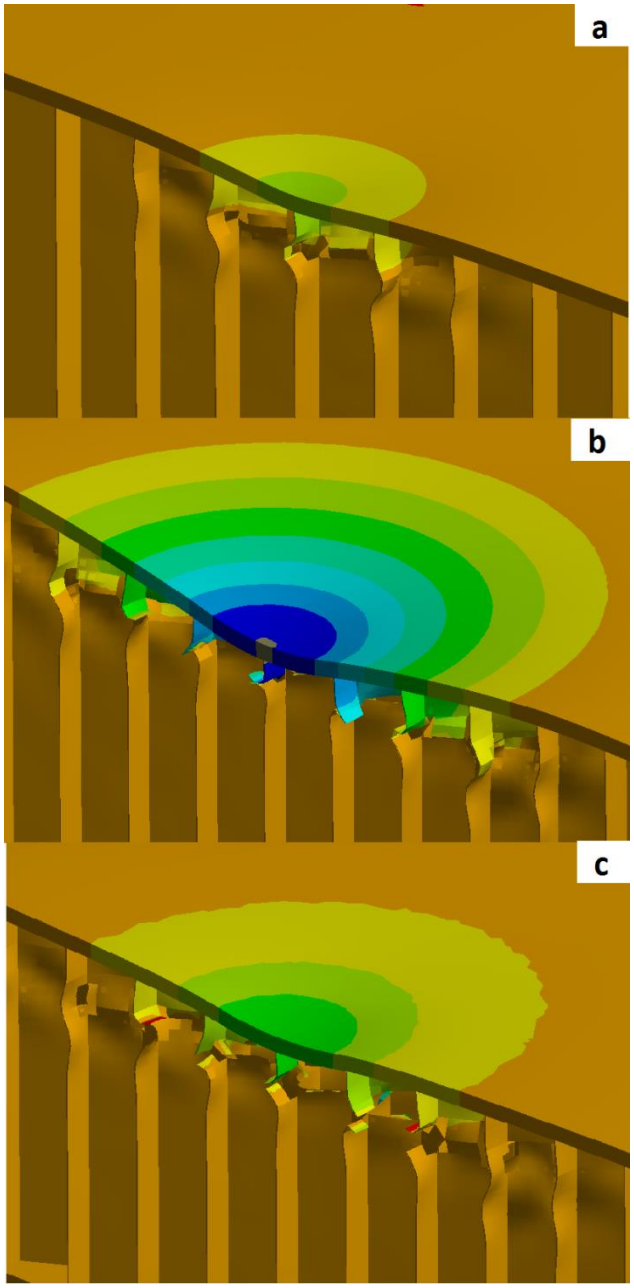

Figure 2.3: Stages of indentation and progression of core damage in terms of vertical displacement; (a) initial impact and initiation of localized buckling; (b) maximum impact depth; and (c) spring-back. The colour blue indicates a greater vertical displacement value.

Low-velocity impact damage can reduce the strength in tension, compression, bending, and fatigue by as much as 50% depending on the damage mode [5]. This may further result in reduced airfoil stiffness, leading to unfavourable aeroelastic phenomena and a significantly reduced fatigue life [6].

Though spring-back is not as severe for metallic face sheets as it is for laminates, BVID can result nonetheless. BVID is simply a class of low-velocity impact damage that is characterized by dents that are difficult to detect from visual observation alone. The criterion for classifying BVID is loosely based on dent depth as opposed to dent diameter for the damage limits outlined previously and is largely contested in terms of the range of accepted measurements. As an example, the National Physical Laboratory in the United Kingdom (UK) defined BVID as damage causing a dent depth of 0.5mm [7], whereas a NASA report defined BVID as having a dent depth within the range of 1.27mm to 2.54mm [8].

Given the lack of an official definition for BVID in terms of accepted measurements, the numerical models in the current work, sought to replicate the dents observed from a retired Griffon panel. Specifically, dent depths in the range of 0.14-1.01mm and dent diameters in the range of 2.96-96.46mm were measured [2]. These respect the allowable damage limits and consist of both visible surface damage and BVID.

2.4. Modelling impact damage

There are a number of different methods for replicating low-velocity impact damage to aluminum honeycomb panels. The focus of these methods is on quantifying the damage to the face sheet, and fewer focus on damage to the core. Experimental methods typically consist of a drop-test machine wherein a blunt object is dropped onto the test specimen and a high-speed camera captures the pre- and post-impact indenter velocities used for determining the energy absorbed by the structure, and in some cases a form of topography measurement method for measuring the profile of the residual dent [3] [9-23]. Analytical methods based on spring-mass

and energy balance models are often used in tandem with experimental methods for rapidly estimating specific properties such as energy absorption and indentation response [3] [11-13] [19-20] [24-25]. In either case, the results are limited to those measured superficially; in other words, the global response and surface damage is prioritized over the local response and core damage. As such, researchers often compliment their experiments with equivalent numerical models, the majority of which use FE software to replicate low-velocity impact damage with attention paid to core damage [10-14] [21] [23]. Others use numerical models exclusively for conducting parametric studies [26] [27]. In any case, these models typically consist of a simulation of the drop-test wherein an object impacts a model of a panel coupon and specific results such as equivalent (von Mises) stress and equivalent plastic strain are predicted.

The primary benefit of modelling impact damage numerically consists of the ability to investigate stresses and strains on a component-by-component basis, among others such as the comparatively reduced cost and ability to work collaboratively on the same model, to name a few. In order to develop such a model, a number of features are important to consider. These comprise the analysis type, core and adhesive representation, the parameters affecting damage, and other model details such as coupon shape, element type, element size, material failure representation, the strain-hardening behaviour of the honeycomb core, and criteria for assessing damage

2.4.1. Analysis type

Low-velocity impact damage can be modelled in two different ways, namely through dynamic impact or quasi-static indentation. As an example, McQuigg et al. [28] studied low-velocity impact damage using both a drop-test set-up and quasi-static indentation and found that both methods produced roughly the same damage except at lower energy levels where it was found that quasi-static indentation produced greater damage. Similarly, Schubel et al. [29] studied both methods of generating low-

velocity impact damage using panels with laminate face sheets and PVC foam cores. It was found that damage initiated sooner and was more severe for quasi-static indentation, especially in the indenter-face sheet contact region.

Furthermore, using FE modelling software, the user has the choice of either an implicit or explicit solver for modelling low-velocity impact damage. The two differ largely in the time integration scheme used. Implicit solvers are normally used for static structural problems where the loading lasts longer than a second, whereas explicit solvers are normally used for dynamic problems where the loading lasts less than a second. Implicit solvers approximate the solution at discrete time steps using equilibrium iterations, whereas explicit solvers do so explicitly without having to iterate during time integration. Implicit solvers are normally better-suited for linear problems, whereas explicit solvers are normally better-suited for highly non-linear problems. For these reasons, an explicit solver is normally used for modelling impact damage, and an implicit solver is normally used for modelling post-impact loading. The latter is further discussed in Section 2.5.

Virtually all researchers modelling low-velocity impact damage to honeycomb sandwich structures have used explicit dynamic analyses over quasi-static analyses [3] [9-18] [21-23]. The results of these simulations show good agreement with their respective experimental results. Foo et al. [12] used an explicit FE model of an aluminum honeycomb sandwich panel to study the factors affecting the initiation and propagation of low-velocity impact damage such as honeycomb core density and strain-hardening models. Similarly, Zhang et al. [9] used an explicit FE model of an aluminum honeycomb sandwich panel to study energy absorption of the face sheets and core and the effect of the adhesive that bonds the core to the face sheets.

2.4.2. Core representation

Generally, there are three ways of representing a honeycomb core when modelling impact damage numerically. The first consists of homogenizing the core as a single block of material with equivalent orthotropic mechanical properties determined from experimental testing. The second consists of using a grid of equivalent non-linear springs. The third consists of full core details such as cell geometry, core plasticity, and core buckling. The first and second are normally used to study the impact response of honeycomb structures and benefits from quick solve times, whereas the third accurately models both the impact response and damage modes incurred from low-velocity impact, but at significantly longer solve times.

Horrigan and Aitken used a continuum damage model for simulating non-metallic core crushing due to impact [14]. It was found that it underestimated core damage width by a factor of 3 and overestimated the permanent deformation by a factor of 2. Meo et al. modelled low-velocity impact damage to a panel with laminate skins and a homogenized Nomex® core calibrated using experimental data for the purpose of studying surface damage and the energy absorption properties [18]. It was found that the experimental and numerical results agreed well for the dent depth and the area of delamination. Similarly, Atkay et al. studied the crushing behaviour of both aluminum and Nomex® honeycomb panel specimens with laminate face sheets, along with homogenized core variants. It was found that the models with homogenized cores were insufficient for capturing extensive fracture, especially when failure resulted from the core [30]. Lastly, Castanié et al. studied the validity of using a grid of non-linear springs for modelling the low-velocity impact response of metal-skinned panel with a Nomex® core [31]. It was found that the springs could not model transverse shear in the core under bending.

All other studies considered herein utilized models of honeycomb cores with the 3D geometry of the cells. In doing so, this enabled the study of damage and failure modes, localized buckling in the core, face sheet spring-back, and changes to the load path for post-impact loading, to name a few. Lee et al. [21] utilized the 3D honeycomb cell structure to study

dynamic fracturing mechanisms through indenter contact point position for a low-velocity aluminum honeycomb panel specimen. It was found that peak impact force was greatest when the indenter was centred at the cell centre, and that cracks propagated to the core from those that had initiated in the face sheet. Zhu and Chai [16] modelled a honeycomb panel with laminate face sheets and a geometrically correct Nomex® core to develop low-velocity impact damage and failure mode maps for varying parameters such as core density, indenter radius, and face sheet thickness.

2.4.3. Adhesive representation

Adhesives affect the structural response of honeycomb sandwich panels subjected to low-velocity impact in a number of different ways. Namely, the adhesive increases the stiffness of the face sheets [17], increases the energy-absorbing capacity of the panel [3] [9] [32], and offsets localized buckling in the core [2]. However, many studies featuring numerical models have largely neglected the adhesive altogether, either to minimize model run times or citing the influence as negligible. Only a handful of researchers have studied the effects of the adhesive.

Zhu and Chai compared the low-velocity impact responses of panel specimens with acrylic face sheets detached from a Nomex® core and attached via Araldite® 2012 adhesive through experimental and numerical testing [17]. The bond between the face sheets and core in the numerical models were represented by node superposition. It was found that the structural stiffness and peak impact load for the attached specimens were roughly 3 and 1.5 times greater than the detached specimens, respectively.

In a preliminary study, Zhang et al. conducted experimental and numerical testing of an all-aluminum honeycomb sandwich panel subjected to low-velocity impact and studied the energy absorption properties, and indentation and load responses for models with and without a representative adhesive layer [9]. The adhesive was modelled by simply doubling the thickness of the impacted face sheet and maintaining node superposition. It was found that the presence of the adhesive lowered the

peak impact force, and prolonged contact duration and the elastic region, resulting in up to 4.6% more energy absorbed.

Lastly, inspection of sections of the retired Griffon panels has revealed a phenomenon wherein localized core buckling appears to be offset by the depth to which the adhesive extends down into the core. Under fatigue loading, cracks may initiate and grow in this region of cell crumpling. This is shown in Figure 2.4. The dashed red line indicates the depth of the adhesive.

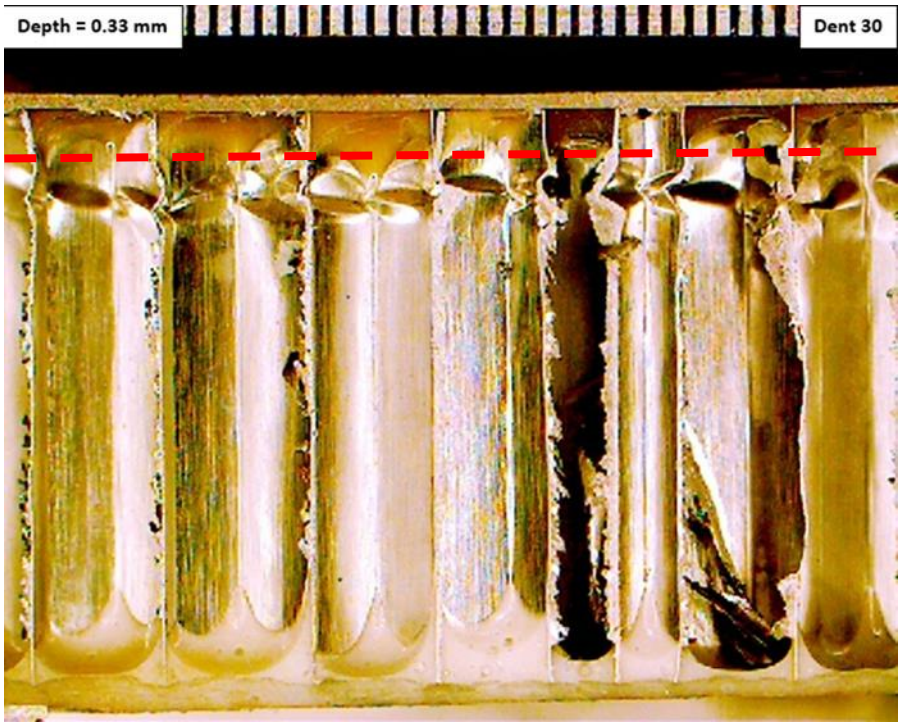

Figure 2.4: Illustration of a panel section showing localized core buckling offset by the epoxy adhesive for a dent depth of 0.33mm [2].

2.4.4. Parameters affecting damage

The primary parameters affecting low-velocity impact damage consist of those for the panel such as face sheet thickness and core density through

cell size and foil thickness, and those for the indenter such as indenter size as well as impact energy through indenter mass and velocity. Researchers have studied these parameters to varying degrees.

Concerning the panel parameters, Foo et al. [10] and Atkay et al. [30] conducted experimental and numerical testing on all-aluminum honeycomb structures and showed that the energy absorbed during impact is independent of the core density, though denser cores resulting from increased foil thickness and smaller cell sizes were shown to exhibit greater peak loads, increased buckling stability, and reduced damage profiles in the core and indented face sheet. Wowk and Marsden used numerical models to study the effect of face sheet thickness and core density on the residual dent depth, surface damage width, and face sheet stresses for a low-velocity impacted all-aluminum honeycomb sandwich structure [27]. For increasing face sheet thickness and decreasing core density, it was found that susceptibility to BVID increased due to the increased spring-back capacity. Furthermore, it was found that surface damage width increased linearly with face sheet thickness, and that the highest face sheet stresses were found around the circumference of the dent for thinner face sheets and towards the centre of the dent for thicker face sheets. Clarke [26] used numerical modelling to study the relationships between impact parameters, surface damage, and core damage for aluminum honeycomb sandwich panels. It was found that damage depth stayed constant for a given panel configuration and material selection, regardless of the input parameters. It was also found that decreasing face sheet thickness produced deeper dents with the same dent diameter and core damage size.

As for the impact parameters specifically, indenter shape is exclusively spherical or hemi-spherical in all of the literature considered. Tomblin et al. [33] and Raju et al. [34] studied the effect of the diameter of a hemispherical steel impactor on the low-velocity impact damage state of a panel with laminate skins. It was found that a smaller diameter impactor produced visible dents and fractures in the face sheet, and that a larger diameter impactor produced less visible dents and larger core damage states. Foo et al. [12] studied the effect of impact energy on the maximum indenter/face sheet deflection of a metallic panel for impact energies of 0.85J to 13.0J. It was found that maximum deflection increased linearly with increasing

impact energy. Similarly, Clarke [26] studied the residual dent depth and diameter for varying impact energies from 0.61J to 4.31J through indenter mass and velocity. It was found that residual dent depth and diameter increased linearly and logarithmically with increasing impact energy, respectively.

Based on these findings, different impact and panel parameters can result in different combinations of damage. In any case, the most severe damage to the core and face sheet is observed for the thinnest face sheets, the least dense cores, and the largest impact energies. Furthermore, large indenter shapes produce wide but shallow dents.

2.4.5. Additional model details

When modelling impact damage, a number of other features must be considered. These include the coupon shape, element type, element size, material failure representation, the strain-hardening behaviour of the honeycomb core, and criteria for assessing damage.

Coupon shapes typically consist of a square or circle. The former appears to be simpler for modelling and replicating results in a laboratory setting, whereas the latter can reduce run times by eliminating regions of insignificant structural contribution under low-velocity impact. Foo et al. appears to have studied circular coupons exclusively, having showed that runtime could be reduced by up to 25% due to a lower element count [10-13].

Elements in numerical FE models are critical for replicating the mechanical response of the structure for which they are based. Shell elements are normally used for fully-featured honeycomb cores and laminate and thin metallic face sheets in macro-models, whereas solid elements are normally used for homogenized cores and thick metallic face sheets in macro-models, and for honeycomb core cells in micro-models. Shell elements are employed for reducing run times in models utilizing explicit solvers where it is dictated by the smallest element edge length. As for element size, the

primary interest is in the region of damage, and is largely defined in terms of the number of elements measured along the cell edges (or "elements per cell wall"). Both Zhang et al. [3] [9] and Foo et al. [10] [12] used meshes of purely shell elements consisting of roughly 7-10 elements per cell wall for modelling low-velocity impact damage in their aluminum honeycomb panel specimens. It was found that their results in terms of both impact response and indentation characteristics closely resembled their equivalent experiments. Similarly, Ivañez and Sanchez-Saez [22] studied the low-velocity impact response of composite sandwich beams with laminate face sheets and an aluminum core using a mesh of shell elements and 4-5 elements per cell wall and also found the same accuracy in their results in comparison to their experiments. Conversely, Manes et al. [23] used brick elements to study damage initiation, shape, and failure using a highly detailed FE model of a honeycomb sandwich panel with aluminum face sheets and a Nomex® core.

Element failure through element erosion or a similar FE software feature is important for modelling core cracking, indenter penetration, or disbonding between the face sheet and core. The authors mentioned herewith chose different approaches for modelling element erosion based on different failure criteria. Zhang et al. [3] [9] neglected using a failure criterion since no obvious cracking or penetrative damage was observed from experiments. The models used by Foo et al. [10] [12] included detailed element erosion settings through the stress-based Hashin criteria. Likewise, Ivañez and Sanchez-Saez [22] used the Hou failure criteria. Lastly, Manes et al. [23] used a fracture locus curve.

The strain-hardening behaviour is important to consider because energy absorption is dominated by the core through local plastic deformation [35]. Foo et al. [12] and Zhang et al. [9] studied the strain-hardening behaviour of aluminum honeycomb cores for all-aluminum panels through numerical modelling. They showed that a bilinear hardening scheme is just as accurate as a Ramberg-Osgood hardening scheme concerning the low-velocity impact response and energy absorption.

Criteria for assessing damage are based on either surface damage through dent depth measurements, or core damage, normally in the form of

localized buckling and deformation. Zhang et al. [3] studied residual dent depth both experimentally and numerically for an aluminum honeycomb panel subjected to multiple low-velocity impact energies and found that it increased non-linearly with impact energy. Clarke [26] studied both surface and core damage using an explicit FE model and found that core damage width was virtually the same as dent diameter, and core damage depth was roughly constant for any variation of the impact parameters for a given panel configuration and panel material designation .

2.5. Modelling post-impact loading

There are different types of post-impact loading tests for measuring residual strength, ranging from compression-after-impact tests (CAI) [28] [36-42] to three- and four-point bending [43-45]. The former represents the bulk of the literature on this topic. CAI tests consist of a drop-weight setup for creating panel damage followed by a fixture setup which compresses the damaged panel in the ribbon direction up to the point of failure. CAI is typically used for panels with laminate face sheets since their compressive strength is susceptible to delaminations. For example, McQuigg et al. [28] [38] conducted multiple experimental CAI tests and equivalent numerical simulations of small honeycomb sandwich specimens with laminate face sheets and Nomex® cores and studied the effect of core material density on the CAI failure strength and failure mode for the same low-velocity impact damage. It was found that an increase in the core density resulted in a significant increase in failure strength and a different failure mode, namely, from indentation propagation to crack propagation. Similarly, Gilioli et al. [39] studied the statistical reduction in strength of small sandwich panel specimens with aluminum face sheets and Nomex® core due to low-velocity impact compared to undamaged cores. It was confirmed that CAI strength was reduced significantly for increasing impact energy, up to a 50J threshold. Conversely, Kang et al. [43] used static three-point bending experiments to study the influence of face sheet material and core thickness on the residual strength of low-velocity impact damaged honeycomb sandwich specimens with glass/epoxy and carbon/epoxy laminate face

sheets and a Nomex® core. It was found that residual strength increases were pronounced for core thickness increases in the glass/epoxy specimens, and that it was unaffected up to a given impact energy threshold. Past this threshold, residual strength rapidly reduced to 50% of the initial strength for all specimens considered. Unfortunately, the bulk of these tests consist of panels with laminate face sheets and Nomex® cores; studies featuring purely metallic panels are scarce.

These results are important to consider because, even though the surface damage was minimally visible, significant reductions in the load-carrying capacity occurred. For CAI, Tomblin et al. [46] explains that these reductions are a result of buckling and crumpling in the core which leaves the damaged face sheet unsupported and reduces its ability to carry loads, especially in bending. McQuigg et al. [28] mentioned this was due to the damaged face sheet since the undamaged face sheet had supported a portion of the load after failure. McGowan et al. [36] observed increased compressive strains in the region of damage. The remaining authors support these explanations indirectly through descriptions of the failure modes which are primarily stability-based or strain-based.

Concerning fatigue, Freeman et al. [44] studied the effect of penetrative low-velocity impact damage on the fatigue life of a small honeycomb sandwich specimen with two- and four-ply laminate face sheets and a low- and high-density foam-filled core using an experimental four-point bending setup. It was found that fatigue life for the panels with four-ply laminate face sheets and both foams and those with two-ply laminate face sheets and only the low-density foam was unaffected by the impact energies considered. This was largely due to the failure mode which was in shear at the contact points of the four-point bending setup. Conversely, fatigue life for the panels with two-ply laminate face sheets and the high-density foam was affected to the same degree for all impact energies considered. Specifically, failure was in bending in the region of pure bending where cracks emanating from the impact region were observed. This was shown through increased stress levels measured from the tests.

Studies on the effects of different parameters such as dent size on residual strength are limited to a few publications [28] [36-38] [40]. Furthermore,

none have studied the effects of these parameters for post-impact tensile loading. Aminanda et al. [37] studied the effect that the dent depth had on the residual compressive capability of a honeycomb sandwich panel specimen with brass face sheets and a Nomex® core with low-velocity impact damage from static indentation. It was found that the load-displacement behaviour in compression was not initially affected by dent depth, and that the residual strength decreased with increasing dent depth due to instability.

2.6. Areas for further research

Present publications on the residual strength of honeycomb structures with low-velocity impact damage are sparse in a few areas. Specifically, most authors have opted for laminate face sheets over metallic face sheets. In regards to the type of post-impact loading, none have featured tensile loading in relation to fatigue. This is important because CAI does not trigger the same failure mechanisms in panels with metallic face sheets compared to panels with laminate face sheets, and because in-service bending loads could result in tensile regions in the outer portion of the panel where the bulk of the impact damage is located. Lastly, there have been no comprehensive studies that have focused on identifying the damage characteristics that have the most significant effects on the residual panel strength. Given these shortfalls, the present paper aims to study the effect of face sheet dent depth and dent diameter on face sheet stresses resulting from post-impact tensile loading.

3. Modelling impact damage

3.1. Introduction

In order to predict the effect of dent size on face sheet stresses due to post-impact tensile loading, a two-stage dynamic model was developed. The first stage consisted of modelling the impact damage, followed by the second stage which consisted of the post-impact tensile loading. This chapter provides details on the model used for modelling the first stage.

The purpose of this model was to confirm its ability to capture important details used for modelling post-impact loading in Chapter 4 such as plasticity in the core and face sheet and localized core buckling. It also had to be able to generate different damage states meant for studying damage characteristics such as core damage depth and width later on in Chapter 5. ANSYS Academic Research structural analysis software was used throughout, namely, versions 15.0 and 17.2 of ANSYS Mechanical.

3.2. Model details

The approach with this section was to use a dynamic solver to model low-velocity impact damage by a hemispherical indenter to a roughly square aluminum honeycomb sandwich panel coupon with the 3D cell structure featured. The properties of the panel are representative of a flat panel from the CH-146 Griffon.

The model described herein was used to simulate the impact event and to create different damage stages for the two-stage simulations described in Chapter 4. These different damage states were created by altering face sheet thickness in one scenario and indenter radius and velocity in another scenario while keeping all other aspects of the model the same.

3.2.1. Geometry

The geometry of the panel coupon modelled in ANSYS consisted of a 12.192mm (0.48″) thick core sandwiched between two 0.508mm (0.020″) thick face sheets, yielding a total panel thickness of 12.7mm (0.50″). The core itself comprised hexagonal cells of size 3.175mm (0.125″) measured across flats with a foil thickness of 0.0254mm (0.001″) and a doubled thickness of 0.0508mm (0.002″) in the ribbon or L-direction. A representative adhesive layer was designated for the top 1.424mm of the core. The hemispherical indenter was initially modelled as a spherical shell with a radius of 12.7mm (0.5″) and a shell thickness of 0.5mm (0.0197″). It was subsequently sliced at a vertical distance of 0.51mm (0.2201″) from the top face sheet in order to limit the number of elements in the model. The center of the indenter corresponding to the initial point of contact with the face sheet upon impact was aligned with the mid-point of a doubled cell wall found at the center of the coupon. This indenter positioning was kept constant for all simulations. These dimensions are illustrated in Figure 3.1-Figure 3.3.

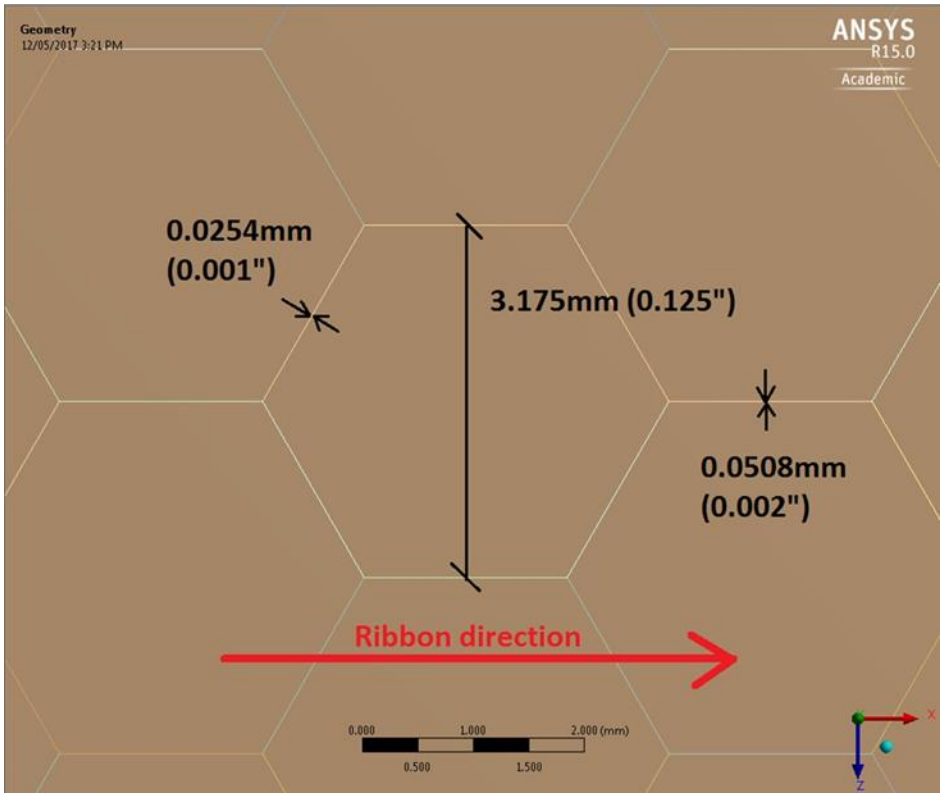

Figure 3.1: Model cell size and cell wall thickness.

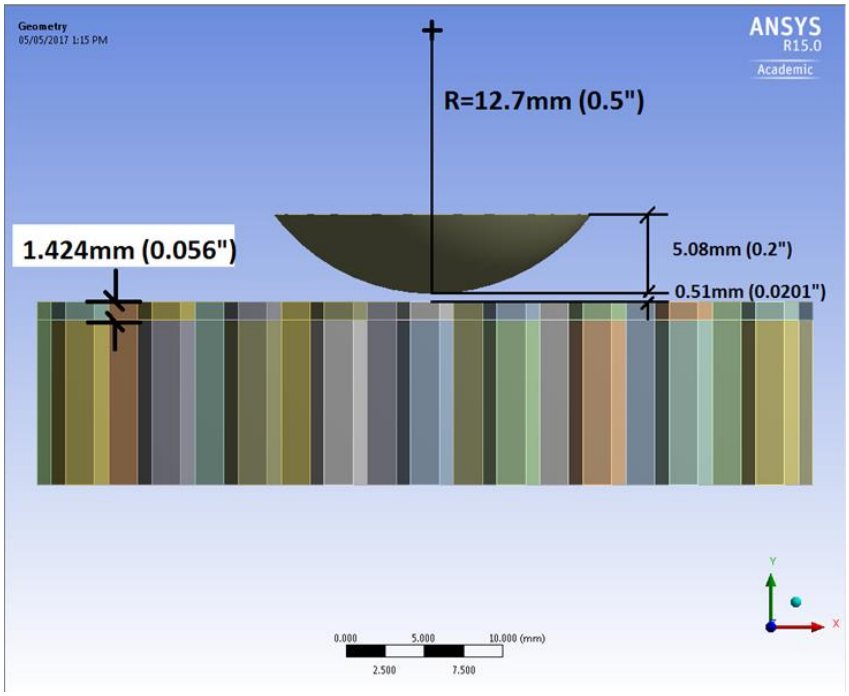

Figure 3.2: Model adhesive layer and indenter dimensions and placement.

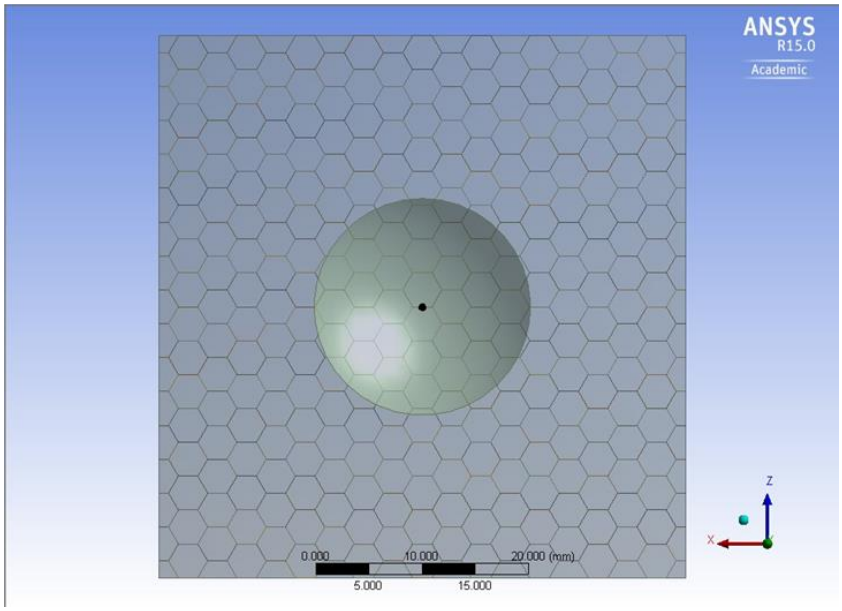

Figure 3.3: Model indenter positioning.

The dimensions of the coupon were chosen to represent an infinite panel void of the influence from boundary conditions, and were selected to be 93.5mm (3.68″) by 95.2mm (3.75″). Details of how the coupon size was selected are presented in Subsection 3.3.1. The coupon size corresponded to a total of 17 cells measured along the L-direction and 30 cells measured along the W-direction. These dimensions are illustrated in Figure 3.4.

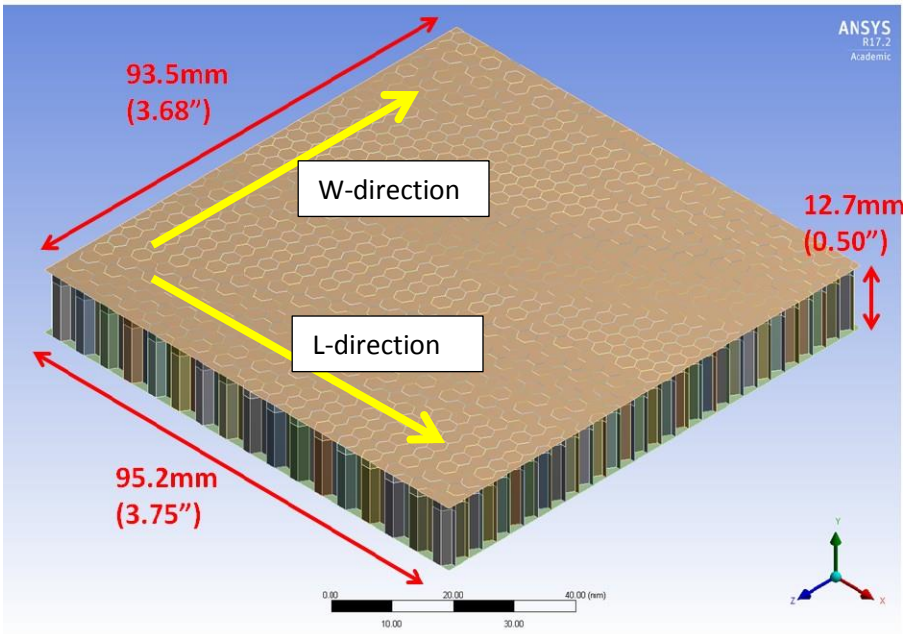

Figure 3.4: Model coupon dimensions.

3.2.2. Material properties

The face sheets were assumed to be made of 7075-T6 aluminum and the core of 5052-H32, which are typical of the materials used for honeycomb panels on the CH-146 Griffon. The indenter was assumed to be made of steel and the adhesive bonding the core to the face sheets of HYSOL EA 934NA. A maximum equivalent plastic strain failure criterion was used in tandem with element erosion for all components except for the indenter which was assumed to be linear elastic and was not expected to yield.

The top 1.424mm of the core geometry was given material properties to represent the presence of the adhesive. This included one set of material properties for the regular cell walls (denoted by "Adhesive, W-direction") and another for the doubled cell walls (denoted by "Adhesive, L-direction"). The process by which these material properties were determined is outlined in Subsection 3.3.2. The modulus of elasticity of 70300MPa cited for 5052-H32 represents an average of the tensile and compressive moduli, with the compressive modulus being 2% greater than the tensile modulus.

Bilinear strain-hardening models were used for both the face sheets and core over a curve because Zhang et al. [9] showed that it was an acceptable simplification. In short, the bilinear material model sufficiently captures the impact response while limiting solver run times. Here, the tangent modulus representing the plastic region was determined by calculating the slope of the line formed between the point of yielding and the point of failure in tension. Conversely, an elastic-perfectly plastic material model was used for the epoxy adhesive because its strain-hardening behaviour was not considered to be necessary for the impact simulation. The maximum equivalent failure strain criteria for the adhesive layer was the same as that for the core material since it was assumed that the adhesive simply increased the mass and stiffness of the core in the region it affected without affecting the failure of the cell walls.

Through trial and error, it was found that an indenter mass of 0.125kg for an an indenter velocity of 4m/s produced low-velocity impact damage within the the allowable damage limits. This corresponded to a 1J impact. Given the volume volume of the hemispherical indenter was 202.7mm^3, its density was specified as specified as 6.1667x10^{-4}kg/mm^3. The material properties used for the model are are presented in

Table 3.1 along with stress-strain curves in Figure 3.5.

Table 3.1: Model material properties [47].

	Indenter, structural steel	Skins, 7075-T6	Core, 5052-H32	Epoxy, HYSOL EA 934NA	Adhesive, W-direction	Adhesive, L-direction
Density [kg/mm^3]	6.17E-04	2.81E-06	2.68E-06	1.36E-06	2.43E-05	1.32E-05
Young's modulus [MPa]	200000	71700	70300	3790	103861	88650
Poisson's ratio [-]	0.3	0.33	0.33	0.3	0.3	0.3
Yield strength [MPa]	-	503	193	40	-	-
Tangent modulus [MPa]	-	670	298.5	0	-	-
Max. eq. plastic strain [mm/mm]	-	0.11	0.12	0.012	0.12	0.12

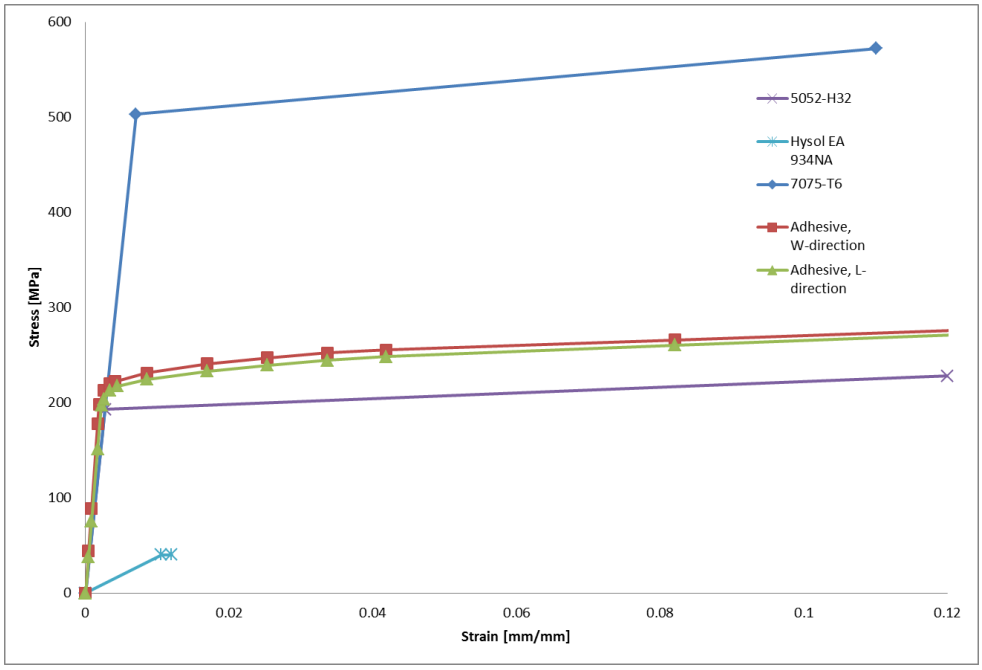

Figure 3.5: Model material stress-strain curves.

3.2.3. Element type and mesh

A free mesh of lower order quadrilateral shell elements using a uniform mesh method and a global element size of 0.465mm was used for the entire panel and indenter. For the core, this corresponded to 4 elements per cell wall. Higher order elements were not available in ANSYS using the explicit solver. A study on element size is presented in Subsection 3.3.3. The final mesh is shown in Figure 3.6.

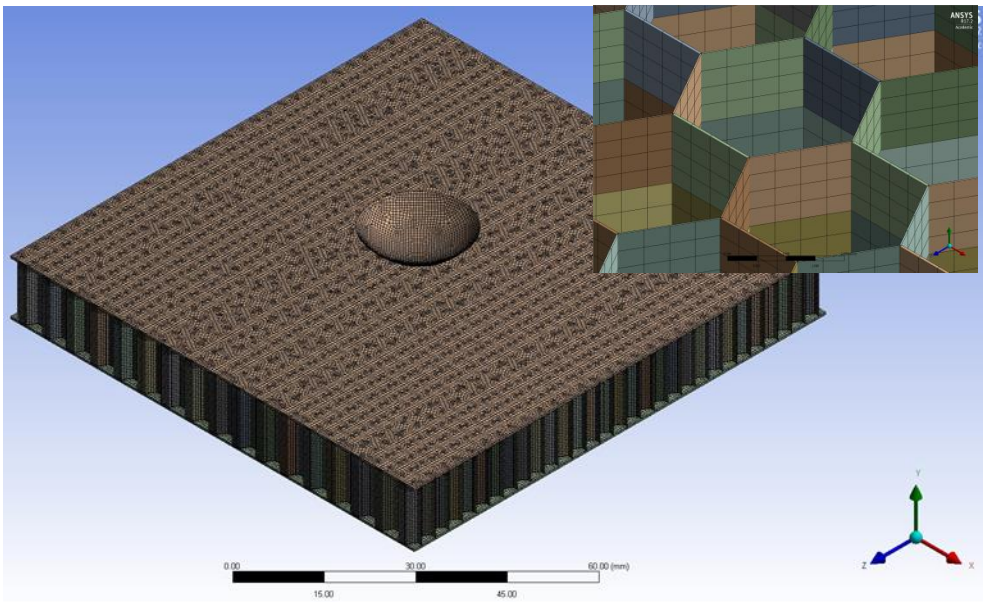

Figure 3.6: Model final mesh overview.

3.2.4. Loading and boundary conditions

The indenter impacted the top face sheet with a prescribed initial velocity of 4m/s in the face sheet normal direction. This velocity corresponded to 1J of kinetic energy and yielded dents within the allowable damage limits. Contact was defined between all bodies which enabled interactions between the indenter and face sheet and between cell walls as they

crumpled. Coefficients of static and dynamic friction of 0.61 and 0.47 respectively were assigned to all bodies [48].

The bottom face sheet was constrained in its normal direction to represent a panel sitting on a rigid surface. This was deemed acceptable given the overall deformation of a full size panel in service was expected to be small for low-velocity impacts. This boundary condition also improved damage repeatability. The sides of the panel including the outer core and face sheet edges were constrained from translating in their respective normal directions to represent an infinitely large panel.

3.2.5. Solution

An explicit solver was used exclusively with a single 1.36ms load step denoting the end of the impact stage. The solution included geometric and material non-linearity through local buckling of the core and plasticity in the face sheets and core. Element erosion was enabled, occurring only when the maximum equivalent plastic strain value specified in the material properties was exceeded. Under the same controls, the inertia of the eroded elements was retained.

3.3. Additional Model Development

Preliminary studies were performed in order to determine the most effective methods for representing an infinite panel, for representing the adhesive, and the element size appropriate for modelling both the first and second stage of the two-stage model. The results of these studies are presented in Subsections 3.3.1-3.3.3.

3.3.1. Effects of coupon size on damage

A series of simulations was completed to determine the coupon size that yielded a damage state representative of an infinite panel void of the influence from boundary conditions. Specifically, the coupon size was enlarged until the average equivalent face sheet stresses in the damage region were the same for a coupon with and without the sides constrained in their respective normal directions.

Three separate coupon sizes were considered, specifically:

- Coupon #1: *Small* – 49.5mm (1.95″) by 50.8mm (2″) (9 cells in the L-direction and 16 cells in the W-direction) or a surface area of 2514.6mm^2;
- Coupon #2: *Medium* – 82.5mm (3.247″) by 82.6mm (3.25″) (15 cells in the L-direction and 26 cells in the W-direction), or a surface area of 6814.5mm^2; and
- Coupon #3: *Large* – 93.5mm (3.6805″) by 95.2mm (3.75″) (17 cells in the L-direction and 30 cells in the W-direction), or a surface area of 8901.2mm^2.

The equivalent face sheet stresses were predicted from averaging the results at four separate locations in the damage region. An illustration of the locations is provided in Figure 3.7.

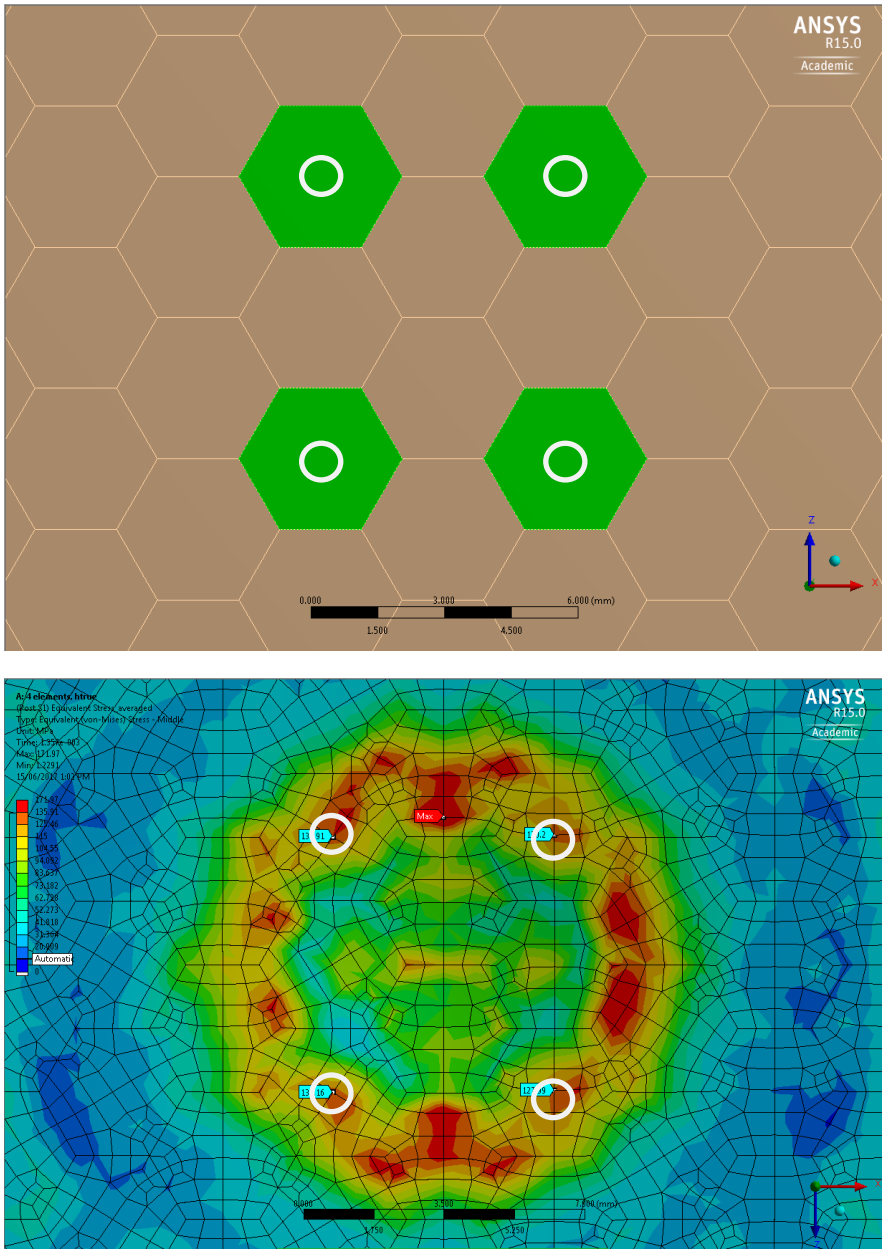

Figure 3.7: Top view of top face sheet showing locations where equivalent face sheet stresses were recorded (white circles).

The average face sheet stresses as a function of coupon size are provided in Figure 3.8. This shows that the stresses are roughly unchanged for the large

coupons, indicating that a panel with dimensions 93.5mm (3.6805″) by 95.2mm (3.75″) best represents an infinite panel for this damage state.

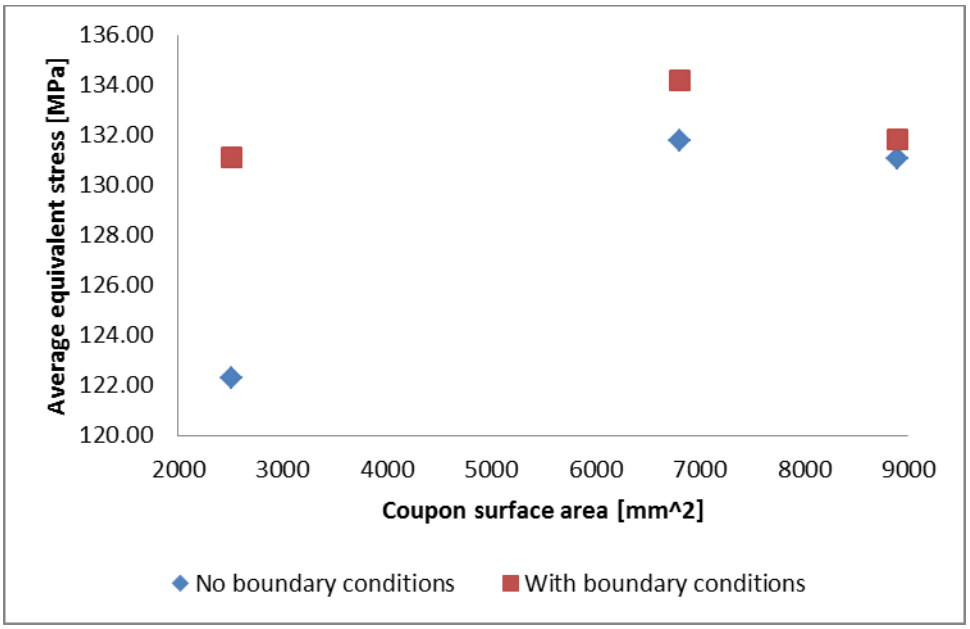

Figure 3.8: Plot of average equivalent face sheet stress in the damage region versus coupon surface area.

3.3.2. Adhesive representation and material property calibration

The adhesive was included in the model because it results in more accurate energy absorption [3] and core damage depth predictions [2]. Specifically, the primary purpose of modelling the adhesive in the manner outlined herein was to replicate the location of core buckling beneath the face sheet that was observed from panel sectioning [2]. In this section, a method for modelling the effects of the adhesive fillet without using a 3D geometric representation was devised. Instead, a layer of the core was sectioned 1.424mm below the top face sheet (Figure 3.2) and assigned material properties that had been calibrated to achieve the same overall stiffness as

the adhesive fillet in tension. This will be referred to as the representative adhesive layer. The material properties were calibrated based on a comparison with a fully 3D model of the adhesive fillet to ensure that the representative adhesive layer produced the same force-displacement response as the fillet. Specifically, two sets of material properties for the representative adhesive layer were determined: one for cell walls of regular thickness and another for the cell walls of doubled thickness.

A fully 3D, static model of a single cell wall with an adhesive fillet of radius 1.17mm was created as shown in Figure 3.9. The fillet radius was based on an average of the actual measured fillet radii in a honeycomb panel from one panel of the Griffon [2]. Symmetry conditions were imposed resulting in a quartered model of the 3D fillet. This was repeated for the doubled cell wall.

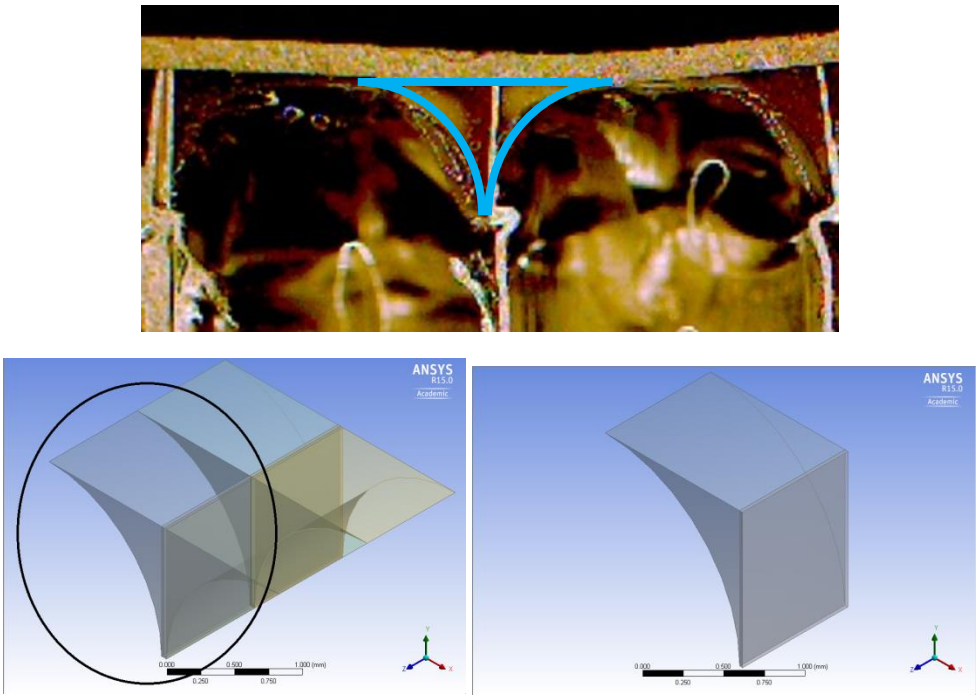

Figure 3.9: Side view of an adhesive fillet in a retired Griffon panel outlined in blue (top) [2], full adhesive geometry (bottom-left), quartered model (bottom-right).

The cell walls were made of 5052-H32 aluminum, and the fillet was made of HYSOL EA 934NA epoxy adhesive with the properties outlined in Table 3.2. The dimensions of the fillet test specimens are illustrated in Figure 3.10.

Table 3.2: HYSOL EA 934NA material properties [47].

	Epoxy, HYSOL EA 934NA
Density [kg/mm^3]	1.36E-06
Young's modulus [MPa]	3790
Poisson's ratio [-]	0.3
Yield strength [MPa]	40
Tangent modulus [MPa]	0
Max. eq. plastic strain [mm/mm]	0.012

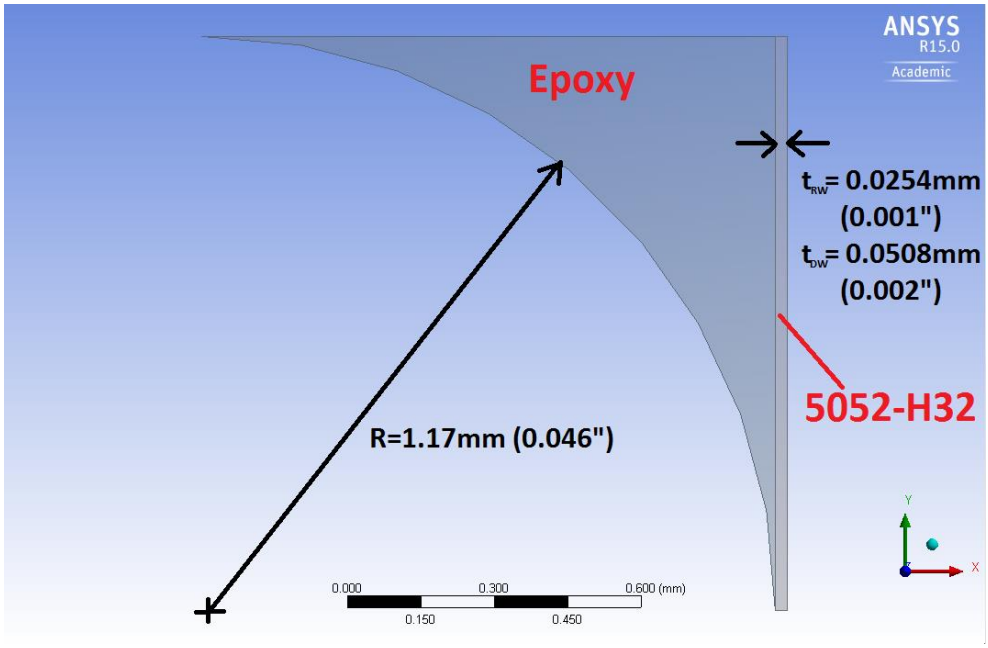

Figure 3.10: Front view of the fillet test specimen showing the radius and the thickness value for both the single cell wall (t_{RW}) and doubled cell wall (t_{DW}).

A vertical displacement was applied to the top face of the fillet to put the fillet fillet into tension and the resulting force reaction was recorded. Through trial and trial and error, ten displacements were considered sufficient for capturing the the elastic, plastic, and elastic-plastic transition zones. From these results, the the modulus of elasticity, true stress, and true plastic strain values were determined, together forming a set of strain-hardening curves representing the the behaviour of the 3D fillet. The strain-hardening data and curves are shown in

shown in

Table 3.3 and Figure 3.11, respectively. The masses and volumes of both models were also noted.

Table 3.3: 3D fillet strain-hardening data.

3D fillet, single cell wall thickness		**3D fillet, doubled cell wall thickness**	
Stress	*Strain*	*Stress*	*Strain*
[MPa]	[mm/mm]	[MPa]	[mm/mm]
197.58	0.0000	196.42	0.0000
212.87	0.0005	204.39	0.0003
219.54	0.0013	212.43	0.0010
222.17	0.0020	217.24	0.0020
230.86	0.0063	224.50	0.0060
240.49	0.0146	232.99	0.0143
247.11	0.0229	239.11	0.0226
251.90	0.0312	244.03	0.0309
254.99	0.0394	248.08	0.0390
265.42	0.0795	260.24	0.0791
275.93	0.1180	270.63	0.1176

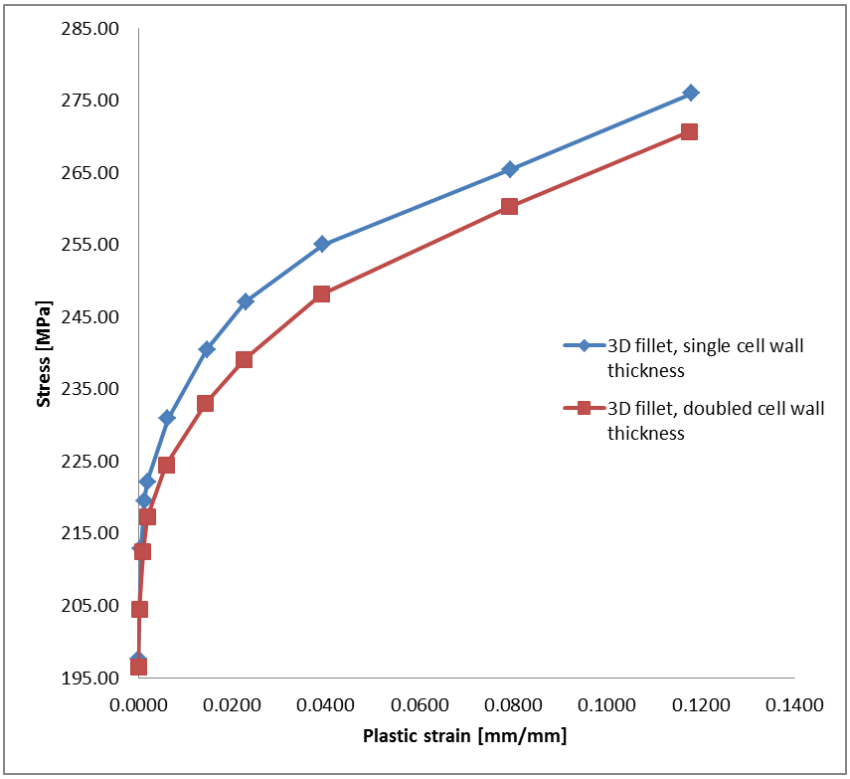

Figure 3.11: 3D fillet strain-hardening curves.

The results from the 3D fillet model were then used to calibrate the material properties for the representative adhesive layer. A model with only the cell wall was created for representing the top 1.424mm section of the core, as shown in Figure 3.12.

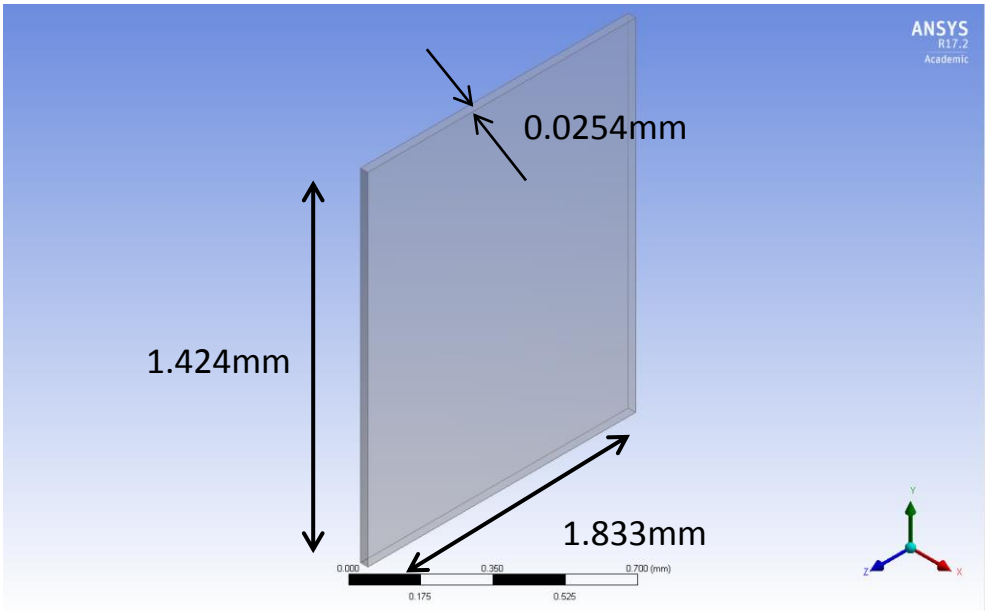

Figure 3.12: Overview of single cell wall in the representative adhesive layer with dimensions shown.

This model consisting of a single cell wall in the representative adhesive layer was assigned the material properties that were calibrated from the 3D fillet model in order to yield the same force-displacement curve. Poisson's ratio was kept the same, the modulus of elasticity was based on the force-displacement curve of the 3D fillet model, and the density was adjusted to reflect the same mass. Despite both model variants having the same mass of adhesive, the density of the cell walls of single thickness in the adhesive layer was roughly twice that of the cell walls of doubled thickness in the adhesive layer. Specifically, the mass and volume of the 3D fillet model with the single cell wall thickness were 1.61x10-6kg and 0.0663mm^3, respectively. The mass and volume of the 3D fillet model with the doubled cell wall thickness were 1.76x10^{-6}kg and 0.1326mm^3, respectively. Hence, a

combination of a similar mass and higher volume translated to a lower density for the doubled cell wall model. These properties are provided in

Table 3.4. Figure 3.13 shows the force-displacement curves for the single cell wall models in the representative adhesive layer compared with the 3D fillet models.

Table 3.4: 3D fillet test specimen material properties.

	Density [kg/mm^3]	*Young's modulus* [MPa]
Core, 5052-H32	2.68E-06	70300
Adhesive, HYSOL EA 934NA	1.36E-06	3790
Core & **Adhesive,** single thickness	2.43E-05	103861
Core & **Adhesive,** doubled thickness	1.32E-05	88650

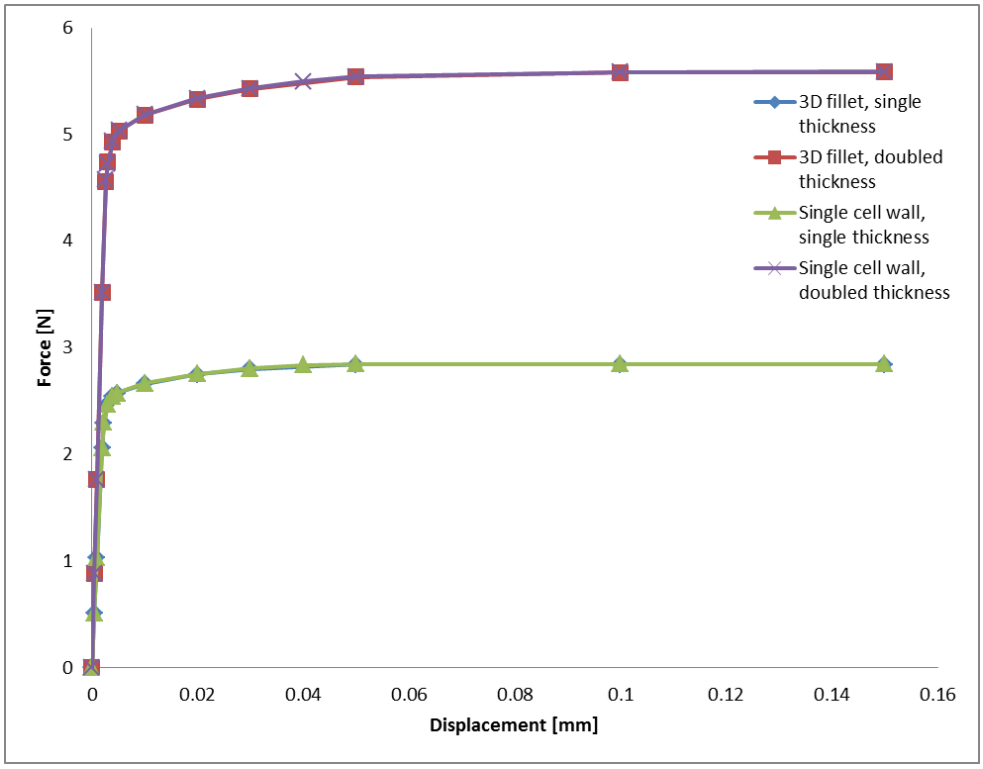

Figure 3.13: 3D fillet model and representative adhesive layer load-displacement curves.

The modulus of elasticity of the representative adhesive layer with the single cell wall thickness was increased by 48% from the original value for 5052-H32, and by 26% for the doubled cell wall thickness to account for the presence of the adhesive fillet. Furthermore, the force-displacement curve comparison shows that the representative adhesive layer can replicate the mechanical response of the 3D fillet in tension.

The presence of the representative adhesive layer in the sandwich panel produced the offset to the localized core buckling observed by Reyno [2] and increased the energy absorbing capacity. Specifically, Figure 3.14 illustrates side views of the sectioned coupon along the W- and L-directions and shows that core damage is offset by the depth of the adhesive layer, in contrast to the equivalent model with no adhesive layer. The energy absorbed by the coupon was derived from the difference

between the ingoing and outgoing indenter velocity. It was found that 1.5% more energy was absorbed with the representative adhesive layer compared to a model without it. These findings are consistent with observations by Reyno [2] and those published by Zhang [3] [9] and Okada [32].

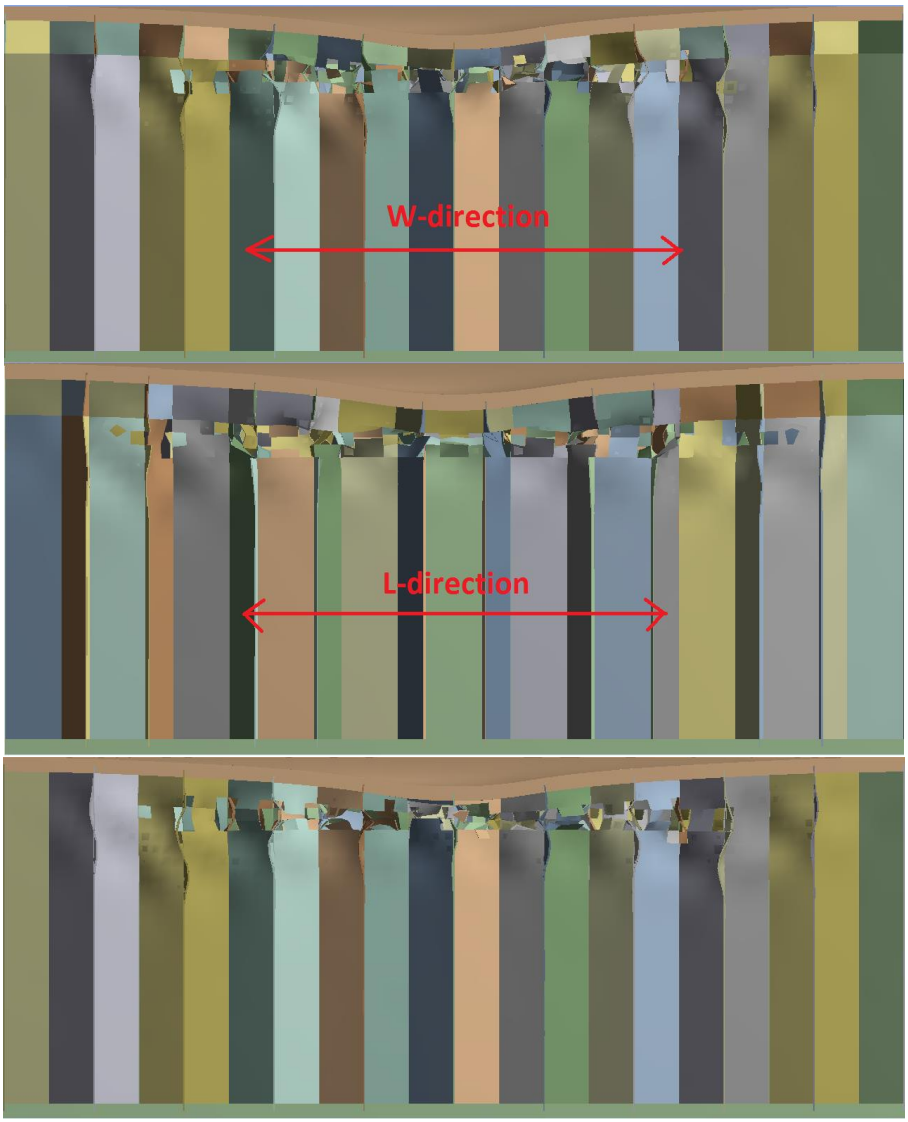

Figure 3.14: Side views of coupon sections along the W- and L-directions (top and middle, respectively) that show localized core buckling below the representative adhesive layer compared to a model with no adhesive (bottom).

3.3.3. Element size

The purpose of this study was to determine the element size suitable for replicating the damage observed from sections of a retired Griffon panel. Various element sizes based on the number of elements across a single cell wall were considered for a variant of the model representing an infinite panel, but with a 47% smaller coupon size (Coupon #1) to minimize run times. The appropriate element size was gauged primarily through visual comparison of the core damage results. The influence of the element size on the residual dent depth, core damage depth and width, equivalent face sheet stresses, peak impact force, energy absorbed and the solver run times were also determined.

The same parameters from the model were used, including a 4m/s indenter velocity and 1J impact energy. Element sizes of 1mm, 0.625mm, 0.465mm, and 0.37mm were considered, corresponding to 2, 3, 4, and 5 elements per cell wall, respectively. The representative adhesive layer was also included. The meshes for 2 and 4 elements per cell wall are shown in Figure 3.15 and Figure 3.16.

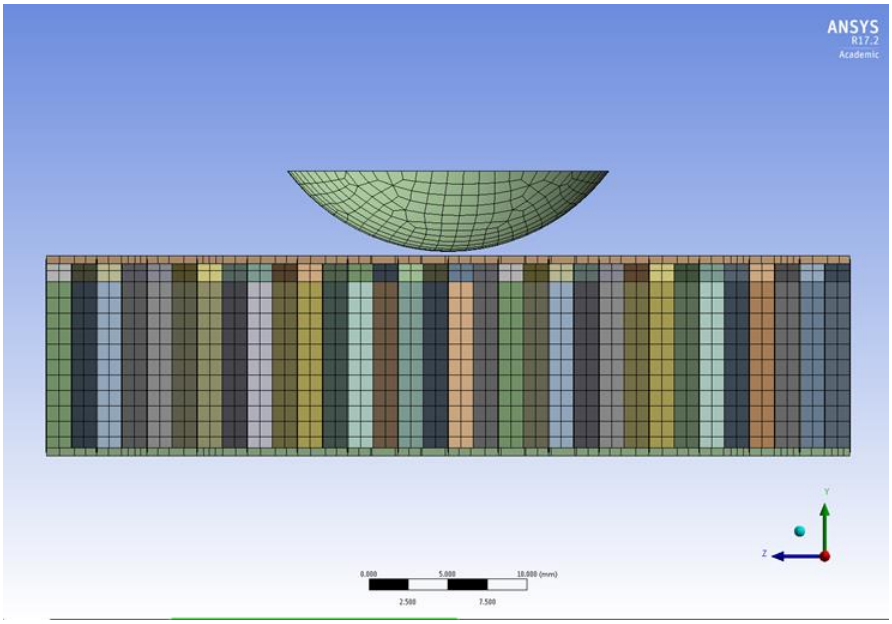

Figure 3.15: Side view of small coupon mid-section mesh with 2 elements per cell wall.

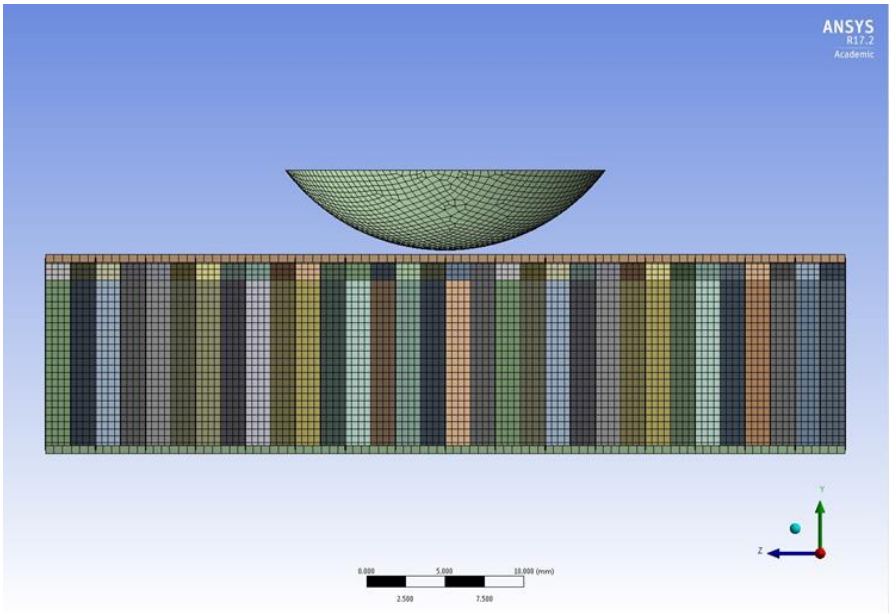

Figure 3.16: Side view of small coupon mid-section mesh with 4 elements per cell wall.

Solver run times increased with increasing mesh density, as shown in Figure 3.17. As a result, element sizes greater than 5 elements per cell wall were excluded because they were taking 45 hours to run on a computer with 64GB of RAM and an Intel® Xeon processor for the model with the small coupon size. These run times would have been undoubtedly worse for the required coupon size representing an infinite panel.

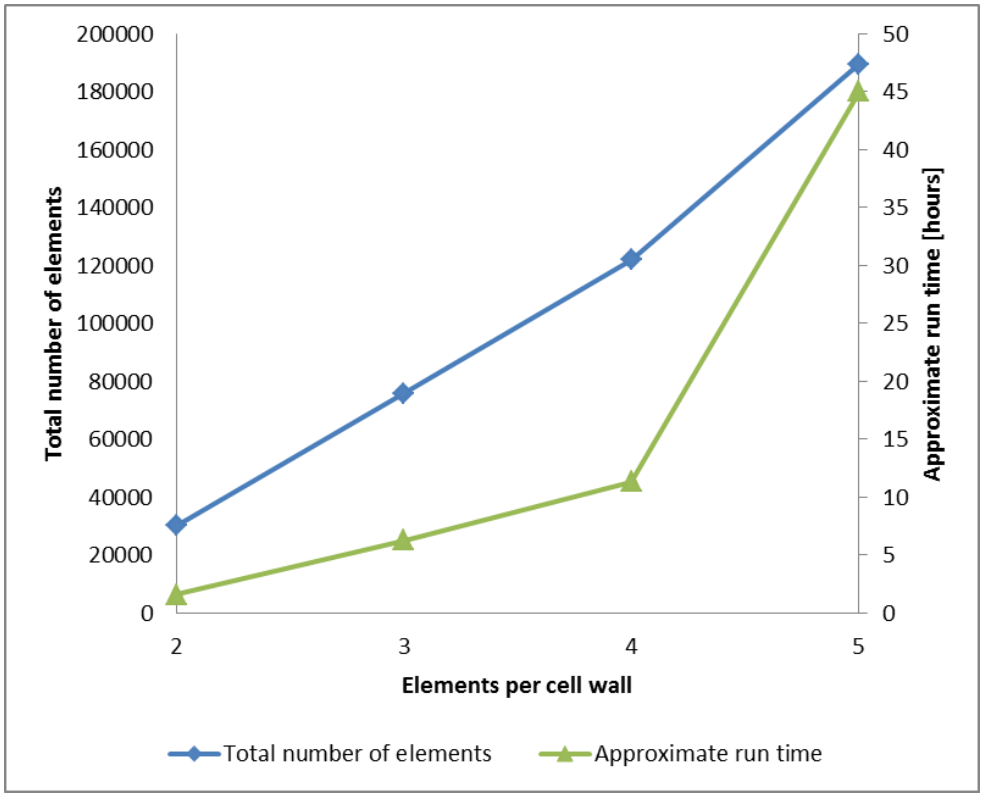

Figure 3.17: Plot of approximate solver run time and total number of elements versus meh density (number of element per cell wall).

Residual dent depth was predicted by the displacement of the top face sheet at the centre of the dent. A plot of residual dent depth versus the number of elements per cell wall is shown in Figure 3.18. The dent depth varied between 0.99mm and 1.04mm for the four different element sizes, which was within the range of the dents present on the Griffon panel [2]. This range had a maximum percent difference of 5%, a 2% difference between the meshes with 2 and 5 elements per cell wall, and a 1%

difference between the meshes with 4 and 5 elements per cell wall. This confirmed that a mesh with 4 elements per cell wall was sufficient for predicting dent depth.

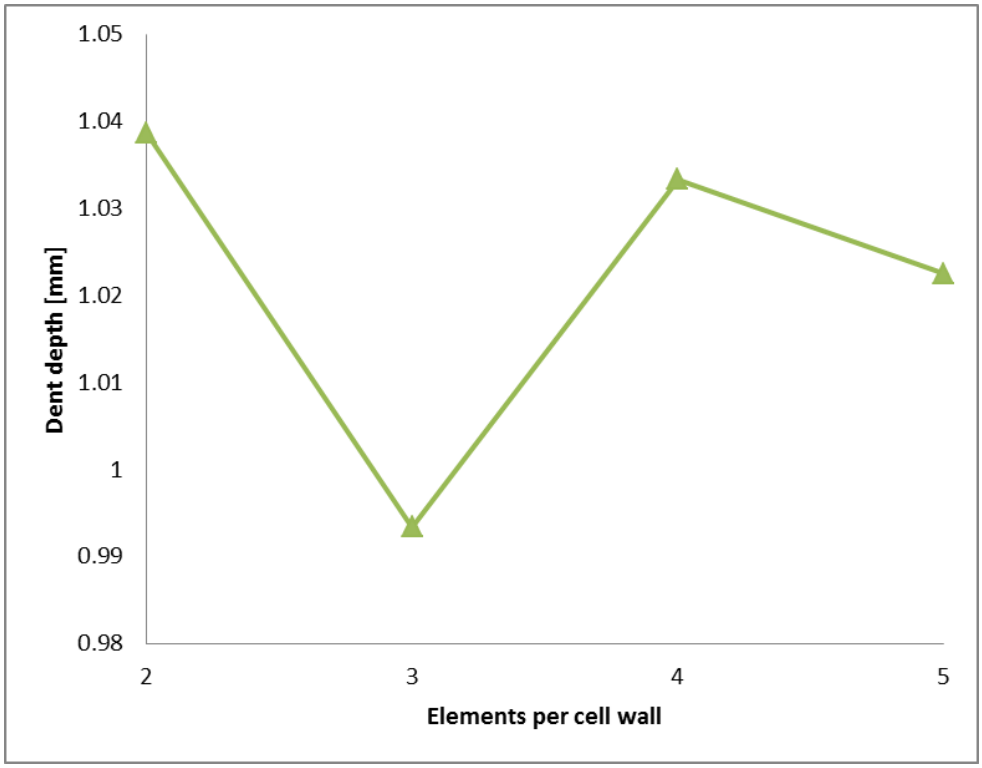

Figure 3.18: Plot of residual dent depth versus number of elements per cell wall.

Core damage depth and width were predicted from the equivalent plastic strain results at coupon mid-span from slices along the W- and L-directions, respectively. The results were scaled so that the minimum plastic strain value displayed was 0.0005mm/mm. This value was selected for outlining the region of core yielding, and also for enabling consistent and comparable predictions using ImageJ. For each cell with damage greater than this value, a damage depth was recorded. The damage depth values cited herein represent averages of the damage depth in each of the cells meeting the aforementioned criterion. In a similar fashion, core damage width was predicted from the left and right extremities of the core damage region in cell wall increments. This method for measuring core

damage is consistent with that used by Clarke [26]. Illustrations of the equivalent plastic strain results for a W-direction slice at coupon mid-span are provided in Figure 3.19-Figure 3.22 for the four different mesh sizes.

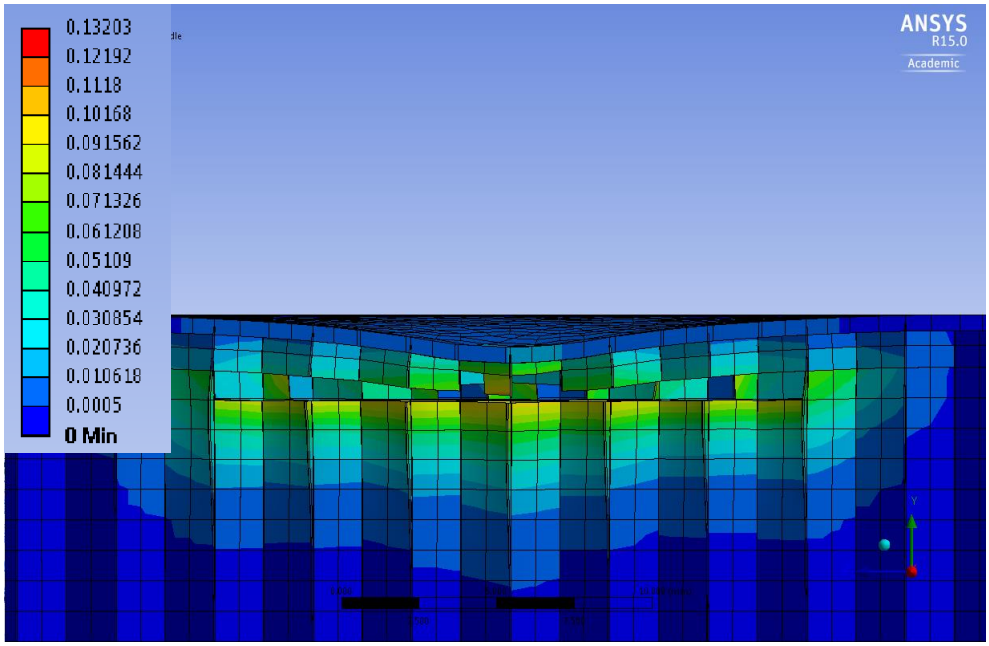

Figure 3.19: Side view of equivalent plastic strain results for a W-direction slice at coupon mid-span in the model with 2 elements per cell wall.

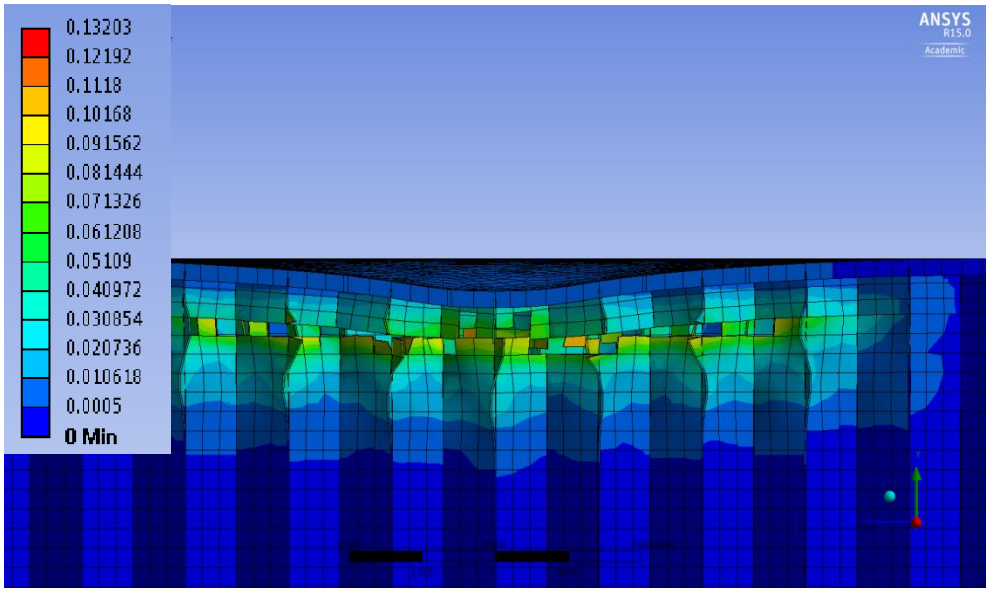

Figure 3.20: Side view of equivalent plastic strain results for a W-direction slice at coupon mid-span in the model with 3 elements per cell wall.

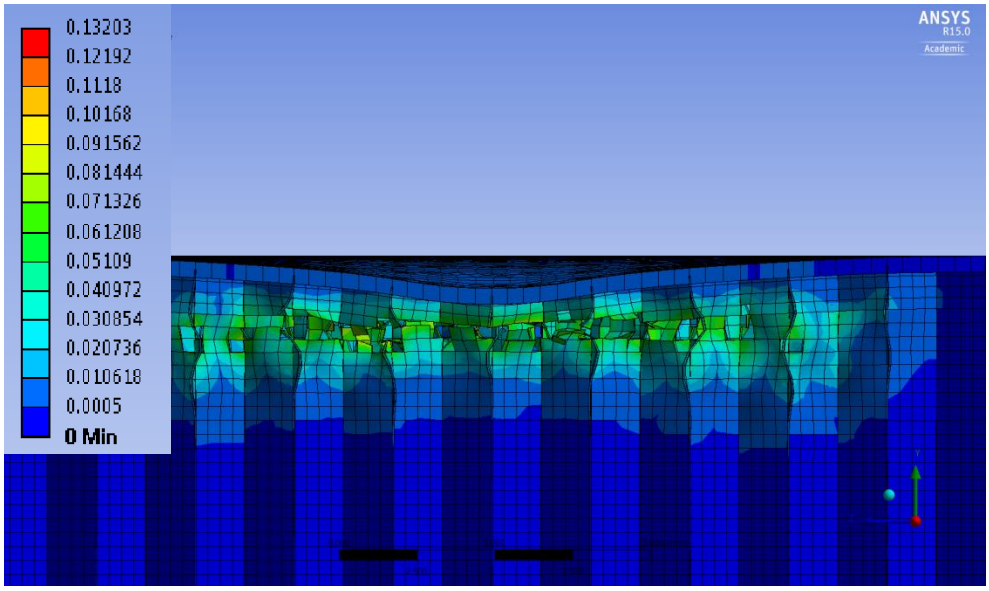

Figure 3.21: Side view of equivalent plastic strain results for a W-direction slice at coupon mid-span in the model with 4 elements per cell wall.

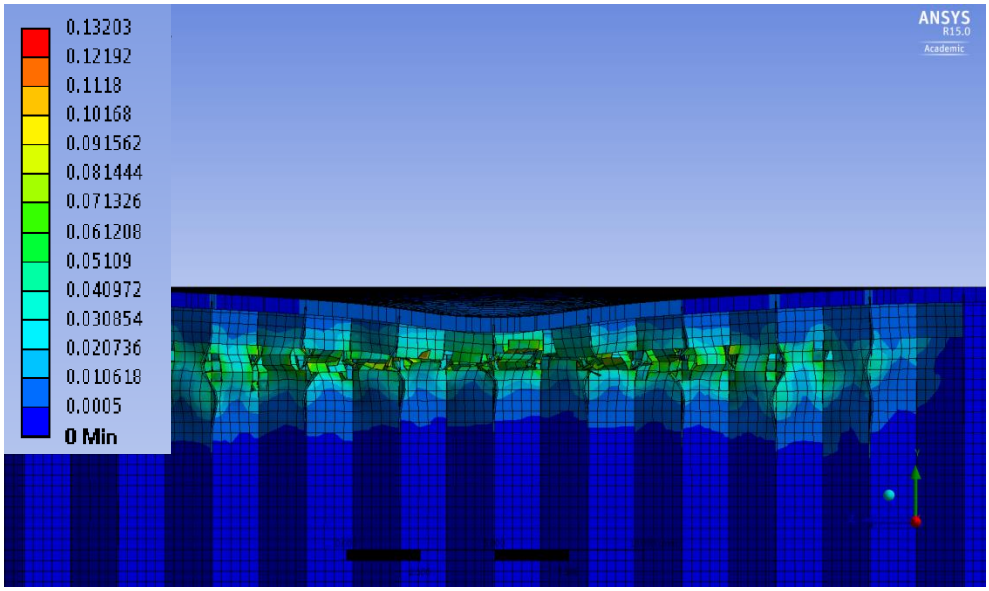

Figure 3.22: Side view of equivalent plastic strain results for a W-direction slice at coupon mid-span in the model with 5 elements per cell wall.

These results show that a layer of eroded (or deleted) elements develops in the core, indicating that these have exceeded the maximum equivalent plastic strain failure criteria. This effectively predicts core separation and could indicate core cracking. Though the overall shape of the deformed core compared well against that from sections of a retired Griffon panel, core cracking was not observed [2].

This layer of eroded elements grows horizontally, and element erosion becomes more influential as mesh density decreases. This is due to the comparatively larger artificial stiffness for coarser meshes resulting from limited degrees of freedom in the core mesh which otherwise facilitate element rotation and further cushion impact. In other words, large elements in a coarse mesh will erode sooner than the small elements in a fine mesh. This is illustrated in Figure 3.23.

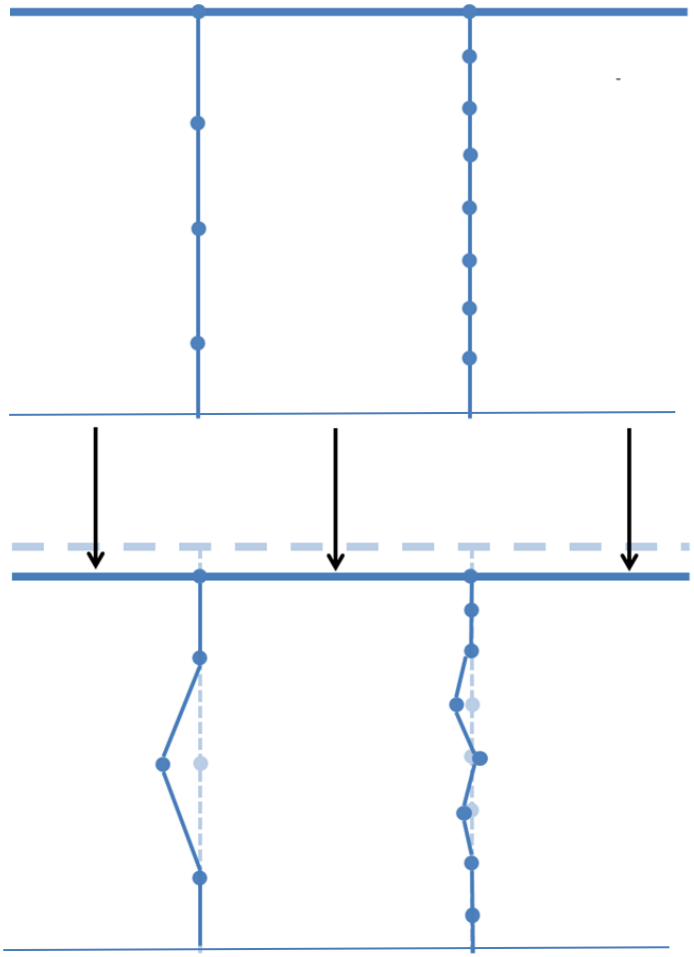

Figure 3.23: Illustration of buckling in a coarse core mesh (left) and a fine core mesh (right). The circles denote the nodes in the core, and the top line indicates the compression of the top face sheet under impact.

A summary of these results are shown in Figure 3.24 in the form of a plot of core damage width and average core damage depth versus the number of elements per cell wall.

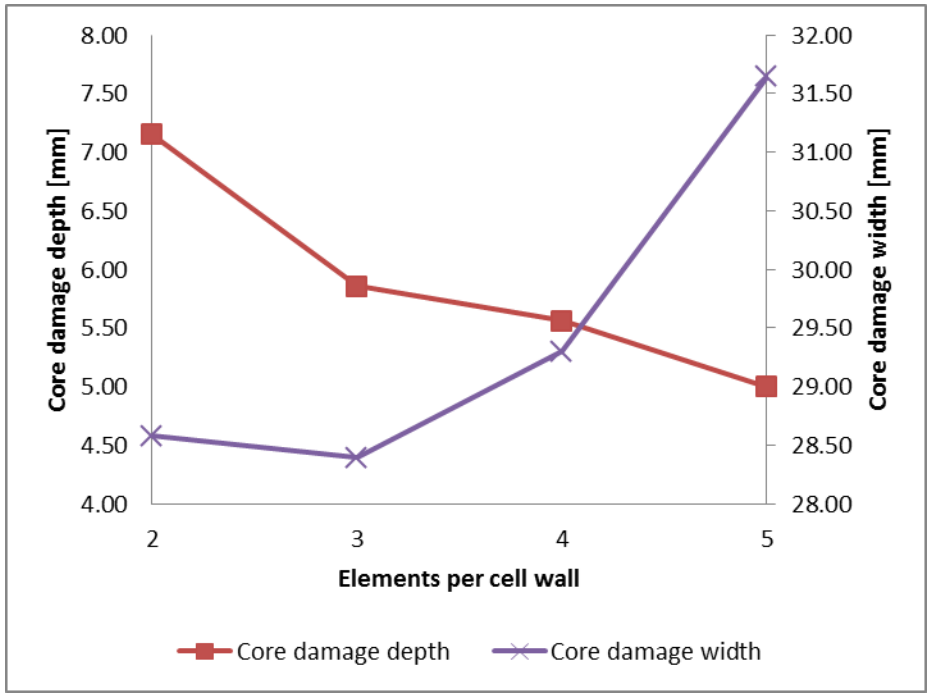

Figure 3.24: Plot of core damage width and average core damage depth versus number of elements per cell wall.

The core damage depth decreases, but the width increases with more elements. Furthermore, convergence did not occur; the percent differences for core damage depth and width between the meshes with 4 and 5 elements per cell wall are 10% and 4%, respectively.

In contrast to the core damage observed from the sectioned panel specimens (as shown in Figure 2.4- of Subsection 2.4.3), the models with 4 and 5 elements per cell wall and a representative adhesive layer compared well qualitatively based on the offset localized buckling and the overall shape of the deformed core. The buckling observed in the physical panels was more pronounced than that from the models, but both the model and the physical panels showed 2- and 3-lobe folding [2]. This is further illustrated Figure 3.25 in a side-by-side comparison of an example of real core damage [2] from a retired Griffon panel and the core damage from models with 4 and 5 elements per cell and the representative adhesive layer, respectively.

Figure 3.25: Comparison of core damage in a real dent [2] (top) and in the representative adhesive layer models with 4 (middle) and 5 (bottom) elements per cell wall.

The average core damage depth measured by Reyno [2] was 2.66 ± 0.85 mm based on 20 dents. This was defined as the vertical distance between the undented face sheet and the maximum depth of core crushing. Based on this definition, the current prediction based on the model with 4 elements per cell wall was 4.3mm averaged across the damaged cells. It is expected that this figure would decrease with increasing mesh density and converge to the value recorded by Reyno [2].

Peak impact force was predicted directly from the software through the force reaction results recorded at the bottom boundary condition, and the energy absorbed by the coupon was derived from the ingoing and outgoing indenter velocities. A plot of energy absorbed by the coupon and peak impact force versus the number of elements per cell wall is provided in Figure 3.26.

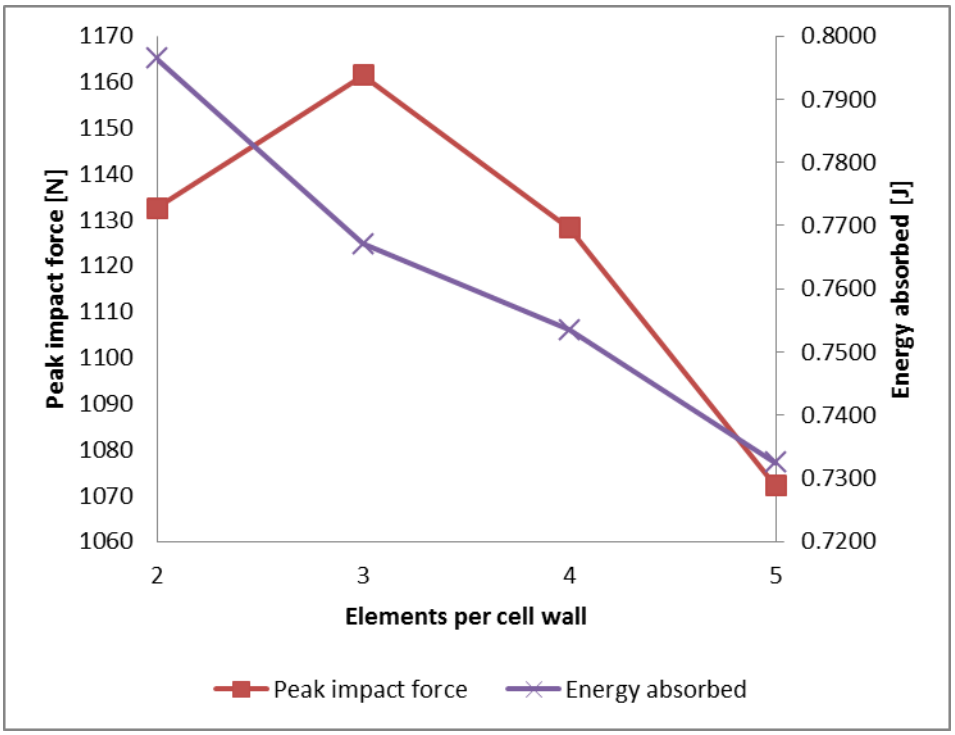

Figure 3.26: Plot of energy absorbed by the coupon and peak impact force versus number of elements per cell wall.

As the number of elements increased from 3 to 5 elements per cell wall, both the peak force and the absorbed energy decreased. The percent differences between 4 and 5 elements per cell wall for the peak impact force and energy absorbed were 5% and 3%, respectively.

Upon analysis of the results, it was found that a finer mesh decreases the apparent stiffness due to increased degrees of freedom and deformation capacity in the core mesh. Finer meshes result in a lower peak impact force and deeper face sheet dents. In such cases, core damage depth is shallow and core damage width is large. The former is a result of localized deformation attributed to a finer mesh, and the latter is attributed to a more flexible core which makes it such that bending of the impacted face sheet is facilitated.

One would expect that as peak impact force decreases the energy absorbed by the coupon increases. This was not so due to the element erosion feature. Essentially, a void made by the eroded elements that have exceeded the failure criterion resulted in a trampoline effect whereby the face sheet in this region was left unsupported. This void was much larger for the mesh of 2 elements per cell wall, as shown in Figure 3.19. During impact, the face sheet absorbed most of the energy from the indenter through yielding, as shown in Figure 3.27 and Figure 3.28. Thus, the finer the mesh, less yielding and energy absorption occurred in the face sheet.

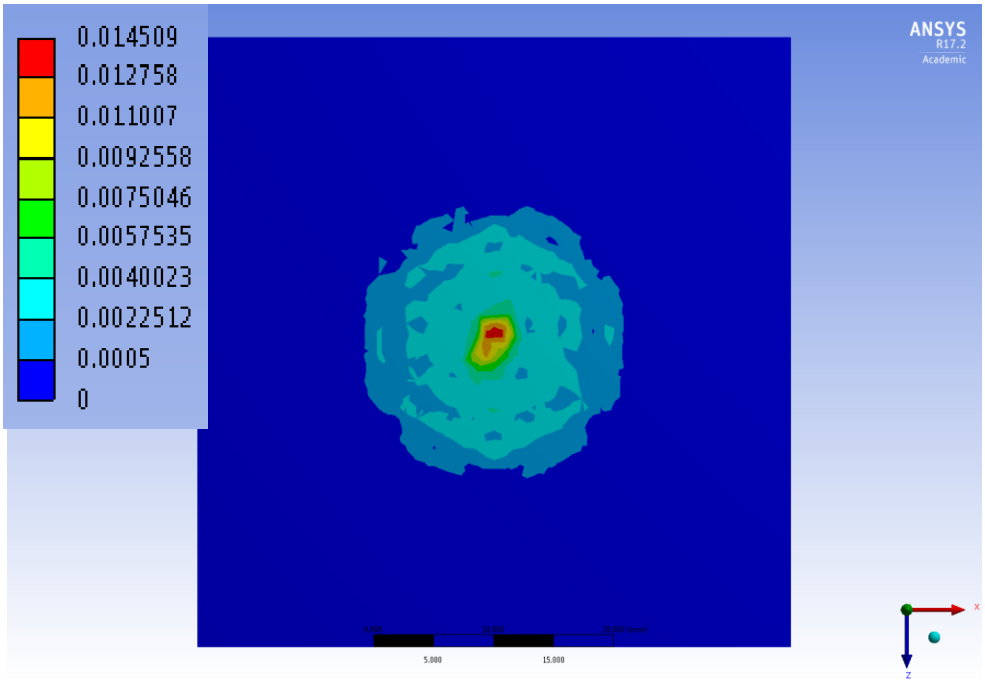

Figure 3.27: Top view of equivalent face sheet plastic strain results for the model with 2 elements per cell wall.

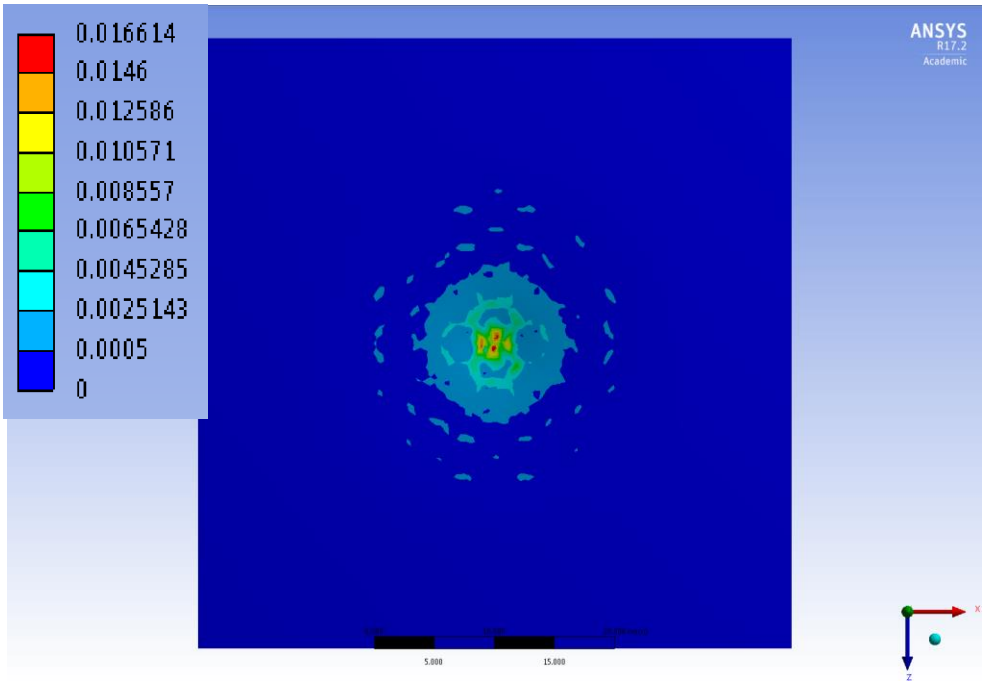

Figure 3.28: Top view of equivalent face sheet plastic strain results for the model with 5 elements per cell wall.

The equivalent face sheet stresses were predicted via the same method described in Subsection 3.3.1. Illustrations of these stresses are provided in Figure 3.29-Figure 3.31 for 2, 4, and 5 elements per cell wall, respectively.

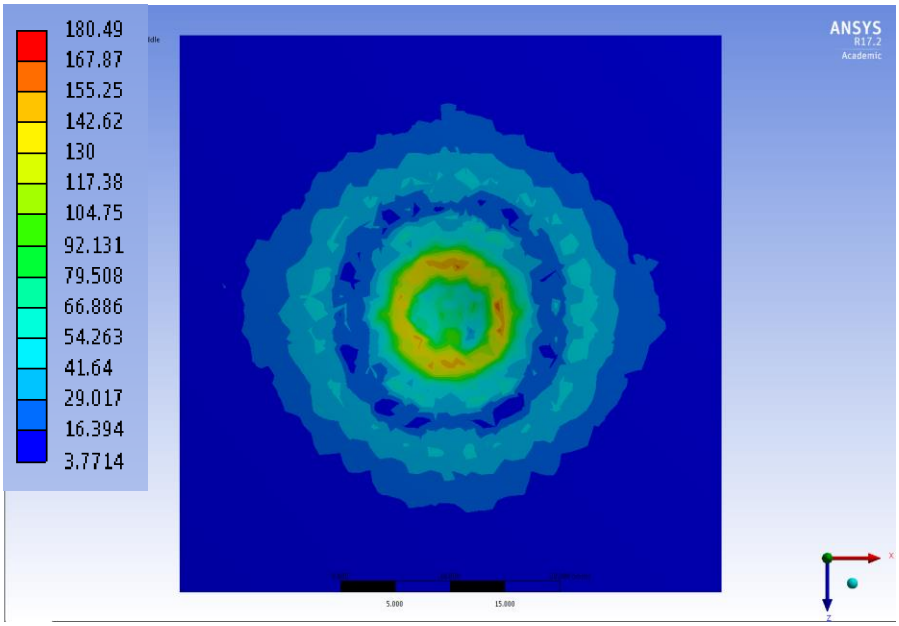

Figure 3.29: Top view of equivalent face sheet stresses [MPa] for the model with 2 elements per cell wall.

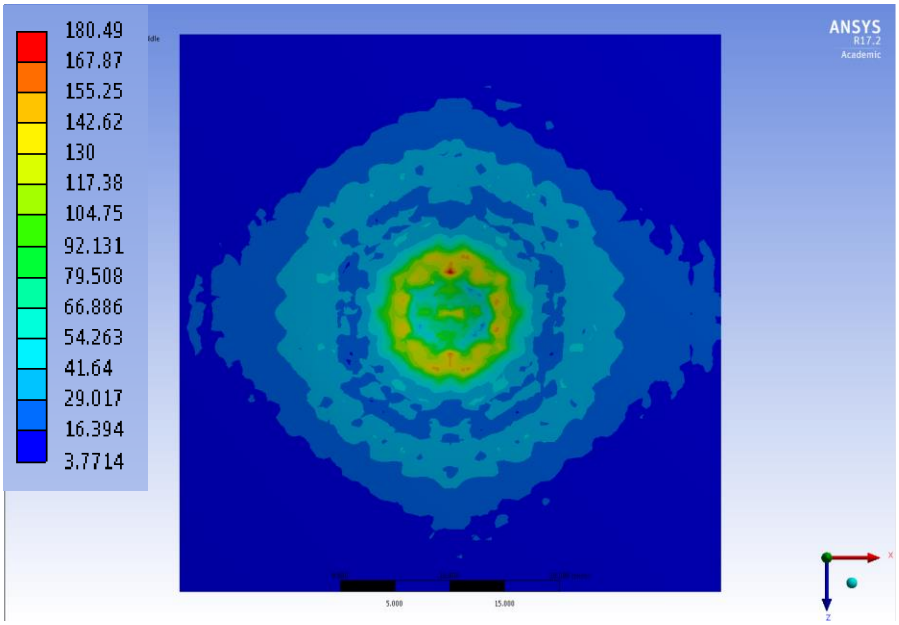

Figure 3.30: Top view of equivalent face sheet stresses [MPa] for the model with 4 elements per cell wall.

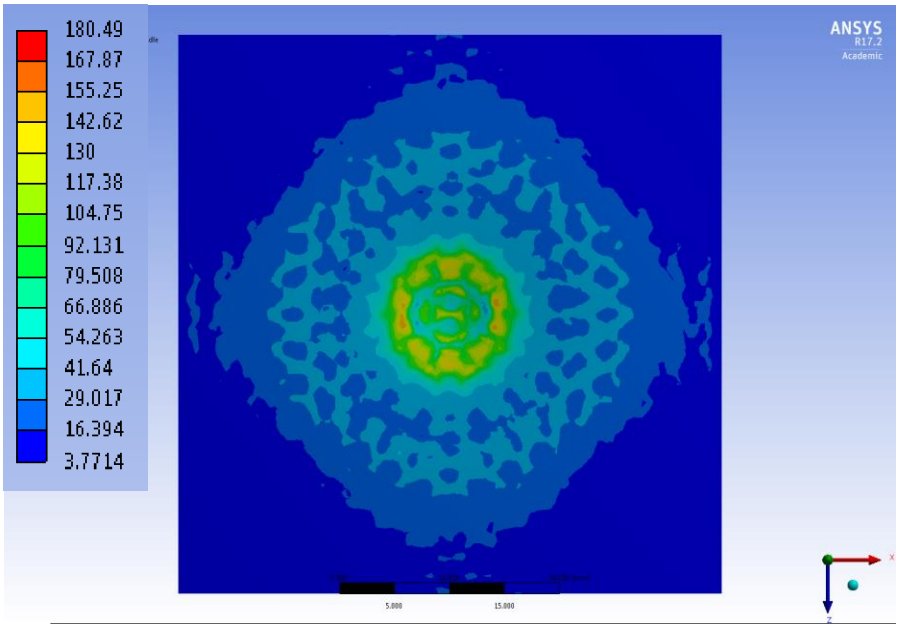

Figure 3.31: Top view of equivalent face sheet stresses [MPa] for the model with 5 elements per cell wall.

The overall pattern is largely unchanged from 4 to 5 elements per cell wall with a slight increase in the size of the 16-30MPa band and a subtle smoothening out of the 30-40MPa band. More importantly, the size and shape of the ring of high stresses (55+MPa) located in the impact region remains roughly the same. A plot of average equivalent face sheet stress in the damage region versus the number of elements per cell wall is shown in Figure 3.32.

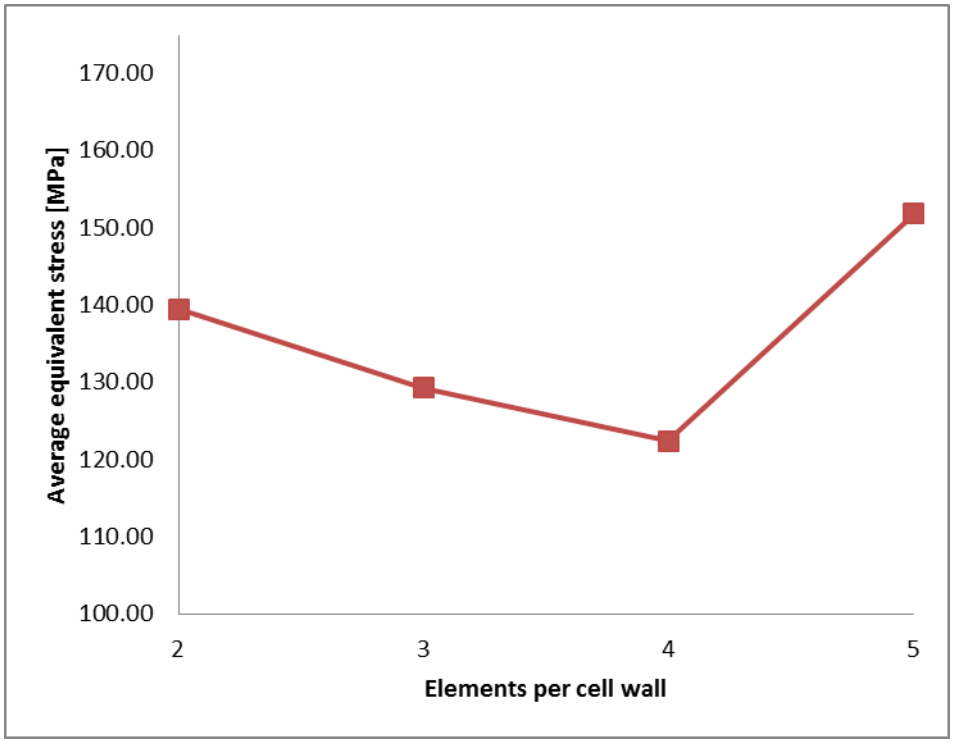

Figure 3.32: Plot of average equivalent face sheet stresses in the damage region versus number of elements per cell wall.

Here, convergence did not occur for the stress results; there was a percent increase of 24% from 4 to 5 elements per cell wall. This is largely attributed to locally high stresses where the cell walls and face sheet meet. Since the 3D fillet geometry was not modeled, the alternative adhesive modelling method presented herein may be the cause for artificially higher local stresses in the face sheet. Despite this, the overall shape and size of both the extended stress distribution and ring of maximum stresses were roughly unchanged. Since the goal of the current work is to predict percent increases in equivalent face sheet stresses, the mesh sizing is not as critical as when absolute values of stress are required.

In summary, a mesh with a global element size of 0.465mm corresponding to 4 elements per cell wall was chosen for best representing core damage observed in the retired Griffon panels and the overall face sheet stress distribution at reasonable run times. Though convergence did not occur for

the maximum stress values, finer meshes would have been required to achieve convergence resulting in excessive run times. To put this into perspective, there was a 300% increase in run time from 4 to 5 elements per cell wall. This increase would be compounded by the second stage consisting of the post-impact tensile load which would add 10 hours to the run time for 4 elements per cell wall and 36 hours for 5 elements per cell wall. Nonetheless, it is recommended that finer meshes be considered in order to achieve convergence in the percent increases in equivalent face sheet stresses.

4. Modelling post-impact tensile loading

4.1. Introduction

The purpose with this phase of modelling was to develop a method for predicting face sheet stresses for a panel loaded in tension with pre-existing low-velocity impact damage. This was achieved using a two-stage sequential loading simulation consisting of an impact stage followed by a tensile loading stage. During the first stage of loading, the indenter impacted the panel with a specified velocity using the model previously described in Chapter 3. Once the indenter had rebounded and face sheet spring-back had occurred, a second loading stage was defined where a tensile load was applied to the panel through a prescribed displacement. Both stages of loading were incorporated into a single continuous run as illustrated in Figure 4.1. The top graphic shows the core and surface damage resulting from the impact stage, and the bottom shows an applied displacement to the same panel using the predicted damage state.

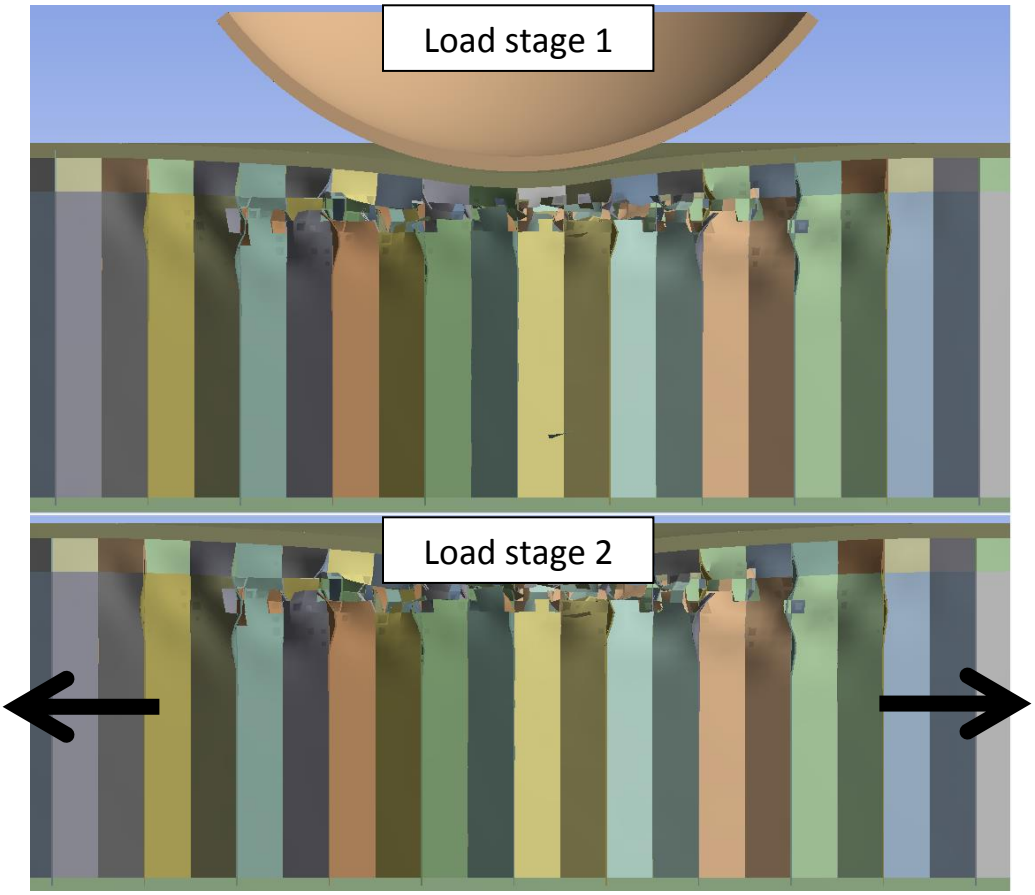

Figure 4.1: Side view of the model with a W-direction slice at coupon mid-span for the impact stage (top) and post-impact tensile loading stage (bottom).

4.2. Model methodology

The model was a continuation of the model presented in Chapter 3 which consisted of a hemispherical indenter with a prescribed velocity of 4m/s, a panel with 5.08mm thick aluminum face sheets, and featured a representative adhesive layer. In addition to this, a tensile loading stage was added post-impact. Possible failure modes in metallic honeycomb

panels could be the formation of cracks in the face sheet or in the core due to fatigue loading, or local buckling of the face sheet under compressive or bending loads. A tensile load case was chosen for the current study to address potential cracking in the impacted face sheet due to tensile fatigue loads. Any localized stress increases in the face sheet could result in a reduction in fatigue life. Tensile loads yield a simpler and more predictable stress state and failure mode than compressive loads and could also be tested experimentally without any custom fixtures.

The boundary conditions remained the same as the impact stage with the bottom surface and three of the sides constrained in their normal directions. The only change was that for the second loading stage, the constraint was removed from one face and replaced with a 0.1mm applied displacement, as indicated in Figure 4.2. A 0.1mm displacement was arbitrarily selected since percent increases in stress were sought, and because it did not produce additional plasticity in the coupon which is typical of fatigue loads where stresses are much lower than the yield stress of the material.

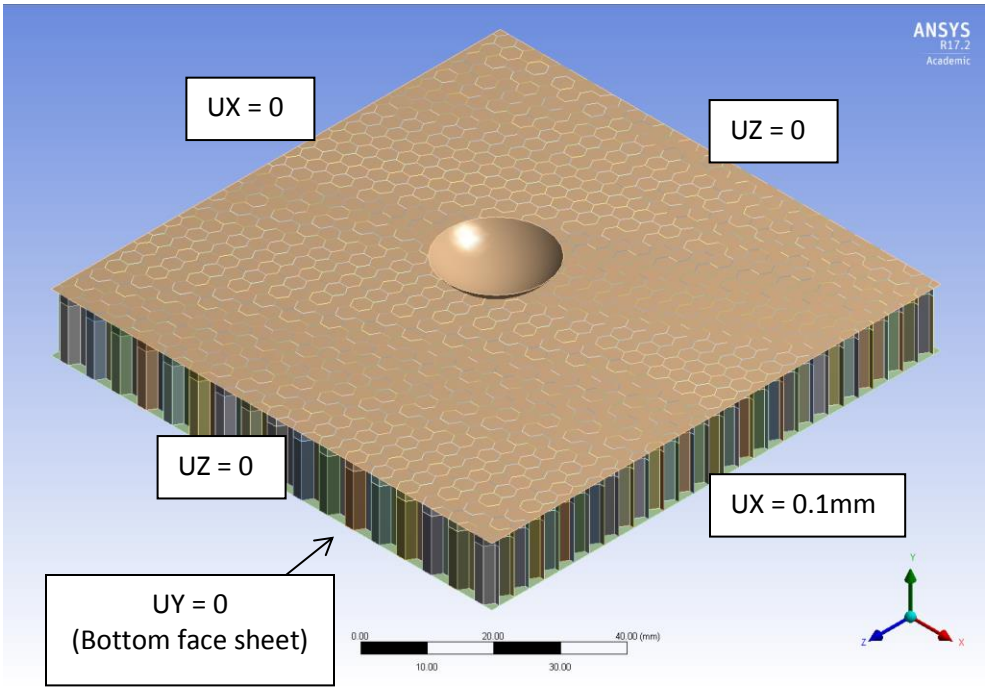

Figure 4.2: Overview of post-impact loading boundary conditions.

The tensile loading stage occurred over 1ms which resulted in an overall simulation end time of 2.36ms when the 1.36ms impact stage was considered. A duration of 1ms was a sufficient length of time for representing a static load despite the fact that it was applied dynamically using an explicit solver. In the literature, explicit and implicit solvers have both been used to model the impact event and the post-impact loading. Fischer et al. [40] conducted numerical CAI tests using an explicit solver and a two-stage modelling approach, while Aminanda et al. [37] used an implicit solver for modelling static indentation followed by CAI. Both approaches showed good agreement with experiments in terms of residual strength predictions and damage growth. The use of an explicit solver for modelling the process of an event causing plasticity followed by the addition of a static load was verified, as presented in the following section.

4.3. Verification

In order to verify the two-stage loading approach for predicting face sheet stresses in panels with impact damage, the same approach was applied to a simple dog bone geometry in uniaxial tension and the results were compared to an analytical solution. This comparison verified that the plastic strain induced during the first loading stage was correctly incorporated into the second loading stage where the static tensile load was applied. The uniaxial simulation was performed using an implicit and explicit solver to confirm that either one could be used as long as the loads were applied at a slow enough rate to minimize dynamic effects.

The uniaxial dog bone specimen shown in Figure 4.3 had a cross-section of 3mm by 9.525mm and was modeled using planes of symmetry on faces A and B. A yield stress of 280MPa, Young's modulus of 71,000MPa, and a tangent modulus of 500MPa were used to define the stress-strain curve. Two tensile loading stages were applied sequentially. In the first stage, the specimen was subjected to a tensile load of 5400N which was large enough to induce plasticity. This load was then removed and the stress in the specimen returned to zero while plastic strain remained. In the second stage, a tensile load of 2500N which was small enough to keep the specimen in the elastic range was applied. The maximum normal Y-Axis true stress value and plastic strain at the end of the second stage of loading was recorded. When the explicit solver was used, the plasticity-inducing load was applied over 10ms and the second load was applied over 2ms. These durations were selected to minimize dynamic effects and to enable comparison of results at the end of the simulation between explicit and implicit solvers.

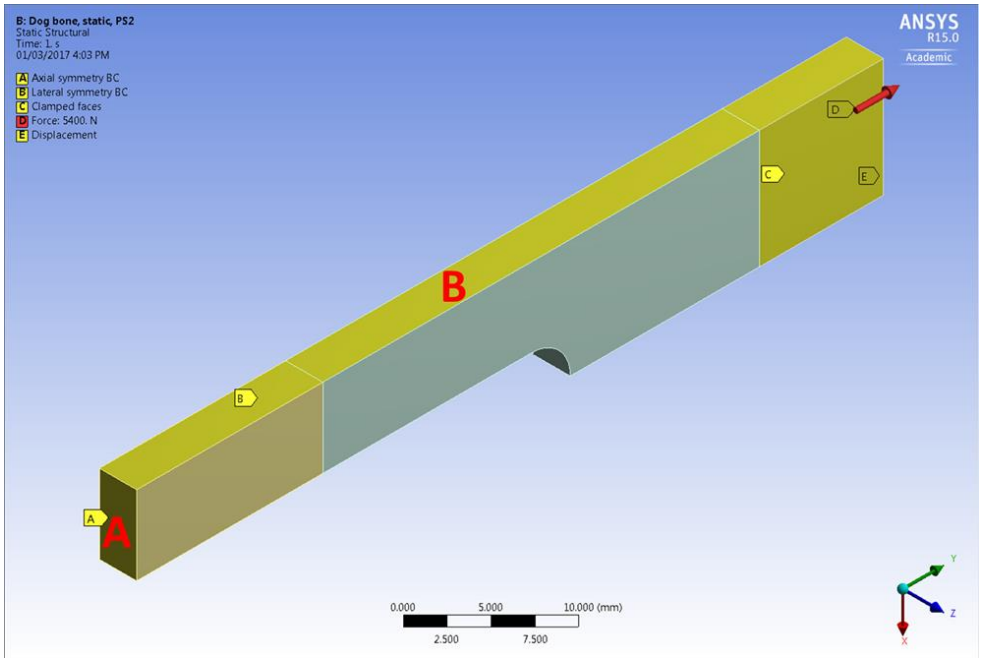

Figure 4.3: Overview of the quartered uniaxial test specimen ("dog bone") showing symmetry conditions 'A' (axial symmetry – {UY =0}) and 'B' (lateral symmetry – {UX=0}), the gauge region (left), fillet region (middle), and clamped loading region (right), and the loading applied to the right face (red arrow).

The results predicted from both the tests and the analytical solution included maximum normal Y-Axis true stress, maximum equivalent plastic strain, and normal Y-Axis elastic strain. Figure 4.4 presents a plot of stress versus strain highlighting the material behaviour exhibited during the two-stage loading simulation. A summary of the results from the simulation and the analytical calculations are provided in Table 4.1.

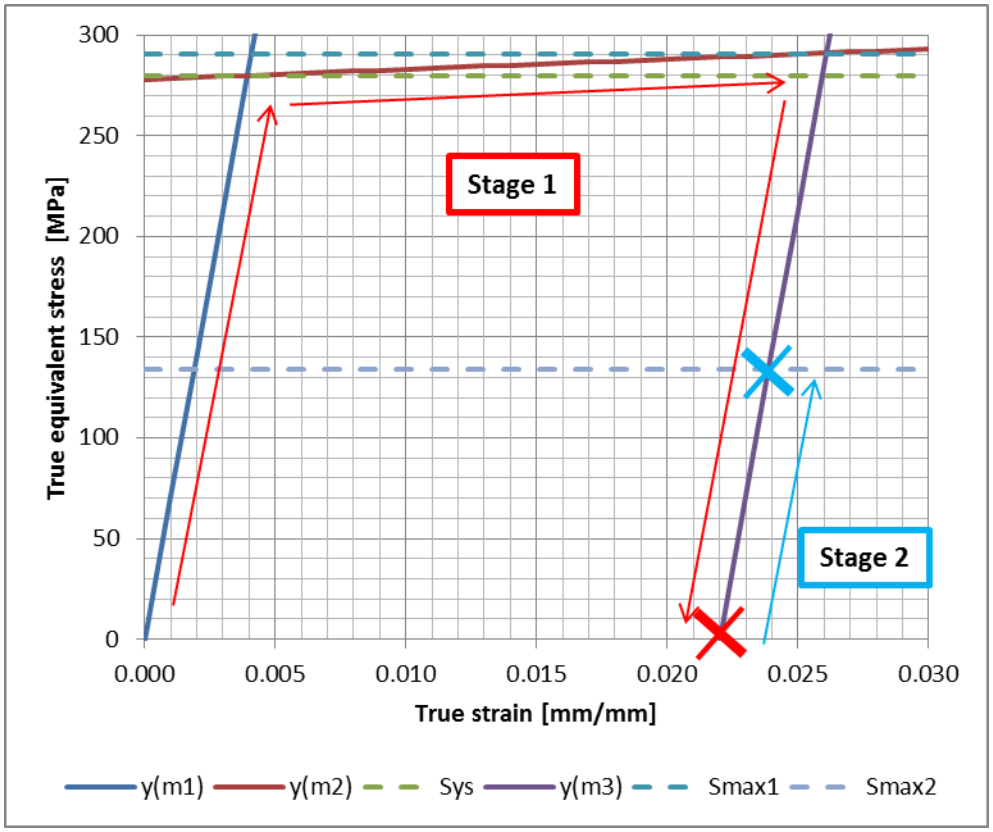

Figure 4.4: Plot of stress versus strain for the uniaxial tensile test featuring the explicit solver.

Table 4.1: Summary of true stress and strain results from the uniaxial tensile test featuring both solvers, and the results from the analytical solution.

			Explicit solver	Implicit solver	Analytical solution
Stage 1 plasticity-inducing load	Normal Y-Axis Elastic Strain	[mm/mm]	0.004	0.004	0.004
	Maximum Equivalent Plastic Strain		0.022	0.022	0.022
	Maximum Normal Y-Axis Stress	[MPa]	289.6	289.8	290.8
Stage 2 incremental load	Normal Y-Axis Elastic Strain	[mm/mm]	0.002	0.002	0.002
	Maximum Equivalent Plastic Strain		0.022	0.022	0.022
	Maximum Normal Y-Axis Stress	[MPa]	133.7	134.1	134.3

For the analytical solution, the true stress at the end of the simulation was calculated from the following equations representing the stress-strain relationship.

$$\sigma = E(\varepsilon - \varepsilon_p) \quad (1)$$

$$\sigma = S(1 + e) \quad (2)$$

$$\varepsilon = \ln(1 + e) \quad (3)$$

σ is the true stress, E is the modulus of elasticity, ε is the total true strain, ε_p is the residual plastic strain from the plasticity-inducing load, S is the engineering stress, and e is the engineering strain. Substituting equations (2) and (3) into (1) yields:

$$S(1 + e) - E\{[\ln(1 + e)] - \varepsilon_p\} = 0 \quad (4)$$

Solving equation (4) yielded a total engineering strain value e of 0.024mm/mm, and a corresponding true stress value of 134.3MPa.

All of the results were within 0.5% of each other which indicated that plasticity was incorporated correctly when determining the stresses for a two-stage loading simulation, and that an explicit solver can be used for modelling post-impact static tensile loading.

Lastly, though 2ms was used for the incremental load in the test featuring the explicit solver, a 1ms duration for the post-impact tensile load in the model of the panel was used as no dynamic effects were seen and the run time was reduced by 17 hours.

5. Determining the effect of dent size on face sheet stresses for post-impact tensile loading

5.1. Introduction

The overall goal of this research was to determine if and how dent size affects face sheet stresses under post-impact tensile loading. This was achieved by using the two-stage loading simulation described in Chapter 4. Using the two-stage model with the impact and panel parameters described in Chapters 3 and 4, two separate series of tests were conducted to determine the influence of dent depth and dent diameter on the stresses in the face sheet. Specific damage states were achieved by altering the parameters of the impact and the panel. Upon consolidating the results from these tests, the specific characteristics of the impact damage affecting the stresses were determined.

5.2. The effects of dent depth on face sheet stress increases

5.2.1. Methods (dent depth study)

The first series of tests examined the effect of dent depth on the face sheet stresses under post-impact tensile loading. Specifically, the aim with these tests was to study the percent increase in the face sheet stresses from the end of the impact stage to the end of the post-impact tensile loading stage for varying dent depths. These tests were run using the two-stage loading simulation with the same loading parameters defined in Section 3.2, namely, an indenter mass and velocity of 0.125kg and 4m/s, respectively.

In order to isolate the effects of dent depth, the thickness of the face sheet was varied in order to produce different dent depths while keeping the dent diameter and core damage shape constant. Clarke found that as the

face sheet thickness increased, the dent depth decreased with virtually no changes to dent diameter or to core damage depth or width [26]. Clarke also showed that core damage depth was constant for a given core density, and that core damage width was the same as the dent diameter. This was verified in the present work through predictions of the dent depth, dent diameter, and core damage depth and width.

Two things must be noted prior to presenting the results from this study. The first deals with the far-field stresses in the face sheet, and the second deals with comparing results. Far-field stresses refer to the stresses produced in an undented face sheet and in a dented face sheet away from the dent.

First, for a prescribed displacement of 0.1mm, a far-field stress of 76MPa was produced for all thicknesses of face sheets because the modulus of elasticity and the strain remained the same. This was confirmed by applying a 0.1mm displacement to a model of the face sheet for varying face sheet thicknesses between 0.508 and 1.524mm, as shown in Table 5.1.

Table 5.1: Face sheet thicknesses, face sheet tensile loads, and maximum equivalent face sheet stresses resulting from a 0.1mm displacement applied to a model of the face sheet only.

Face sheet thickness	Load	Max. eq. stress
[mm]	[N]	[MPa]
0.508	4165	76
0.762	6247	76
1.016	8329	76
1.27	10412	76
1.524	12494	76

Second, in order to determine the percent increases in face sheet stresses and make it such that they were comparable to other models, the stress values post-impact and at the end of the tensile loading stage had to be extracted from a common location. Specifically, the stress predictions were taken at the centre of the dent where the bulk of face sheet yielding occurred.

5.2.2. Results (dent depth study)

The results of interest were the percent increases in stress between post-impact and post-tensile loading for different dent depths. This would indicate how much the stress in a dent could increase during operational loading and whether the depth of the dent has an effect on the percent increase in stress. Five different face sheet thicknesses were considered, producing the dent depths, dent diameters, and core damage depths and widths reported in Table 5.2. Dent depth and core damage depth and width were predicted using the same method as in Subsection 3.3.3. Dent diameter was predicted from the vertical deflection of the face sheet where the edge of the dent corresponded to a 0.01mm deformation threshold. The dent depths varied by 93% while dent diameter, core damage depth, and core damage width varied by 18%, 25%, and 17%, respectively. This confirms that dent depth was varied while keeping dent diameter, and core damage depth and width relatively constant. Furthermore, the average percent difference between core damage width and dent diameter was 3.3%. This is consistent with Clarke's findings where it was found that core damage width matched dent diameter [26].

Table 5.2: Dent depth study parameter (face sheet thickness), resulting dent dimensions (depth and diameter), and resulting core damage dimensions (depth and width).

Face sheet thickness	Dent depth	Dent diameter	Core damage depth	Core damage width
[mm]	[mm]	[mm]	[mm]	[mm]
0.508	1.04	28.8	5.7	29.6
0.762	0.78	30.3	6.1	31.7
1.016	0.60	31.5	6.6	32.3
1.27	0.47	33.0	6.9	34.9
1.524	0.38	34.6	7.3	35.0

Recalling that the applied loading induced a tensile stress of 76MPa in the face sheet,

Table 5.3 presents the equivalent face sheet stresses at coupon mid-span in the W-direction along the bottom surface where the highest stresses formed. Also included in Table 5.3 are the corresponding stress increases at three separate locations in the yielded portion of the impacted face sheet

which enabled comparisons among all dent depths considered. The stress locations are shown in Figure 5.1. The percent increases are illustrated graphically in Figure 5.2.

Table 5.3: Equivalent stresses and corresponding percent increases at three separate locations within the yielded dent regions for all dent depths considered. Location 2 corresponds to the centre of the dent.

Dent depth [mm]	Equivalent stress [MPa]			
	-	Location 1	Location 2	Location 3
1.04	post-impact	304.30	293.33	318.70
	post-tensile loading	355.95	357.39	380.49
	magnitude of stress increase	51.65	64.06	61.79
	percent increase	*17.0%*	*21.8%*	*19.4%*
0.78	post-impact	406.11	394.38	400.63
	post-tensile loading	436.94	447.72	429.50
	magnitude of stress increase	30.83	53.34	28.87
	percent increase	*7.6%*	*13.5%*	*7.2%*
0.60	post-impact	335.80	519.54	371.13
	post-tensile loading	338.71	531.08	373.85
	magnitude of stress increase	2.91	11.54	2.72
	percent increase	*0.9%*	*2.2%*	*0.7%*
0.47	post-impact	292.23	528.52	285.10
	post-tensile loading	276.67	520.26	272.02
	magnitude of stress increase	-15.56	-8.26	-13.08
	percent increase	*-5.3%*	*-1.6%*	*-4.6%*
0.38	post-impact	253.51	523.06	248.89
	post-tensile loading	254.18	500.56	256.72
	magnitude of stress increase	0.67	-22.50	7.83
	percent increase	*0.3%*	*-4.3%*	*3.1%*

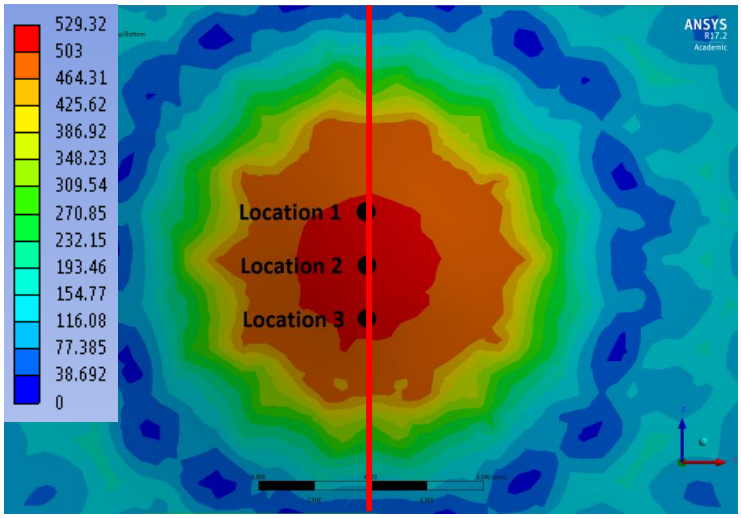

Figure 5.1: Zoomed-in view of bottom surface of impacted face sheet, equivalent stresses [MPa] peak-impact, 1.04mm dent depth, locations of stress predictions. Location 2 corresponds to the centre of the dent. The red line indicates the W-direction path at coupon mid-span. The red contour band indicates yielding.

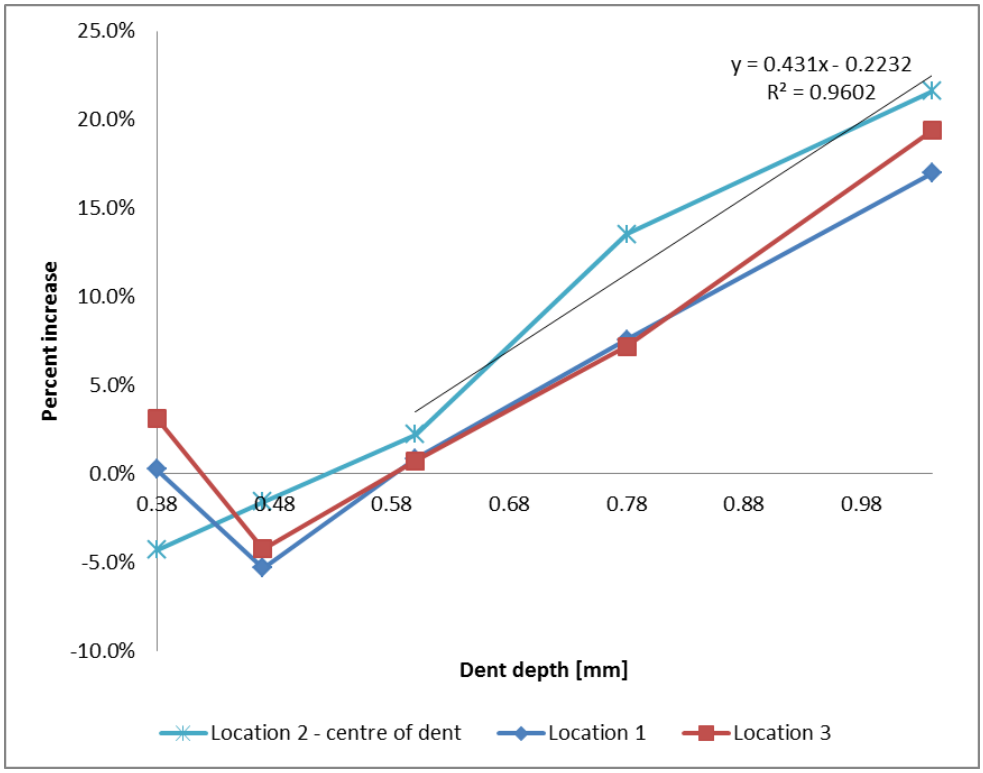

Figure 5.2: Plot of percent increase versus dent depth at all three dent-centre locations. A trend line is shown for the 0.60mm-1.04mm dent depths.

For the dents shallower than 0.60mm, the percent increases in stress were less than 5.3% indicating that none of the applied tensile load passed through the dent. From a dent depth of 0.60mm to a dent depth of 1.04mm, the percent increase in stress at the centre of the dent increased linearly up to 21.8% indicating that more of the load passed through the face sheet dent.

In order to validate the results presented in Table 5.3 and highlight the effect of dent depth on changes to the load path, the magnitude of the equivalent stress at the centre of the dent recorded at the end of the two-stage simulation was compared to the sum of the post-impact stress and the applied 76MPa tensile stress. If the entire load passed through the dent, then the stress predictions from the simulation and the stresses calculated from adding the post-impact stresses and 76MPa stress from tensile loading

would have been equal. The magnitudes of the predicted increases are highlighted in Table 5.3, and a comparison to the calculated stresses is illustrated in Figure 5.3 for the models with the deepest dent (1.04mm) and shallowest dent (0.38mm).

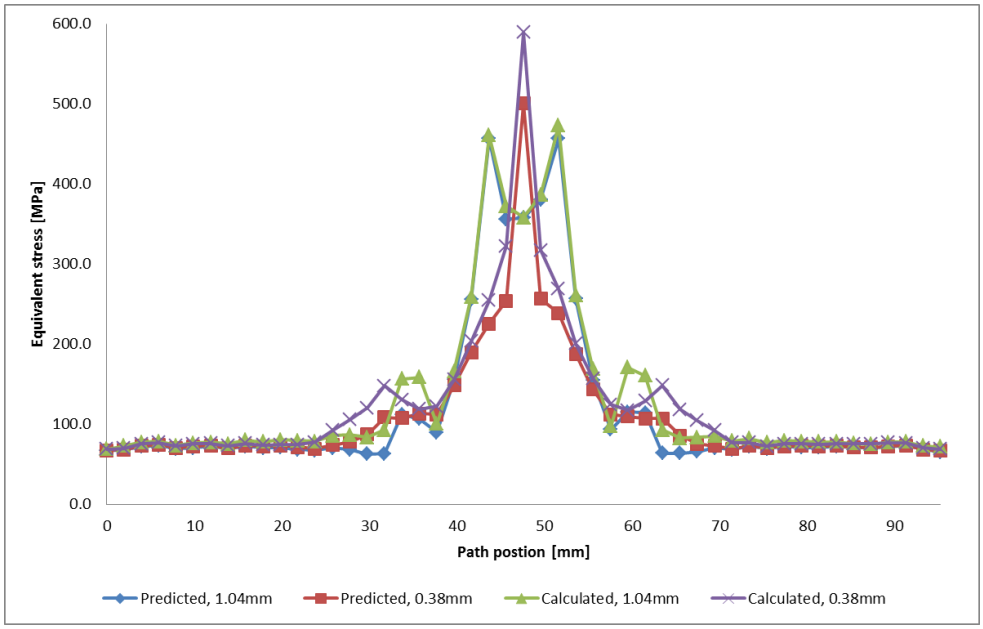

Figure 5.3: Plot of predicted and calculated equivalent stresses versus mid-span W-direction path position for the models with the 1.04mm and 0.38mm dent depths.

In the region away from the dent, the far-field stresses from the two-stage simulation were the same as those predicted by summing the post-impact and the applied stress of 76MPa. This indicates that the applied load passed through the face sheet in the region away from the dent. The stresses were also the same at the centre of the 1.04mm dent which means the load passed through the face sheet dent. For the 0.38mm dent depth, the stresses at the centre of the dent recorded from the two-stage simulation were 24% lower than the sum of the post-impact stresses and 76MPa tensile stress, meaning a significant portion of the tensile load did not pass through the face sheet dent. The predicted stresses were up to 40% lower than the calculated stresses around the circumferences of both the 1.04mm and 0.38mm dents. These observations indicate that the load path through the panel changes when a dent is present.

Illustrations of the equivalent face sheet stresses post-impact and post-tensile loading for the models with the dent depths of 1.04mm and 0.38mm are provided in Figure 5.4. These figures show a view of the bottom surface of the top face sheet where the highest stresses formed. The scale is the same for all stress distributions shown, with the red contour band denoting yielding.

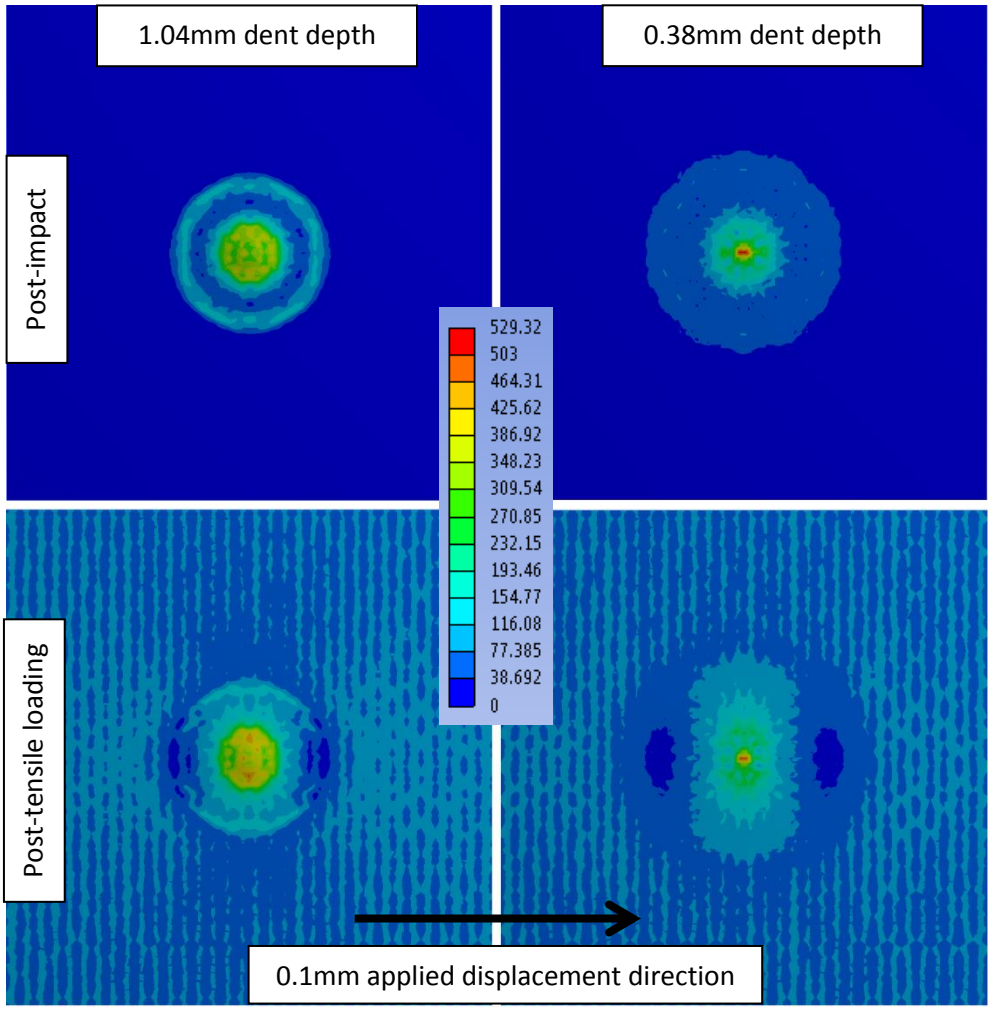

Figure 5.4: Dent depth study, equivalent stresses [MPa], bottom surface of impacted face sheet.

Yielding occurred in a small region at the centres of the dents and the highest post-impact stresses were contained within the dents. The dent was more spread out for the 0.38mm because the face sheet was thicker which made the dent less isolated. In the region away from the dent, there were no stresses in the face sheet post-impact. The tensile loading added a far-field stress of 76MPa to the face sheet, which is indicated by the lighter blue lines where the cell walls attach to the face sheet. The darker blue lines coincide with the cell walls of doubled thickness in the L-direction.

Upon inspection of the core, one finds that the width of the void in the core made by eroded elements increased for increasing dent depth despite the same overall size of core plasticity for all dent depths. For larger face sheet deflections yielding deeper dents, cell wall buckling was more prominent and resulted in increased element deformation and eventually element failure. When the void was larger, the core stresses were higher near the face sheet. When the void was smaller, the stresses near the dent were more evenly distributed within the core. This may indicate that the load passed through the face sheet when the void was present. When the core was intact, the load was drawn away from the face sheet and into the core. A comparison of the core voids made by the eroded core elements and core stresses for the 1.04mm and 0.38mm dent depths is provided in Figure 5.5.

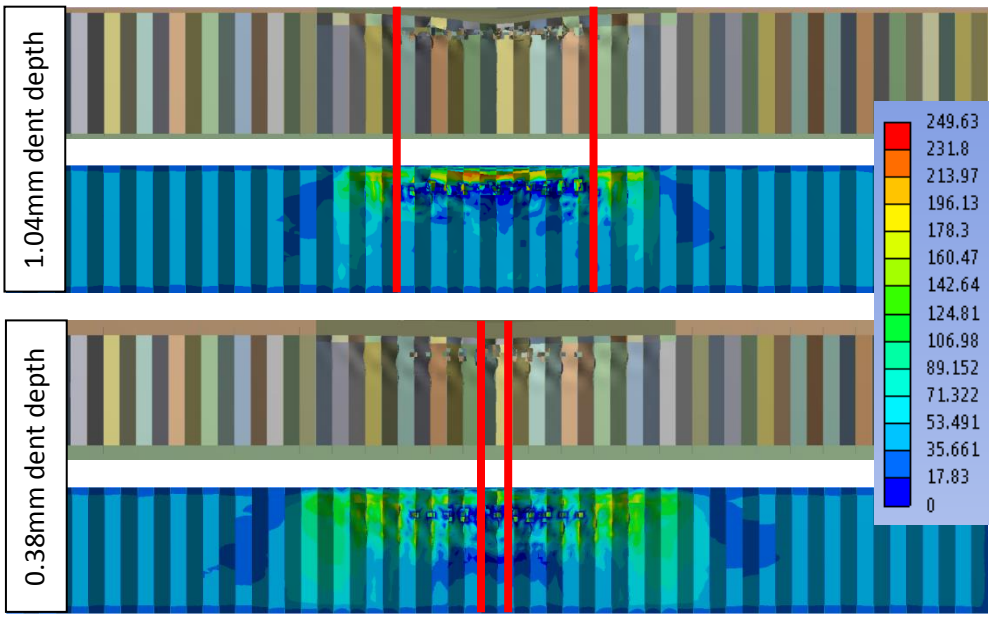

Figure 5.5: Dent depth study, side views of core damage and equivalent stresses [MPa] at coupon mid-span using a W-direction slice. The red lines indicate the extremities of the voids made by the eroded core elements.

In summary, there appears to be a difference in how the load was passed through and around the dent for different dent depths. The percent increase in equivalent stress at the centre of the dent was higher when the dent was deeper.

5.3. The effects of dent diameter on face sheet stress increases

5.3.1. Methods (dent diameter study)

In the second series of tests, dent diameter was varied while keeping dent depth and core damage depth constant. Core damage width is equal to dent diameter [26] for panels with metallic face sheets and core, so keeping core damage width constant while varying the dent width was not possible. Constant dent depth and varying dent diameter was achieved by varying indenter radius and impact velocity. Larger indenter radii result in comparatively wider and shallower dents, whereas larger impact velocities result in both deeper and wider dents with similar increases to core damage width [26]. Therefore, indenter radius was varied between 2.54mm and 12.70mm, and indenter velocity was varied between 3.00m/s and 4.00m/s to produce five different dent diameters. All other coupon and indenter features were kept constant, including indenter mass through adjusting the indenter material density.

5.3.2. Results (dent diameter study)

The indenter radii, velocities, dent depths, dent diameters, and core damage depths and widths for the dent diameter study are given in Table 5.4. Dent diameter varied by 32%, while dent depth, core damage depth, and core damage width varied by 9%, 6%, and 28%, respectively. This shows that dent depth and core damage depth varied minimally with respect to dent diameter, though core damage width varied significantly due to the relationship between dent diameter and core damage width. Specifically, the average percent difference between core damage width and dent diameter was 5.5%. This variance in core damage width is assessed in the discussion (Section 5.4).

Table 5.4: Dent diameter study parameters (indenter radius and velocity), resulting dent dimensions (depth and diameter), and resulting core damage dimensions (depth and width).

Indenter radius	Indenter velocity	Dent depth	Dent diameter	Core damage depth	Core damage width
[mm]	[m/s]	[mm]	[mm]	[mm]	[mm]
12.70	4.00	1.04	28.8	5.6	29.6
10.16	3.75	1.00	27.2	5.5	28.6
7.62	3.50	0.98	25.3	5.5	26.6
5.08	3.25	0.97	23.3	5.3	25.4
2.54	3.00	0.95	20.9	5.3	22.2

Table 5.5 presents the equivalent face sheet stresses and corresponding stress increases which are illustrated graphically in Figure 5.2. The same stress locations as in Figure 5.1 were used.

Table 5.5: Equivalent stresses and corresponding percent increases at three separate locations within the yielded dent regions for all dent diameters considered. Location 2 corresponds to the centre of the dent.

Dent diameter	Equivalent stress [MPa]			
[mm]	-	Location 1	Location 2	Location 3
20.9	post-impact	467.35	566.18	470.09
	post-tensile loading	491.03	586.62	492.13
	magnitude of stress increase	23.68	20.44	22.04
	percent increase	*5.1%*	*3.6%*	*4.7%*
23.3	post-impact	412.24	390.94	402.08
	post-tensile loading	450.58	459.99	445.76
	magnitude of stress increase	38.34	69.05	43.68
	percent increase	*9.3%*	*17.7%*	*10.9%*
25.3	post-impact	353.26	330.52	351.26
	post-tensile loading	404.58	393.67	402.34
	magnitude of stress increase	51.32	63.15	51.08
	percent increase	*14.5%*	*19.1%*	*14.5%*
27.2	post-impact	342.65	286.80	335.52
	post-tensile loading	390.03	340.22	384.23
	magnitude of stress increase	47.38	53.42	48.71
	percent increase	*13.8%*	*18.6%*	*14.5%*
28.8	post-impact	318.70	293.93	304.30
	post-tensile loading	380.49	357.39	355.95
	magnitude of stress increase	61.79	63.46	51.65
	percent increase	*19.4%*	*21.8%*	*17.0%*

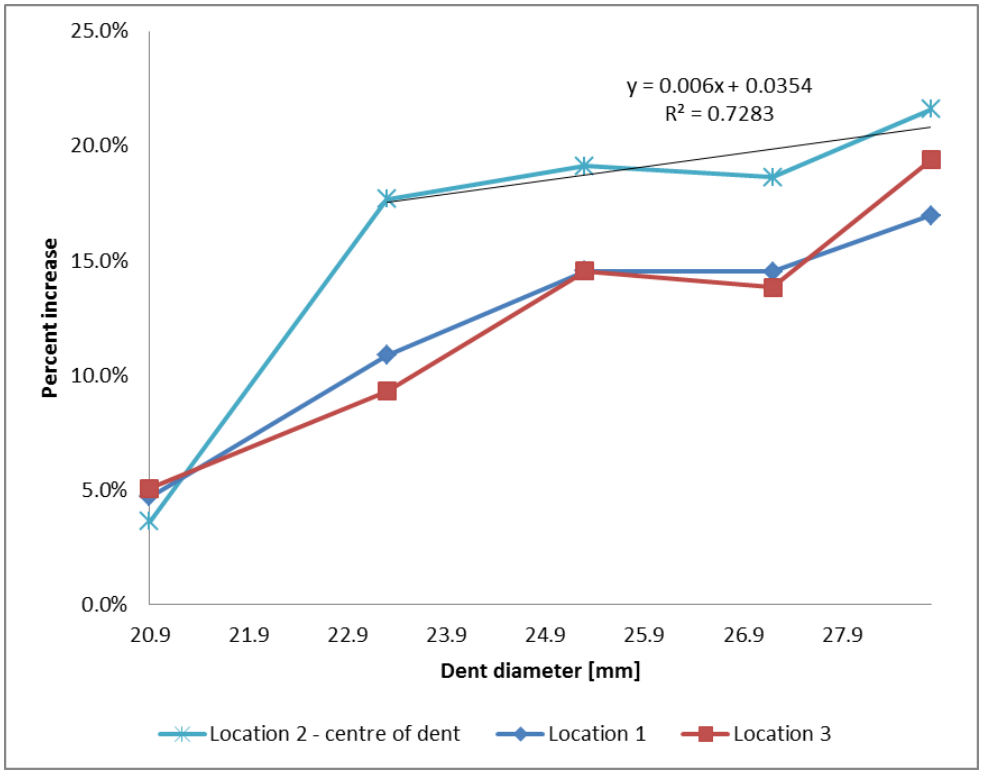

Figure 5.6: Plot of percent increase versus dent diameter at all three dent-centre locations. A trend line is shown for the 23.3mm-28.8mm dent diameters.

For the model with the smallest dent diameter (20.9mm), the percent increases in stress were less than 5.1% which indicates that the tensile load did not pass through the face sheet. From a 23.3mm dent diameter to a 28.8mm dent diameter, the percent increase in stress at the dent-centres increased linearly up to 21.8% indicating that a larger portion of the load passed through the dents.

A graphical comparison of the stress predictions at the end of the two-stage simulations and the stresses calculated from adding the impact stresses and 76MPa tensile stress is shown in Figure 5.7.

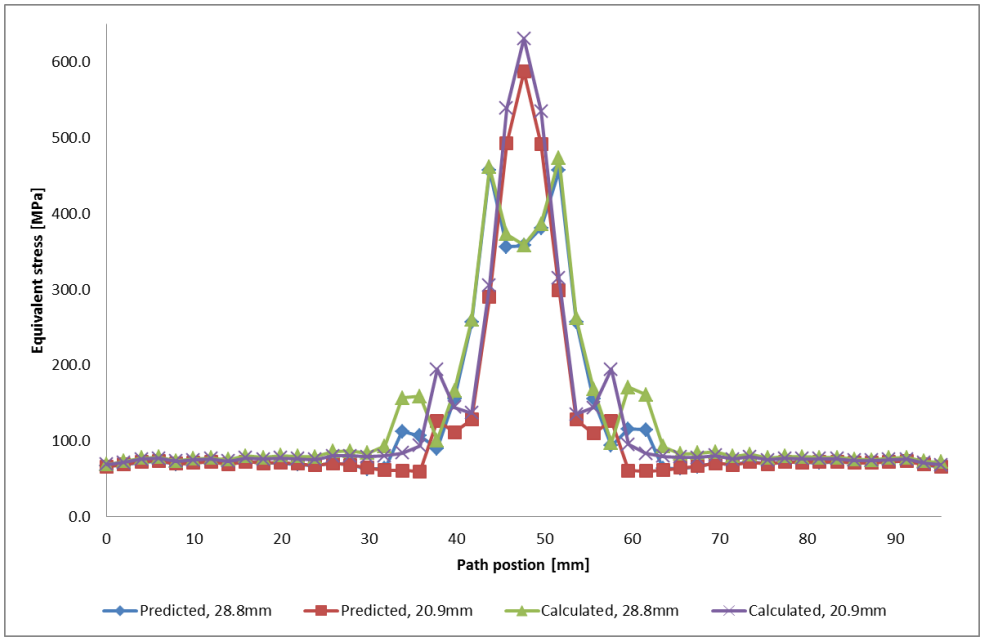

Figure 5.7: Plot of predicted and calculated equivalent stresses versus mid-span W-direction path position for the models with the 28.8mm and 20.9mm dent diameters.

The far-field stresses from the two-stage simulations were the same as those predicted by summing the post-impact stresses and 76MPa tensile stress, indicating that the applied load passed through the face sheet away from the dents. At the dent-centre for the 28.8mm dent, the stresses were also the same which means that the entire tensile load passed through the face sheet dent. As for the model with the 20.9mm dent diameter, the stresses recorded at the end of the two-stage simulation at the centre of the dent were 8% lower than the calculated stresses. This indicates that less of the load passed through this dent, though this is not as severe as the 24% difference recorded for the shallowest dent from the dent depth study. Similar to the observations made in the dent depth study, the predicted stresses were up to 44% lower than the calculated stresses around the circumferences of the dents. As such, changes to the load path were present with varying dent diameter, though not as severe at dent-centres compared to varying the dent depth. Illustrations of the equivalent face sheet stresses are provided in Figure 5.8.

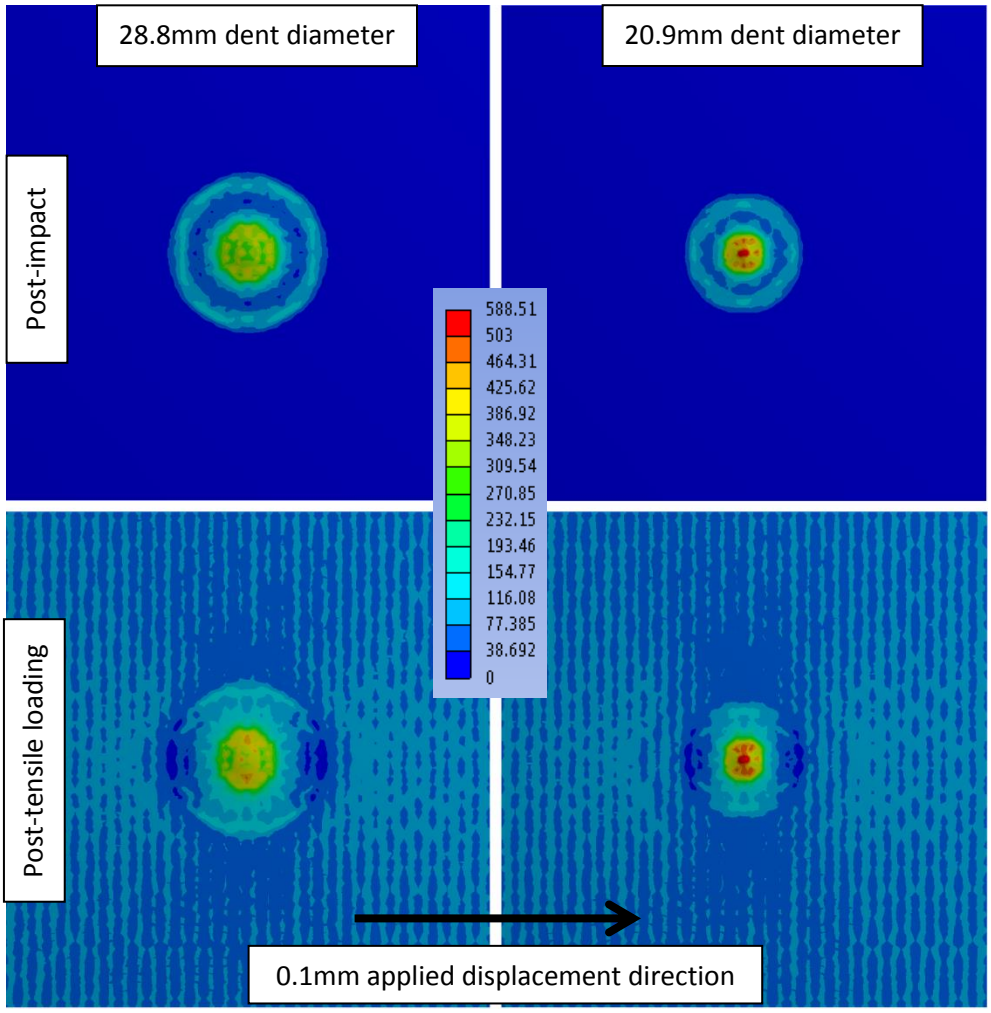

Figure 5.8: Dent diameter study, equivalent stresses [MPa], bottom surface of impacted face sheet.

A small region of yielding occurred at dent-centres with the highest post-impact stresses contained within the dents. Away from the dents, the post-impact face sheet stress was zero. The 76MPa far-field stress state developed due to the tensile loading, indicated by the light and dark blue lines.

Inspection of the core in Figure 5.9 reveals that the width of the void in the core made by the eroded elements increased slightly with increasing dent

diameter and core damage width. For both void sizes, core stresses were higher near the face sheet. As with the dent depth study, this may indicate that the presence of a core void caused the load to pass through the dent.

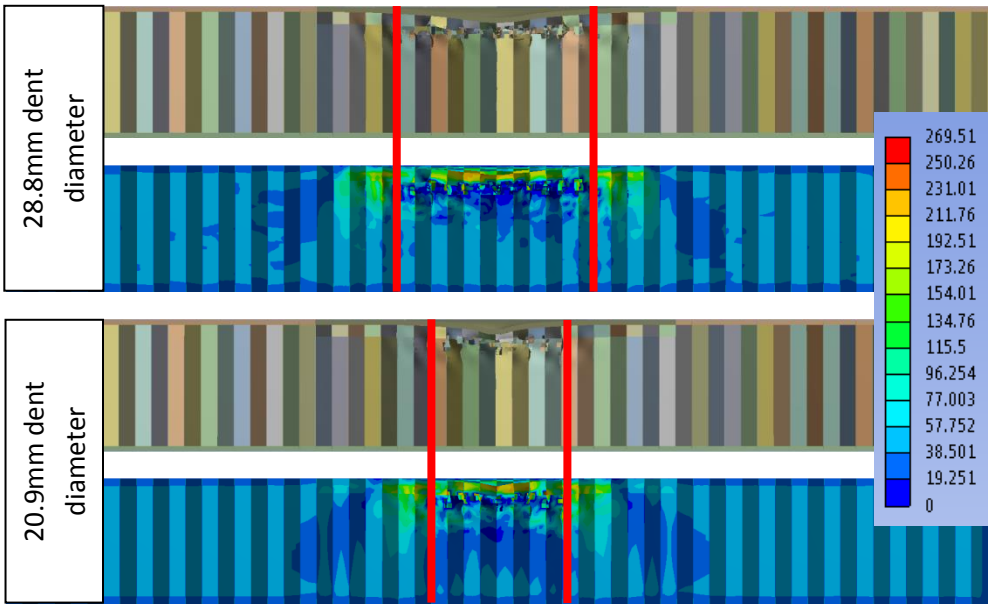

Figure 5.9: Dent diameter study, side views of core damage and equivalent stresses [MPa] at coupon mid-span using a W-direction slice. The red lines indicate the extremities of the voids made by the eroded core elements.

In summary, the load path changed minimally with varying dent diameter as all dent widths produced increases in equivalent stress between 20-70MPa of the expected 76MPa. In all cases, at least part of the tensile load was passing through the face sheet dent.

5.4. Discussion

The results from the dent depth and the dent width study showed that deeper and wider dents produce larger increases in face sheet stress when a tensile load is applied to a panel that contains impact damage. There was a 21.8% increase in stresses for both the model with the 1.04mm dent depth and the model with the 28.8mm dent diameter. This percent increase coincided with the expected 76MPa increase in stress due to the applied tensile load passing through the face sheet. For all dent widths and dent depths above 0.6mm, there was an indication that part of the load was passing through the face sheet. Upon inspection of the core, it was revealed that voids in the core formed by eroded core elements were present in these cases. However, when dent depths were 0.6mm or less, the increase in stress was below 5.3% indicating that the tensile load was not passing through the face sheet dent. In these cases, there was no widespread element erosion.

In order to determine the specific cause for these changes to the load path in the vicinity of the dent, two damage features were considered. The first considers the stress concentration due to the deformed shape of the face sheet in isolation without the presence of face sheet plasticity or core damage. The second considers the presence of core failure in the form of a void beneath the dent. The same 0.1mm displacement resulting in a 76MPa increase in far-field tensile stress was applied. Maximum equivalent stresses at the mid-surface of the face sheet elements were recorded since the face sheets were pre-dented with no residual stresses and were not subjected to bending stresses. Larger dent depths than in Section 5.2 were selected to amplify the effect of dent depth on post-tensile loading stresses. The dent depths and dent diameters that were evaluated are provided in Table 5.6. The maximum difference between the dent depths and dent diameters was 52% and 34%, respectively.

Table 5.6: Dent profile data (depth and diameter) used for studying the effect of dent geometry and core damage on post-tensile loading stresses.

	Dent depth	*Dent diameter*
	[mm]	
Dent #1	1.44	27.27
Dent #2	1.95	
Dent #3	2.46	
Dent #4	1.04	27.37
Dent #5		23.37
Dent #6		19.48

5.4.1. Geometric stress concentration

The effect of the geometric stress concentration in the face sheet was isolated using two variants of the model described in Chapter 4. The first variant comprised a panel with an indented face sheet and a honeycomb core but no associated damage such as face sheet plasticity, residual stresses, residual strains or core damage. The second variant contained an indented face sheet with no plasticity, but with no core altogether. Illustrations of the indented honeycomb panel and face sheet with no associated damage are provided in Figure 5.10 and Figure 5.11.

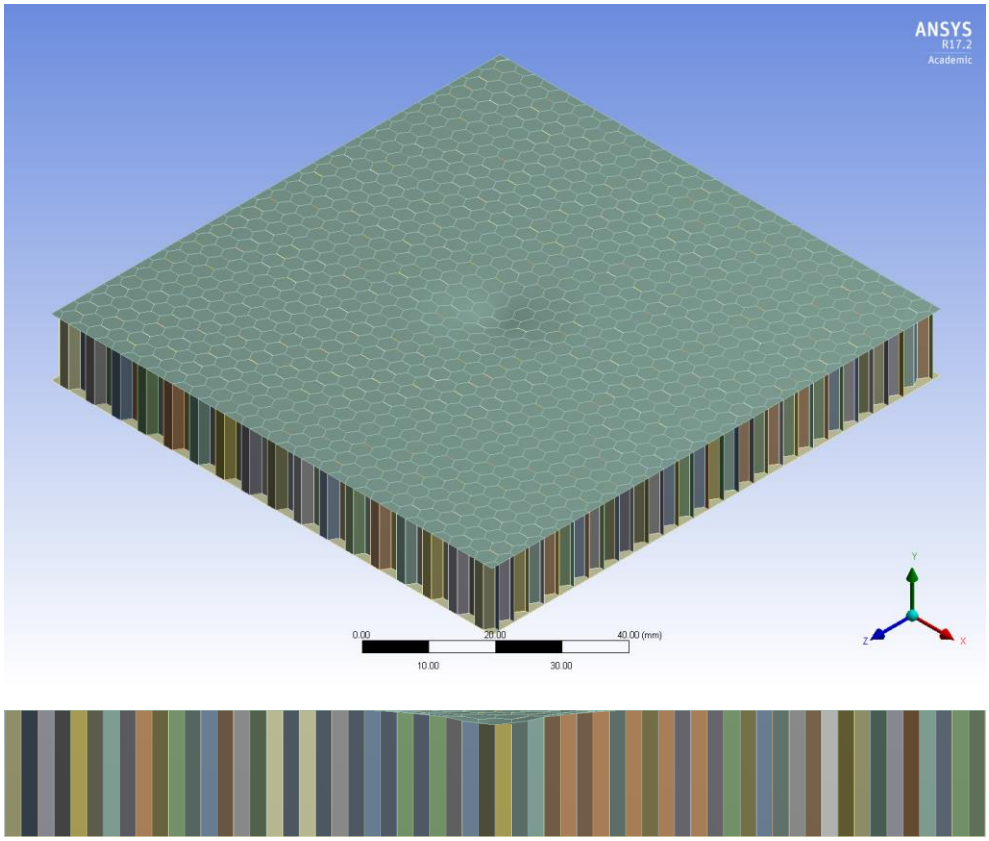

Figure 5.10: Isometric view (top) and side view at coupon mid-span using a W-direction slide (bottom) for an indented honeycomb panel with no associated damage in the face sheet or core.

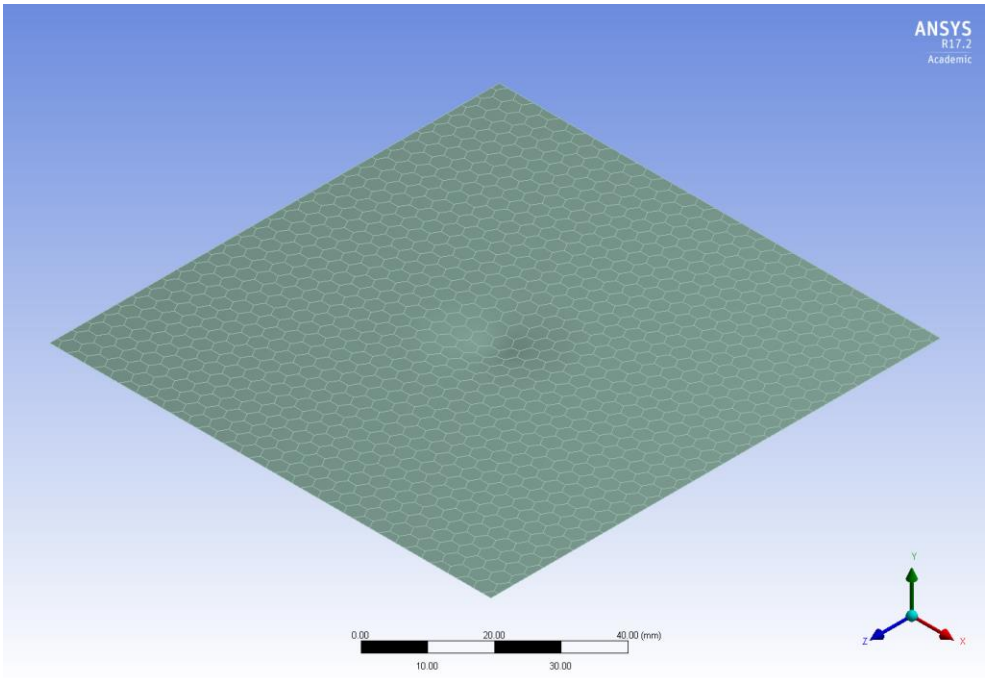

Figure 5.11: Isometric view of an indented face sheet with no damage.

An example of the stress distributions in both an indented panel and indented face sheet subjected to the same tensile load are illustrated in Figure 5.12. Stress concentrations formed to the sides of the dent in the direction perpendicular to the loading, similar to a plate with a hole loaded in the same fashion. The lowest stresses were found at the centre of the dent. For both the panel and face sheet models, the far-field stress state was 76MPa. The model of the face sheet only showed a larger range of stresses in the dent than the model that included the panel.

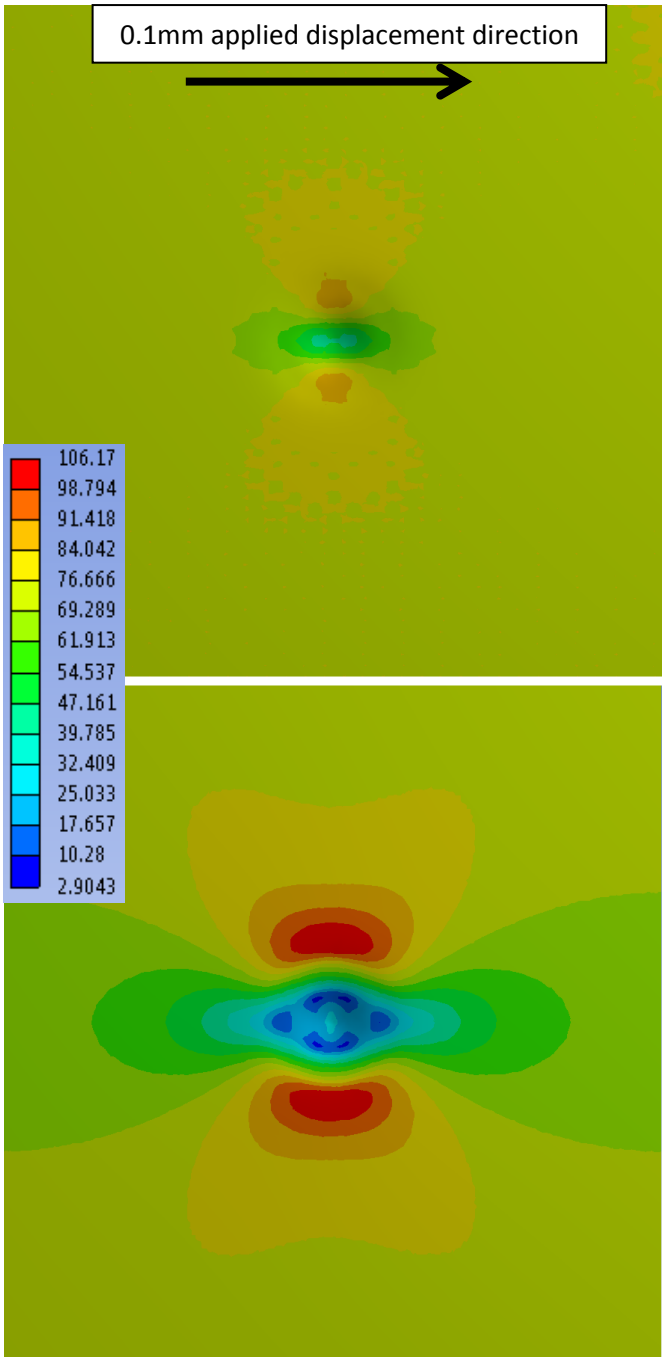

Figure 5.12: Equivalent face sheet stresses [MPa] post-tensile loading for a 2.46mm dent depth – indented panel (top), indented face sheet (bottom).

Comparing the maximum stresses due to tensile loading for different dent depths and diameters shows whether the depth or the diameter of the dent creates different stress concentrations. Table 5.7 shows that varying dent depth has no effect on the maximum stresses. Specifically, an increase of 70.8% in the dent depth resulted in less than a 7.3% increase in stress for the model of the panel. Table 5.8 shows that varying dent diameter has a small effect on the maximum stresses. Namely, a decrease in the dent diameter of 28.8% resulted in an increase of 6.3% for the model of the panel. Altogether, this shows that the geometry of the dent did not have a big effect on the magnitude of the stress concentration. It was not the dent geometry that governed the load path through the dent region. When the maximum stress of 88MPa is compared to the far-field stress of 76MPa, the stress concentration factor is determined to be 1.16. Comparing the panel models with the face sheet models shows that the panel can take up to 29.4% of the load away from the face sheet. This is significant because it shows that if the core is intact underneath a dent, it can draw some of the load away from the dent and into the core.

Table 5.7: Absolute maximum equivalent stresses for varying dent depth, indented honeycomb panel and face sheet with no associated damage.

		Dent depth [mm]			Percent increase
		1.44	**1.95**	**2.46**	70.8%
Equivalent stress [MPa]	**Indented panel, no associating damage**	82	86	88	7.3%
	Indented face sheet, no associating damage	104	105	106	1.9%
	Percent increase	26.8%	22.1%	20.5%	

Table 5.8: Absolute maximum equivalent stresses for varying dent diameter, indented honeycomb panel and face sheet with no associated damage.

		Dent diameter [mm]			Percent increase
		27.37	**23.37**	**19.48**	-28.8%
Equivalent stress [MPa]	**Indented panel, no associating damage**	80	83	85	6.3%
	Indented face sheet, no associating damage	99	102	110	11.1%
	Percent increase	23.8%	22.9%	29.4%	

5.4.2. Core void beneath dent

The effect of the presence of core separation in the form of element erosion was isolated by comparing models with and without a void beneath the dent. This cylindrical void could possibly be used to represent not only core cracking, but weakening of the core through such phenomena as core plasticity, cell wall buckling, or core crushing. The dimensions of this void are shown in Figure 5.13 and are representative of the size of the region of eroded core elements in the models noted in Sections 5.2 and 5.3. The impact phase was omitted, meaning the indented panels had no associated damage such as plasticity, residual stresses, or residual strains. The same six dent profiles presented in Table 5.6 were used, along with the same 0.1mm displacement which put the panel into tension and generated a 76MPa tensile stress. The size of the cylindrical void did not change with varying dent depth or diameter, and the width of the void did not coincide with dent diameter.

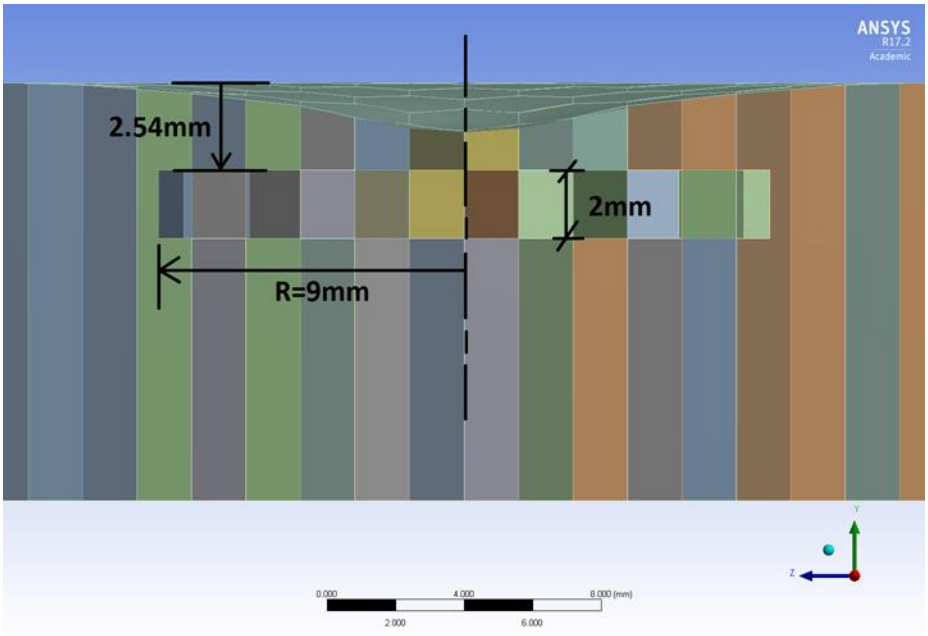

Figure 5.13: Zoomed-in side view of a model with core damage represented by a cylindrical void, and the corresponding dimensions using a mid-span W-direction slice.

Summaries of the maximum equivalent stresses for varying dent depth and diameter for the models of the indented panels with and without representative core damage are given in Table 5.9 and Table 5.10, respectively.

Table 5.9: Absolute maximum equivalent stresses for varying dent depth, indented honeycomb panels with and without core damage.

		Dent depth [mm]			Percent difference
		1.44	**1.95**	**2.46**	52.31%
Equivalent stress [MPa]	**Indented panel, without core damage**	82	86	88	7.06%
	Indented panel, with core damage	98	100	104	6.34%
	Percent increase	18.93%	16.36%	18.07%	

Table 5.10: Absolute maximum equivalent stresses for varying dent diameter, indented honeycomb panels with and without core damage.

		Dent diameter [mm]			Percent difference
		27.37	**23.37**	**19.48**	33.68%
Equivalent stress [MPa]	**Indented panel, without core damage**	80	83	85	5.60%
	Indented panel, with core damage	95	98	101	6.48%
	Percent increase	18.29%	17.87%	19.35%	

The maximum stress level in the model of the indented panel with the void in the core was on average 18% greater than the maximum stress level in the equivalent model without a void in the core, regardless of dent depth or diameter. This indicates that core damage causes a larger portion of the load to pass through the dented region of the face sheet. This phenomenon is illustrated upon inspection of core stresses in Figure 5.14. When the void is present, the highest stresses occur between the face sheet and the void indicating that much of the load is passing through the face sheet. When there is no void present, the highest stresses are in the core and extend deeper into the core than when a void is present.

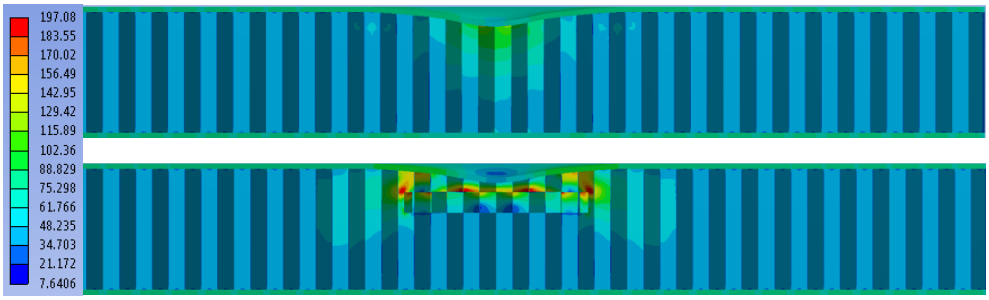

Figure 5.14: Comparison of equivalent core stresses [MPa] between a model of an indented panel without core damage (top) and an equivalent panel with core damage (bottom) using the mid-span W-direction slice. The 0.1mm displacement direction is out of the page.

Table 5.11 and Table 5.12 show that when a void is present, the stresses in the face sheet are within 8.21% of the stresses in a model of the face sheet only. This shows that when a void is present in the core, the tensile load passes through the face sheet dent, and behaves as if the face sheet is in isolation with no support from the core. In the absence of core damage, the core restricts the dent from straightening, thus engaging the core and drawing the load into the core.

Table 5.11: Absolute maximum equivalent stresses for varying dent depth, indented face sheets with no associated damage and indented panels with core damage.

		Dent depth [mm]		
		1.44	**1.95**	**2.46**
Equivalent stress [MPa]	**Indented face sheet, no associating damage**	104	105	106
	Indented panel, with core damage	98	100	104
	Percent difference	6.43%	4.81%	2.00%

Table 5.12: Absolute maximum equivalent stresses for varying dent diameter, indented face sheets with no associated damage and indented panels with core damage.

		Dent diameter [mm]		
		27.37	**23.37**	**19.48**
Equivalent stress [MPa]	**Indented face sheet, no associating damage**	99	102	110
	Indented panel, with core damage	95	98	101
	Percent difference	4.16%	4.44%	8.21%

The results presented in this section showed that the 21.8% increases in stresses for both the deepest dent considered in Section 5.2 (1.0mm dent depth) and the widest dent considered in Section 5.3 (28.8mm dent diameter) were caused primarily by the associated core damage in the form of large voids made by the eroded core elements in those models and not a result of the dents themselves. Minimal effect was provided by the diameters of the corresponding dents, and dent depth had no effect in this capacity. This was confirmed through comparisons of indented panel models with and without representative core damage and no associated impact damage for varying dent depth and diameter where it was found that the maximum stress level increased by 18% on average.

The core damage represented in these models corresponds to cases where core cracking is present. Though core cracking was not observed following destructive sectioning of a similar panel from the Griffon, core cracking has been observed in some specific cases involving panels with thicker face sheets. Core cracking may also develop and grow during fatigue loading, following an impact event.

6. Summary and conclusions

The goals of this thesis were to develop a method using FE modelling techniques for predicting face sheet stresses in an aluminum honeycomb panel with low-velocity impact damage loaded in tension, and to identify the effects of dent depth and dent diameter on the relative stress increases in the impacted face sheet.

It was found that neither dent depth nor dent diameter themselves determined the percent increase in stress due to tensile loading post-impact. Instead, the increased stresses resulted from the associated core damage in the form of a void representing material failure. When said void was present, the tensile load passed through the face sheet and the stresses here increased by a magnitude equal to the applied tensile stress. When the core beneath the dent was intact, the tensile load passed through the core and there were no increases in face sheet stresses. The geometry of the dent had no effect on the face sheet stresses for a given void size.

It has been shown that core damage must be represented in FE simulations used to predict stresses in the face sheets of honeycomb panels subject to tensile loading following impact. The change in the load carrying capacity of the core must be captured in order for residual strength to be accurately predicted.

6.1. Future work

Given the ultimate goal of predicting losses in residual strength using simplified core representation, the present work would benefit from the following in relation to the percent increases in stress:

- A validation of the current results through experimental testing. The current FE model setup should be replicated as closely as possible in order to confirm the observations concluded herein;

- A study on the effect of the size of the void made by the eroded core elements. The location and thickness of the void should be maintained and only the width should be varied in order to study how the load path changes and whether or not the width must be known when representing core damage in the simplified model;

- An investigation into alternate methods of representing core damage. Instead of a cylindrical void representing core failure, core damage in the form of plasticity and cell wall buckling can be represented as a cylinder of core material with a comparatively reduced stiffness;

- A study on the effect of different core material failure criteria. The maximum equivalent plastic strain failure criteria should be varied in order to determine the threshold where element erosion and artificial core material failure ceases and begins to liken to that observed from real-life panels; and

- Consider different types of loading, such as bending. A method for simulating pure bending should be employed in order to avoid complicated setups such as four-point bending which make it more difficult to replicate local buckling of the face sheet due to premature failure at the load introduction points.

References

[1] J. Barrette, "Royal Canadian Air Force Image Gallery"; [Online]. Available: http://rcaf-arc-images.forces.gc.ca/gallery/caf/detail/?filename=IS04-2016-0003-019&assetId=56394

[2] T. Reyno. Optical 3D Scanning, Eddy Current Testing, and Destructive Methods for Assessing Surface and Core Damage in Honeycomb Sandwich Aircraft Panels. Master's thesis, The Royal Military College of Canada, September 2017.

[3] D. Zhang, Q. Fei, and P. Zhang, "Drop-weight impact behavior of honeycomb sandwich panels under a spherical impactor," Composite Structures, vol. 168, pp. 633–645, 2017.

[4] Personal communications with members of the Canadian Armed Forces. 2016-2017.

[5] S. Abrate, "Impact engineering of composite structures", International Centre for Mechanical Sciences: Courses and Lectures, vol. 526, Springer Wien New York, 2011.

[6] D. Hodges and G. Pierce, "Introduction to Structural Dynamics and Aeroelasticity", Cambridge Aerospace Series, Cambridge University Press, 2nd Edition, 2011.

[7] M. Gower, R. Shaw, and G. Sims, "Evaluation of the repeatability under static loading of a compression-after-impact test method proposed for ISO standardisation", National Physical Laboratory, Middlesex, UK, 2005.

[8] D. McGowan and D. Ambur, "Compression response of a sandwich fuselage keel panel with and without damage", Technical report, NASA Langley Research Center, 1997.

[9] D. Zhang, D. Jiang, Q. Fei, and S. Wu, "Experimental and numerical investigation on indentation and energy absorption of a honeycomb sandwich panel under low-velocity impact", Finite Elements in Analysis and Design, vol. 117, pp. 21 – 30, 2016.

[10] C. Foo, G. Chai, and L. Seah, "Quasi-Static and Low-Velocity Impact Failure of Aluminium Honeycomb Sandwich Panels," Proc. IMechE Part L: J. Materials: Design and Applications, vol. 220, no. 2, pp. 53–66, 2006.

[11] C. Foo, G. Chai, and L. Seah, "A model to predict low-velocity impact response and damage in sandwich composites," Composites Science Technology, vol. 68, no. 6, pp. 1348–1356, 2008.

[12] C. Foo, L. Seah, and G. Chai, "Low-velocity impact failure of aluminium honeycomb sandwich panels," Composite Structures, vol. 85, no. 1, pp. 20–28, 2008.

[13] C. Foo, L. Seah, and G. Chai, "A modified energy-balance model to predict low-velocity impact response for sandwich composites", Composite Structures, vol. 93, no. 5, pp. 1385-1393, 2011.

[14] D. Horrigan and R. Aitken, "Finite element analysis of impact damaged honeycomb sandwich", FEA Ltd, Surrey, UK, 1998; [Online]. Available: http://www.lusas.cn/pdf/CS503_FEA_of_Impact_Damaged_Honeycomb_Panels.PDF

[15] D. Feng and F. Aymerich, "Damage prediction in composite sandwich panels subjected to low-velocity impact", *Composites: Part A*, vol. 52, pp. 12-22, 2013.

[16] S. Zhu and G. Chai, "Damage and failure mode maps of composite sandwich panel subjected to quasi-static indentation and low velocity impact," *Composite Structures*, vol. 101, pp. 204–214, 2013.

[17] S. Zhu and G. Chai, "Effect of adhesive in sandwich panels subjected to low-velocity impact", *Proc. IMechE Part L: J. Materials: Design and Applications*, vol. 225, pp. 171-181, 2011.

[18] M. Meo, A. Morris, R. Vignjevic, and G. Marengo, "Numerical simulations of low-velocity impact on an aircraft sandwich panel," *Composite Structures*, vol. 62, no. 3–4, pp. 353–360, 2003.

[19] M. Hazizan and W. Cantwell, "The low velocity impact response of an aluminium honeycomb sandwich structure," *Composites: Part B*, vol. 34, no. 8, pp. 679–687, 2003.

[20] P. Schubel, J. Luo, and I. Daniel, "Low velocity impact behavior of composite sandwich panels," *Composites: Part A*, vol. 36, no. 10, pp. 1389–1396, 2005.

[21] I. Lee, Y. Shi, A. Afsar, Y. Ochi, S. Bae, and J. Song, "Low velocity impact behavior of aluminum honeycomb structures", *Advanced Composite Materials*, vol. 19, pp. 19-39, 2010.

[22] I. Ivañez and S. Sanchez-Saez, "Numerical modelling of the low-velocity impact response of composite sandwich beams with honeycomb core", *Composite Structures*, vol. 106, pp. 716-723, 2013.

[23] A. Manes, A. Gilioli, C. Sbarufatti, and M. Giglio, "Experimental and numerical investigations of low velocity impact on sandwich panels", *Composite Structures*, vol. 99, pp. 8-18, 2013.

[24] M. Hoo Fatt, "Dynamic models for low-velocity impact damage of composite sandwich panels – Part A: Deformation," *Composite Structures*, vol. 52, no. 3–4, pp. 335–351, 2001.

[25] M. Hoo Fatt and K. Park, "Dynamic models for low-velocity impact damage of composite sandwich panels – Part B: Damage initiation," *Composite Structures*, vol. 52, no. 3–4, pp. 353–364, 2001.

[26] G. Clarke, Characterization of low-velocity impact damage in metallic honeycomb sandwich aircraft panels using finite element analysis. Master's thesis, The Royal Military College of Canada, 2017.

[27] D. Wowk and C. Marsden, "Effects of skin thickness and core density on the residual dent depth in aerospace sandwich panels", *Int. J. Comp. Meth. and Exp. Meas.*, vol. 4, no. 3, pp. 336-344, 2016.

[28] T. McQuigg and R. Kapania, "Compression after impact experiments on thin face sheet honeycomb core sandwich panels", Journal of Spacecraft and Rockets, vol. 51, no. 1, pp. 253-266, 2014.

[29] P. Schubel, J.-J. Luo, and I. Daniel, "Low velocity impact behavior of composite sandwich panels", *Composites: Part A*, vol. 36, pp. 1389-1396, 2005.

[30] L. Atkay, A. Johnson, and B.-H. Kröplin, "Numerical modelling of honeycomb core crush behaviour", *Engineering Fracture Mechanics*, vol. 75, pp. 2616-2630, 2008.

[31] B. Castanié, C. Bouvet, Y. Aminanda, J.-J. Barrau, P. Thevenet, "Modelling of low-energy/low-velocity impact on Nomex honeycomb sandwich structures with metallic skins", *International Journal of Impact Engineering*, vol. 35, pp. 620-634, 2008.

[32] R. Okada and M. Kortschot, "The role of the resin fillet in the delamination of honeycomb sandwich structures", Composites Science and Technology, vol. 62, pp. 1811-1819, 2002.

[33] J. Tomblin, T. Lacy, B. Smith, S. Hooper, A. Vizzini, S. Lee, "DOT/FAA/AR-99/49: Review of Damage Tolerance for Composite Sandwich Airframe Structures", Technical report, U.S. Department of Transportation, Federal Aviation Administration, Office of Aviation Research , 1999.

[34] K. Raju, B. Smith, J. Tomblin, "Impact Damage Resistance and Tolerance of Honeycomb Core Sandwich Panels", *Journal of Composite Materials*, vol. 42, no. 4, pp.385-412, 2008.

[35] T. Besant, G. Davies, and D. Hitchings, "Finite element modelling of low velocity impact of composite sandwich panels", *Composites: Part A*, vol. 32, pp. 1189-1196, 2001.

[36] D. McGowan and D. Ambur, "Damage characteristics and residual strength of composite sandwich panels impacted with and without compression loading", Technical report, NASA Langley Research Center, 1998.

[37] Y. Aminanda, B. Castanié, J.-J. Barrau, and P. Thevenet, "Experimental and numerical study of compression after impact of sandwich structures with metallic skins", *Composites Science and Technology*, vol. 69, pp. 50-59, 2009.

[38] T. McQuigg and R. Kapania, "Compression after impact analysis on thin face sheet honeycomb core sandwich panels", *Journal of Spacecraft and Rockets*, vol. 51, no. 1, pp. 200-212, 2014.

[39] A. Gilioli, C. Sbarufatti, A. Manes, and M. Giglio, "Compression after impact test (CAI) on NOMEX™ honeycomb sandwich panels with thin aluminum skins", *Composites: Part B*, vol. 67, pp. 313-325, 2014.

[40] C. Fischer, F. Hähnel, A. Hauffe, and K. Wolf, "Strategies to investigate the residual strength of impact damaged honeycomb sandwich structures

using detailed numerical models", Conference paper, 21st International Conference on Composite Materials, 2017.

[41] A. Akatay, M. Bora, O. Çoban, S. Fidan, and V. Tuna, "The influence of low velocity repeated impacts on residual compressive properties of honeycomb sandwich structures", Composite Structures, vol. 125, pp. 425-433, 2015.

[42] Y. Feng, Y. He, H. Zhang, X. Tan, T. An, and J. Zheng, "Effect of fatigue loading on impact damage and buckling/post-buckling behaviors of stiffened composite panels under axial compression", *Composite Structures*, vol. 164, pp. 248-262, 2017.

[43] K.-W. Kang, H. Kim, M. Kim, and J.-K. Kim, "Strength reduction behavior of honeycomb sandwich structure subjected to low-velocity impact", *Materials Science and Engineering A*, vol. 483-484, pp. 333-335, 2008.

[44] B. Freeman, E. Schwingler, M. Mahinfalah, and K. Kellogg, "The effect of low-velocity impact on the fatigue life of Sandwich composites", *Composite Structures*, vol. 70, pp. 374-381, 2005.

[45] M. Klaus, H.-G. Reimerdes, and N. Gupta, "Experimental and numerical investigations of residual strength after impact of sandwich panels", *International Journal of Impact Engineering*, vol. 44, pp. 50-58, 2012.

[46] J. Tomblin, L. Ilcewicz, A. Vizzini, T. Lacy, and Y. Hwang, "DOT/FAA/AR-02/121: Guidelines for Analysis, Testing, and Nondestructive Inspection of Impact-Damaged Composite Sandwich Structures", Technical report, U.S. Department of Transportation, Federal Aviation Administration, Office of Aviation Research, 2003.

[47] MatWeb: Online Materials Information Resource; [Online]. Available: http://www.matweb.com.

[48] E. Avallone, T. Baumeister III, and A. Sadegh, Mark's Standard Book for Mechanical Engineers, McGraw-Hill, 11th edition, 2007.